THESIS FOR THE DEGREE OF DOCTOR OF PHILOSOPHY

Fractal superconducting resonators for the interrogation of two-level systems

SEBASTIAN DE GRAAF

Department of Microtechnology and Nanoscience
CHALMERS UNIVERSITY OF TECHNOLOGY
Göteborg, Sweden 2014

Chalmers University of Technology
Department of microtechnology and nanoscience, MC2
Quantum device physics laboratory
Experimental Mesoscopic Physics Group
SE-41296, Göteborg, Sweden
Telephone: +46 31 72 1000

Fractal superconducting resonators for the interrogation of two-level systems
Sebastian de Graaf
Department of Microtechnology and Nanoscience, MC2
Chalmers University of Technology, 2014

Abstract

In this thesis we use high-Q superconducting thin-film microwave resonators to interact with several types of quantum mechanical two-level systems. Such a resonator is used as the central building block in a cryogenic near-field scanning microwave microscope (NSMM) to reach a completely new regime of NSMM operation. In this regime where the superconducting resonator is only populated with a small number of photons, we demonstrate a capacitance sensitivity down to $64 \cdot 10^{-21}$ Farad$/\sqrt{\text{Hz}}$ and nanoscale resolution, which is sufficient to apply this scanning probe technique to quantum coherent objects. Such a 'coherent'-NSMM enables several new applications: for example to study the interaction of the NSMM probe with two-level defects in samples and to characterize artificial two-level systems (qubits), which eventually could lead to better understanding of decoherence mechanisms in superconducting quantum circuits.

We demonstrate the ability to reach this regime in a sample consisting of a Cooper-pair box (CPB) weakly coupled to a superconducting resonator. In the strong driving regime we observe Landau-Zener-Stückelberg interference and we discover a new type of relaxation mechanism in the strongly driven CPB that involves pair breaking and quasiparticle tunneling. It results in a recovered parity of the CPB and a population inversion of the dressed states. Not only does this demonstrate the applicability of NSMM for qubit characterization, but the quasiparticle mediated population inversion also becomes suitable for robust charge sensing in a scanning probe setup.

To integrate the superconducting resonator onto our NSMM probe we develop a new type of resonator design - the fractal design - that have a very small external dipole moment allowing for a compact resonator. Another advantage of the fractal resonator is its resilience to magnetic fields. We show that the fractal resonator, after further optimization, can maintain quality factors above 10^5 in applied fields of more than 400 mT, something that becomes particularly useful for the interrogation of spin ensembles coupled to the resonator. We demonstrate that it is possible to detect down to $5 \cdot 10^5$ spins$/\sqrt{\text{Hz}}$ in a very small volume coupled to a fractal resonator. Furthermore, the low dipole moment of the fractal resonator allows us to also introduce DC bias into the resonator without degrading its Q-factor. This is an important technological step that allows us to interact with new materials where spins can be quickly and locally manipulated using electric fields and we demonstrate the first steps in this direction with ensembles of manganese doped ZnO nanowires and frustrated molecular Cu spin triangles.

The measurements achieve a very high sensitivity thanks to the Pound-Drever-Hall locking technique used. We develop this technique such that both resonance frequency and quality factor can be monitored with very high accuracy in real time. The demonstrated stability is $\sim$30 Hz$/\sqrt{\text{Hz}}$ for frequency readout and we can determine the Q-factor with a precision of 34 dB$/\sqrt{\text{Hz}}$.

Keywords: Superconducting resonators, near-field scanning microwave microscopy, atomic force microscopy, decoherence, electron spin resonance, circuit quantum electrodynamics, two-level systems, Cooper-pair box, quasiparticles.

LIST OF PUBLICATIONS

This thesis is based on the following publications:

I. *Magnetic field resilient superconducting fractal resonators for coupling to free spins*,
S. E. de Graaf, A. V. Danilov, A. Adamyan, T. Bauch, and S. E. Kubatkin,
J. Appl. Phys, **102**, 123905 (2012).

II. *A scanning near field microwave microscope based on a superconducting resonator for low power measurements*, S. E. de Graaf, A. V. Danilov, A. Adamyan, and S. E. Kubatkin,
Rev. Sci. Instrum. **84**, 023706 (2013).

III. *Charge Qubit Coupled to an Intense Microwave Electromagnetic Field in a Superconducting Nb Device: Evidence for Photon-Assisted Quasiparticle Tunneling*, S. E. de Graaf, J. Leppäkangas, A. Adamyan, M. Fogelström, A. V. Danilov, T. Lindström, S. E. Kubatkin, and G. Johansson,
Phys. Rev. Lett., **111**, 137002 (2013).

IV. *Effect of quasiparticle tunneling in a circuit-QED realization of a strongly driven two-level system*, J. Leppäkangas, S. E. de Graaf, A. Adamyan, A. V. Danilov, T. Lindström, M. Fogelström, G. Johansson, and S. E. Kubatkin,
J. Phys. B: At. Mol. Opt. Phys., **46**, 224019 (2013).

V. *Galvanically split superconducting microwave resonators for introducing internal DC bias*, S. E. de Graaf, D. Davidovikj, A. Adamyan, A. V. Danilov, and S. E. Kubatkin,
Submitted to Appl. Phys. Lett. (2013).

VI. *Accurate real-time monitoring of quality factor and center frequency of superconducting resonators*, S. E. de Graaf, A. V. Danilov, and S. E. Kubatkin,
Submitted to IEEE Trans Appl Supercond. (2013).

Other publications not included in this thesis:

VII. *Identifying noise processes in superconducting resonators*, J. Burnett, T. Lindstrom, I. Wisby, S. E. de Graaf, A. Adamyan, A. V. Danilov, S. Kubatkin, P. J. Meeson and A.Ya.Tzalenchuk,
Proceedings of the 14th International Superconducting Electronics Conference (ISEC), p. 1-3 (2013).

Paper I This paper describes the design of the fractal resonator and its performance in magnetic fields. My contribution consisted of fabricating most of the samples, developing the measurement setup (hardware + software), performing the measurements, analyzing the data and writing the paper with support from AD who also performed most of the simulations. AA assisted with sample fabrication and preparation, TB assisted with measurements in the dilution fridge and some theoretical support.

Paper II Describes the principles and performance of our low power near-field microwave microscope. I designed and developed the microscope hardware with support from AD. I designed and fabricated all scanning probes and samples with some support from AA. I set up the measurement hardware and software (AFM + PDH-loop), performed all the measurements, analyzed the data and wrote the paper.

Paper III and IV describes the measurement of a Cooper-pair box in a strong electromagnetic field and we observe a new regime where quasiparticles play an interesting role in the dynamics of the system. I set up and developed the hardware with support from TL and TB. I helped develope the fabrication process with AA who eventually made the sample, I performed the measurements with help form TL and AD, analyzed the data together with JL who developed the theory with support form GJ and MF. I wrote paper III with support from JL and the other way around for paper IV.

Paper V describes a superconducting resonator design optimized for electrostatic interaction with spin ensembles. I wrote the paper after analyzing the data and devicing the measurement setup. DD and AD designed the samples and DD and AA did the fabrication and the measurements with the assistance of me and AD.

Paper VI describes the measurement setup we use in several of the other experiments. We demonstrate the applicability of the method for tracking superconducting resonators in magnetic field sweeps, where the resonance frequency changes substantially more than the resonance linewidth. We obtain a frequency stability unaffected by the measurement of quality factor: $\sim 10 - 30 \text{ Hz}/\sqrt{\text{Hz}}$ and the Q can be measured with accuracy $34 \text{ dB}/\sqrt{\text{Hz}}$. I wrote the paper after performing the measurements and deriving the theory. Data analysis and constructing the measurement setup was done with the assistance of AD.

Contents

List of Abbreviations

AFM	–	Atomic Force Microscopy
nc-AFM	–	non-contact Atomic Force Microscopy
AM	–	Amplitude Modulation
CPB	–	Cooper-Pair Box
CPW	–	Coplanar Wavegiude
CPWR	–	Coplanar Waveguide Resonator
DPPH	–	2,2-diphenyl-1-picrylhydrazyl
DUT	–	Device Under Test
EFM	–	Electrostatic Force Microscopy
ESR	–	Electron Spin Resonance
FIB	–	Focused Ion Beam
FM	–	Frequency Modulation
KPFM	–	Kelvin Probe Force Microscopy
LZ	–	Landau-Zener (tunneling)
LZS	–	Landau-Zener-Stückelberg (interferometry)
NBI	–	Norris-Brandt-Indenbom (model)
NSMM	–	Near-field Scanning Microwave Microscopy
NV	–	Nitrogen-Vacancy (centers)
PDH	–	Pound-Drever-Hall
PID	–	Proportional-Integrating-Differential (controller)
PLL	–	Phase Locked Loop
PM	–	Phase Modulation
PSD	–	Power Spectral Density
QED	–	Quantum Electrodynamics
QIP	–	Quantum Information Processing
RF	–	Radio Frequency
SEB	–	Single Electron Box
SMM	–	Single Molecule Magnet
SNOM	–	Scanning Near-field Optical Microscopy
SNR	–	Signal-to-Noise Ratio
SPM	–	Scanning Probe Microscopy
SQUID	–	Superconducting Quantum Interference Device
STM	–	Scanning Tunneling Microscopy
TLF	–	Two-Level Fluctuator
TLS	–	Two-Level System
VCO	–	Voltage Controlled Oscillator
VNA	–	Vector Network Analyzer
YIG	–	Yttrium-Iron Garnet (filter)
ZFS	–	Zero-Field Splitting

List of symbols & constants

Fundamental constants

e – Electron charge
k_B – Boltzmann constant
h – Planck constant
$\hbar$ – $h/2\pi$
μ_0 – Vacuum permeability
μ_B – Bohr Magneton
c – Speed of light
ϵ_0 – Vacuum permittivity
ϵ_r – Dielectric constant
Φ_0 – Flux quantum
m_e – Electron mass

Superconductor and resonator properties

W – Strip width
S – Gap width
d – Thin-film thickness
λ_L – London penetration depth
λ_{eff} – Thin-film penetration depth
λ – Wavelength
ξ – Coherence length
d – Thin-film thickness
γ – Propagation constant
α – Attenuation constant
β – Phase constant
T – Temperature
T_c – Critical temperature
L_g – Geometric inductance
L_k – Kinetic inductance
τ_n – Quasiparticle scattering time
Δ – Superconducting energy gap
ω – Angular frequency
ω_0 – Angular Resonance frequency
t – Time
N – Number of photons
S_{21} – Transmission coefficcient
R – Resistance
G – Conductance
C – Capacitance
C_0, C_r – Resonator capacitance
C_c – Coupling capacitance
L – Inductance
L_0, L_r – Resonator Inductance
M – Mutual inductance
Q – Total quality factor
Q_i – Internal quality factor
Q_c – Coupling quality factor
Q_B – Magnetic field induced quality factor
Q_{rad} – Radiation loss quality factor
p_0 – Power dissipation per unit length
$\tan\delta$ – Loss tangent

σ – Conductivity
Z – Impedance
Z_0 – Characteristic impedance 50Ω
Z_r – Resonator impedance
V – Voltage
I – Current
E – Energy
j – Current density
H – Magnetic field
H_c – Thermodynamic critical field
$H_{c1/2}$ – Lower / upper critical field
$K(x)$ – Elliptic integral (first kind)

PDH measurement technique

α, β – Modulation depth
$\Omega, \Omega_1, \Omega_2$ – Angular modulation frequency
$J_n(x)$ – n:th order Bessel function
P_0 – Total spectrum power

NSMM

E – Electric field
Γ – Reflection coeficcient
Z_s – Sample impedance
Z_t – Tip (resonator) impedance
C_{t-s} – Tip-Sample capacitance
x_s – Normalized sample reactance
r_s – Normalized sample resistance
Q_s – Sample-induced quality factor
k – Spring constant

Cooper-pair box

$a, (a^\dagger)$ – Photon creation (annihilation) op.
A_{ng} – Microwave induced gate charge
β – Dimensionless drive strength
C_J – Junction capacitance
C_g – Gate capacitance
C_Σ – Total capacitance
Δ_m – Dressed energy gap
Δ – Superconductor energy gap
E_C – Charging energy
E_J – Josephson energy
δE_C – Charging energy difference
$f(\omega)$ – Fermi distribution
g – Coupling
n_g – Gate charge
n – Electron number
θ – Mixing-angle

Cooper-pair box (cont.)

ν, ν_0	–	Slew rate
n_{g0}	–	Average (static) gate charge
N	–	Number of photons
R_Q	–	Resistance quantum
$\rho(\omega)$	–	BCS density of states
$\sigma_x, \sigma_y, \sigma_z$	–	Pauli matrices
σ^+, σ^-	–	TLS raising and lowering operator
T_1	–	Relaxation time
T_2	–	Dephasing time

Spin ensembles

C	–	Chirality
C^+, C^-	–	Chirality raising and lowering op.
g	–	gyromagnetic ratio, g-factor
Γ	–	Total coupling
Γ_0	–	Single spin coupling
γ	–	Spin linewidth
D	–	Zero-field splitting
E_0	–	Single photon induced electric field
I_0	–	Single photon induced current
κ	–	Dipole coupling
M	–	Magnetization
N	–	Number of spins
S	–	Spin angular momentum

1

INTRODUCTION

A large part of our understanding of materials and their properties comes from their interaction with electromagnetic waves. For example, we can probe the quantum mechanical nature of atoms and molecules by irradiating them with photons and study the absorption to find the electronic structure. A similar setup can be used to perform computation. In a classical computer information processing occurs through semiconducting materials whos' highly nonlinear density of states is used to control the flow of charge carriers, bearers of classical information. Similarly, for quantum computation we rely on the most fundamental of electronic structures – a two-level system (TLS) in which a single bit of quantum information can be encoded.

As envisioned by Feynman in 1982 [1], quantum systems could potentially be used to compute their own time-evolution, thus solving problems in a timescale much shorter than classical computers. Since then the field of quantum based computation has evolved with a tremendous pace and today several different technologies such as quantum optics [2], semiconductor quantum-dots [3] and superconducting integrated circuits [4] have become mature enough to soon make a leap towards large scale integration of quantum circuits. However, to achieve fault tolerant large scale quantum computation very high requirements on reproducibility and stability are required [4, 5].

In practical situations the quantum state will not persist for an infinite amount of time. It will be subject to decoherence and dephasing due to leakage of energy into degrees of freedom other than those used for information processing. Such a lossy environment can also be described in terms of a large number of two-level systems that couple to the qubit and photon modes. The study of the physics behind these loss mechanisms is currently a very important topic, and constitutes one of the main technological limitations of todays quantum circuits. While clever design can elude some of the most detrimental loss mechanisms [4, 6–8] there still remains a large number of problems to be solved within materials science before quantum computing can become a mature technology [6].

This brings us back to the importance of studying both the qubits and their environment using electromagnetic waves in order to pinpoint and eliminate the material defects and impurities that lead to excess losses in these devices. The physical origin of some of the mechanisms behind this excess loss is still a widely debated topic [6, 9], and in order to gain a better understanding many different tools for characterization will be required. Having this in mind, the long-term goal of the main project described in this thesis is to develop several of these tools.

To study (artificial)atom-photon interactions on the nanoscale we take the well known technique of Near-field Scanning Microwave Microscopy (NSMM) and bring it to a new regime. NSMM is a scanning probe technique [10] that studies the interaction of microwaves with a sample in the near-field regime, overcoming the Abbe resolution limit $d > \lambda/2n_i \sin\theta$

of propagating electromagnetic radiation. By combining this technique with an Atomic Force Microscope (AFM) [11] we can obtain spatial information down to the nanoscale. The new regime of NSMM that we reach involves a very small probing power, so small that we can start to interrogate quantum two-level systems. We show that the obtained sensitivity is sufficient to perform qubit characterization, in the so called strong driving regime, using a scanning probe setup. This can become particularly useful for the characterization of future large-scale quantum circuits involving many qubits [4, 5].

Such characterization can reveal many properties of the qubit itself and its environment. In particular, we discover a new regime in one of our samples that reveals a new type of dissipation channel in the qubit. Not only does this demonstrate the usefulness of qubit characterization using NSMM, but it also results in another interesting application: in this new regime, the qubit itself shows a very high charge sensitivity with several advantages over other scanning-probe charge-sensing instruments, such as the scanning single electron transistor microscope [12]. In terms of NSMM this means that instead of characterizing qubits with microwaves we can also integrate the qubit onto our NSMM probe and perform robust charge sensing on the nanoscale [12–14]. This provides for a complementary way of interrogating quantum devices on the nanoscale.

As the fundamental building block for our low power NSMM we use a micromachined superconducting thin-film microresonator that is designed to be compact and light enough to fit onto our AFM cantilever, without disrupting its mechanical properties. Superconducting resonators have shown to be very versatile tools, not only as central building blocks in superconducting quantum circuits, but also as astronomy detectors [15, 16] and parametric amplifiers [17]. They turn out to be very sensitive probes of their environment, and together with their very wide operating range they can be used both as part of devices and circuits, and as tools to characterize these devices and circuits throughoutly.

The second track of the thesis will be dealing with a slightly different topic, but again the central physics is the interaction of microwaves with large ensembles of two-level systems. This time we instead consider the interaction between spin degrees of freedom and microwave photons, and it illustrates the wide applicability of superconducting resonators. Coupling spin degrees of freedom to microwave cavities is a direction which is currently under much investigation within the field of solid state quantum information processing. Spin ensembles have shown to exhibit very long coherence times [18], which makes them suitable for storage of quantum information in hybrid quantum circuits. Futhermore, recent advances in supra-molecular chemistry shows that a new class of materials called Single Molecule Magnets (SMM) could potentially also be used to perform quantum computation [19], and the properties of such a qubit and/or memory could be chemically engineered to fit a wide range of applications.

The first spin ensembles coupled to resonators that were demonstrated have several shortcomings when it comes to scalability and diversity: The ensembles are very large and the interaction is controlled by magnetic fields. Such control is not only slow but could also not be made local. On the other hand, electric fields can easily be localized and tuned much faster. This does, however, still require that the spin ensemble is brought to the right working point in magnetic field, which unfortunately can be very large and detrimental for superconducting resonators.

Our resonators are particularly useful for operation in strong magnetic fields, where we have demonstrated performance an order of magnitude better than previously reported. This makes the resonators particularly useful for interaction with spin ensembles and electron spin resonance (ESR) measurements. We specifically aim towards interacting with a

new class of exotic spin systems that by chemical design couple spin degrees of freedom to electric fields. The ability to manipulate spins with electric fields is one important direction that could enable large scale integration of quantum memories on-chip. For this purpose we have specifically developed a resonator in which we can introduce static electric fields without introducing additional loss in the resonator.

This thesis is organised as follows. The first chapter outlines the fundamentals of superconducting resonators and then continues with describing our developed 'fractal' resonators, with focus on magnetic field performance. In Chapter 3 a measurement technique that have been extensively used throughout this thesis will be described. This technique is adapted from frequency metrology and is called Pound-Drever-Hall locking. In this thesis we extend this method such that we can measure both the center frequency and quality factor of our microwave resonators with unmatched precision and bandwidth. In Chapter 4 the details of the developed near-field scanning microwave microscope will be outlined and in the next chapter (Chapter 5) we both theoretically and experimentally investigate the new regime of NSMM that we have reached with our microscope. This is done in a test sample consisting of a qubit coupled to a microwave resonator mimicking the conditions of NSMM. We find that the NSMM can be used for qubit characterization and we also discover an interesting new relaxation mechanism in the qubit. This mechanism is described in chapter Chapter 6 and we discuss its applications to materials characterization using NSMM and charge sensing scanning probe tools.

Finally, in Chapter 7 we discuss the second major application of the 'fractal' resonators, namely that of hybrid quantum systems and electron spin resonance (ESR), another class of two-level systems, using chemically tailored spin ensembles to enable new technologies for quantum information storage. Manipulation of spin ensembles using electric fields again bring us back to the NSMM which can be directly applied to further characterize such systems.

2
FRACTAL RESONATORS

In this chapter we start by defining a few concepts that apply to superconducting resonators in general. We then continue by outlining different aspects that are limiting the performance of coplanar resonators in the specific regimes that we are interested in. Based on these different shortcomings we then create the "fractal" resonators which solves several of the issues introduced here (but also adds a few more issues).

To put the developments outlined here in a wider context it should be noted that there is currently a large interest in going beyond the coplanar waveguide (CPW) design for quantum information processing (QIP) purposes. For example, different geometries could be used to protect qubits from decaying energy into unwanted modes [20–22], or to eliminate dielectric losses by using cavities that store most of their energy in vacuum [8, 23] which can reach quality factors above 10^8, to name a few examples of this rapidly developing field.

2.1   Fundamentals of superconducting resonators

In this section we look at the most fundamental aspects of superconducting resonators in general and in particular the quarter-wave resonator measured in transmission. We start by defining a coplanar transmission line and its geometry, shown in Fig. 2.1. A superconducting thin-film of thickness d is located on top of a dielectric substrate with dielectric constant $\varepsilon = \varepsilon' + i\varepsilon''$. The thin-film is patterned into the CPW geometry, having a central conducting strip of width W. The central strip is separated from two (semi-infinite) ground planes by a gap of width G. We also define $a = 2G + W$. A CPW can be described by its characteristic impedance

$$Z_0 = \sqrt{\frac{R + i\omega L}{G + i\omega C}}, \tag{2.1}$$

where L and C is the inductance and capacitance per unit length, and R and G is the resistance and conductance per unit length. In the lossless case $Z_0 = \sqrt{L/C}$, which is a good approximation for a superconductor. We define the microwave signal propagating in the transmission line as plane wave in the y-direction: $Ae^{\gamma y + i\omega t}$, were

$$\gamma = \sqrt{(R + i\omega L)(G + i\omega C)} = \alpha + i\beta, \tag{2.2}$$

is the propagation constant [24]. $\beta = \omega/\nu_{ph}$ is the phase constant of the line and α is the attenuation constant.

From such a transmission line we can now define a resonant structure by taking a piece of transmission line of length l. The line impedance is then

$$Z_l = Z_0 \tanh(\gamma l). \tag{2.3}$$
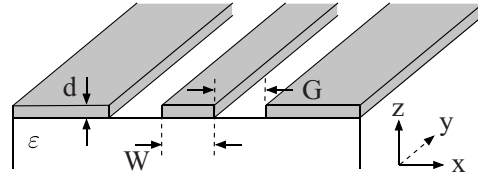
Figure 2.1: Geometry of a coplanar transmission line.

Using the transmission constant from eq. (2.2) we can rewrite this expression as

$$Z_l = Z_0 \frac{1 - i \tanh \frac{\beta l}{2Q_i} \cot \beta l}{\tanh \frac{\beta l}{2Q_i} - i \cot \beta l}, \tag{2.4}$$

where the internal quality factor is defined as $Q_i = \beta/2\alpha$. We now select $l = \lambda/4 = \pi v_{ph}/2\omega_0$ to be the length of the resonator. This allows us to write $\beta l = \frac{\pi}{2}(1 + \Delta\omega/\omega_0)$ and near the resonance frequency we may Taylor expand eq. (2.4) and to first order we get [24, 25]

$$Z_l = Z_0 \frac{4Q_i/\pi}{1 + 2iQ_i \frac{\Delta\omega}{\omega_0}}, \tag{2.5}$$

where $\Delta\omega = \omega - \omega_0$ is the detuning from the resonance frequency.

Capacitive coupling

In order to excite the resonator it has to be coupled to some source of microwave radiation. The most straightforward way of doing this is by using a capacitive coupling. For a microwave transmission line we can treat the coupled resonator as a parallel shunted stub with impedance

$$Z_t = 1/j\omega C_c + Z_l. \tag{2.6}$$

At the resonance frequency the imaginary part of the impedance goes to zero. This we can use to find the loaded resonance frequency

$$\frac{\omega - \omega_0}{\omega_0} \approx -\frac{2Z_0\omega_0 C_c}{\pi}. \tag{2.7}$$

Assuming a matched network, i.e. both feedline and resonator is 50 Ω, the power that is dissipated through the coupling element is

$$P_{\text{leak}} = I^2 Z_0 = (\omega C_c V)^2 Z_0. \tag{2.8}$$

Since the quality factor is defined as the amount of energy stored ($E = C_r V^2/2$) divided by the power dissipated per cycle we can now define a quality factor associated with the coupling capacitance

$$Q_c = \frac{E\omega}{P_{\text{leak}}} = \frac{C_r}{2\omega C_c^2 Z_0} = \frac{\pi}{2\omega^2 C_c^2 Z_0 Z_r}. \tag{2.9}$$

Using this it is possible to express the loaded resonance frequency through the coupling quality factor. Eq. (2.7) becomes

$$\frac{\omega - \omega_0}{\omega_0} \approx -\sqrt{\frac{2}{\pi Q_c}}. \tag{2.10}$$
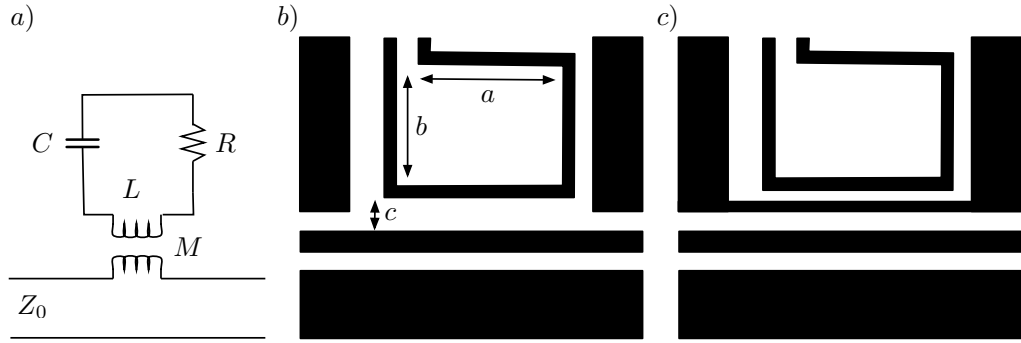
Figure 2.2: a) Lumped element circuit model used in the derivation of the inductively coupled resonator. b) and c) two different coupling geometries discussed in the text.

By using this new resonance frequency we can write eq. (2.6) on the following form

$$\frac{Z_{in}}{Z_0} = \frac{2Q_c}{Q_i}\left(1 + 2iQ_i\frac{\Delta\omega}{\omega_0}\right). \tag{2.11}$$

For a parallel shunt impedance the transmission signal is given by [24]

$$S_{21} = \frac{2}{2 + Z_0/Z_{in}} = \frac{\left(1 + 2iQ_i\frac{\Delta\omega}{\omega_0}\right)}{\left(1 + 2iQ_i\frac{\Delta\omega}{\omega_0}\right) + \frac{Q_i}{Q_c}} = \frac{S_{21,min} + 2iQ\frac{\Delta\omega}{\omega_0}}{1 + 2iQ\frac{\Delta\omega}{\omega_0}}, \tag{2.12}$$

with

$$S_{21,min} = \frac{Q_c}{Q_i + Q_c} \qquad Q = \frac{Q_iQ_c}{Q_i + Q_c}. \tag{2.13}$$

The above equations can also be combined to give the more common expression for the total quality factor as the reciprocal sum of individual quality factors

$$\frac{1}{Q} = \frac{1}{Q_c} + \frac{1}{Q_i}. \tag{2.14}$$

Inductive coupling

For most of the resonators considered in this thesis we use inductive coupling instead of capacitive coupling. The main reason for this is within the NSMM application, here we desire a compact and mechanically decoupled excitation of the resonator that we use as a near-field probe and the inductive scheme provides an excellent solution for this problem.

The circuit considered in this case is shown in Fig. 2.2a, where the resonator itself is represented as a series RLC-circuit with impedance Z_r. The input impedance of the circuit in Fig. 2.2a is [26, 27]

$$Z_{in} = j\omega L_1 + \frac{\omega^2 M^2}{Z_r}, \tag{2.15}$$

where M is the mutual inductance and L_1 the inductance of the transmission line over the coupling segment. From this expression it is possible to derive exactly the same expression, eq. (2.12), for the resonance lineshape as in the case of capacitive coupling (see Appendix

C for a derivation). This means we can treat this kind of resonators using exactly the same framework that has been developed for capactively coupled resonators. The coupling quality factor becomes

$$Q_c = \frac{2Z_0 Z_r}{\omega_0^2 M^2}.$$

(2.16)

The mutual inductance is strongly dependent on geometry of the coupling element, and in most cases it can only be evaluated numerically. For the simple case shown in Fig. 2.2b it is possible to estimate the mutual inductance between an infinite wire and a single rectangular loop by using Biot-Savart's law.

$$Q_c = \frac{8\pi^2 Z_0 Z_r}{\omega_0^2 \mu_0^2 a^2 \ln^2 \left[1 + \frac{b}{c}\right]}.$$

(2.17)

For many practical applications requiring high qaulity factors this simple geometry is not sufficcient. Much better control of the coupling is obtained if another grounded segment is introduced inbetween the resonator and feedline (as illustrated in fig. 2.2c). The main effect from this is that this conductor effectively screens the resonator. The current induced in this strip will be of similar magnitude as the current in the feedline, but with the opposite sign. The effective coupling that the resonator experiences is therefore reduced considerably. This gives much better control in designing the coupling Q on the level of a few tenths of thousands and above. However, it becomes difficult to obtain an analytical expression for the mutual inductance, and either experimental iterations or numerical simulations have to be used.

Photon number

The number of photons in the resonator can be estimated by considering how much power is pumped into the resonator. If a quarter wave cavity is probed with power P_{in} the equivalent average energy in the resonator when excited at resonance is given by [25]

$$\langle E_{int} \rangle = \frac{2}{\pi} \frac{Z_0}{Z_r} \frac{Q^2}{Q_c} \frac{P_{in}}{\omega_0},$$

(2.18)

and the average number of photons in the resonator is

$$\langle N \rangle = \frac{\langle E_{int} \rangle}{\hbar \omega_0}.$$

(2.19)

As an example, for a 5 GHz critically coupled resonator with $Q_i \sim 10000$ we need to probe the cavity with a power around 1.25 aW ($\sim$ -140 dBm) to have on average a single quanta of energy inside the resonator.

Properties of resonance curves

The general characteristics of the transmitted signal S_{21} is visualized in Fig. 2.3. We can plot both the magnitude and the phase of eq. (2.12). At resonance the imaginary part goes to zero, i.e. the phase is 0 and the magnitude is given by $S_{21,min}$. Care should be taken when comparing different resonator configurations. Even if the transmitted amplitude $|S_{21}|$ may look the same for a quarter wave resonator measured in transmission or a half-wave resonator measured in reflection, the phase response and the physical picture can be very different.
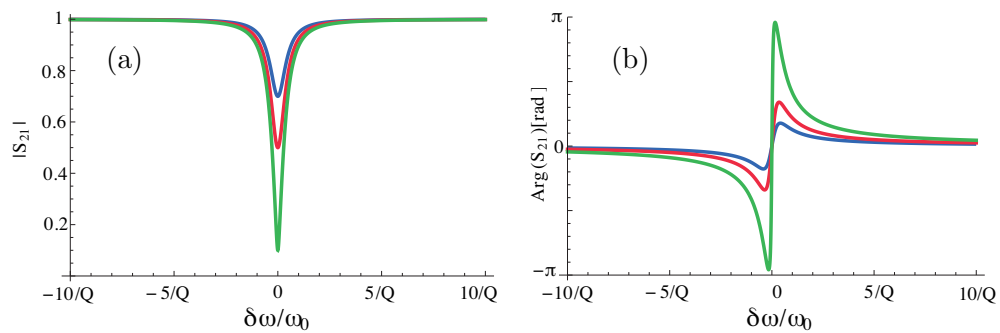
Figure 2.3: Magnitude (a) and phase (b) of the transmission S_{21} (eq. (2.12)) for three possible cases of coupling. Blue curve is for the undercoupled case when $Q_i > Q_c$, red is critical coupling $Q_i = Q_c$ and green the overcoupled case $Q_i < Q_c$.

It is important to note that the above equation for S_{21} is only valid for a quarter-wave resonator measured in transmission, for other geometries see for example [16, 24, 25, 28].

The three resonance curves plotted in Fig. 2.3 constitute three different coupling regimes. These are called undercoupled ($Q_i > Q_c$), critically coupled ($Q_i = Q_c$) for which we achieve full matching of the resonator to the coupled transmission line, and finally the overcoupled regime ($Q_i < Q_c$).

For an ideal resonator measured in transmission the magnitude of S_{21} will never reach zero at the resonance frequency, resulting in a phase response that is always less than 2π. This is a drawback for phase-sensitive detector applications, since a resonator measured in reflection can have a much steeper phase response. This constitutes a complete wrap-around of the resonance curve around (0,0) in the complex plane (Fig. 2.4b). However, for application to NSMM and applications requiring multiplexing of resonators [29] reflection measurements become less convenient.

Assymmetry in the resonance lineshape

The above situation represents the ideal case, but in reality we often encounter an asymetric lineshape. This manifests itself as a rotation of the resonance circle (i.e. the real and imaginary parts of S_{21} plotted in the complex plane, see Fig. 2.4b). We can model this by adding a complex factor to eq. (2.12).

$$S_{21} = \frac{S_{21,\mathrm{min}}e^{i\varphi} + 2iQ\frac{\Delta\omega}{\omega_0}}{1 + 2iQ\frac{\Delta\omega}{\omega_0}}. \tag{2.20}$$

As pointed out in Ref. [30] this parameter should be considered as an independent complex coupling, and simply rotating the center of the resonance circle in the complex plane back to the real axis (in which case the asymetry is regarded as a property not intrinsic to the resonator) does not account for the scaling of the radius ($\propto 1/\cos\varphi$) of the resonance circle that this parameter causes. Thus simply rotating back the circle to put the resonance at the real axis will give an error in the extracted quality factors, this becomes mostly prominent if the resonator is in the undercoupled regime, as can be seen in Fig. 2.4 where the same asymmetry factor results in a large rotation for a weakly coupled resonator as compared to a strongly coupled one. Proper fitting should include φ in the form of eq. (2.20) as an additional fitting parameter.
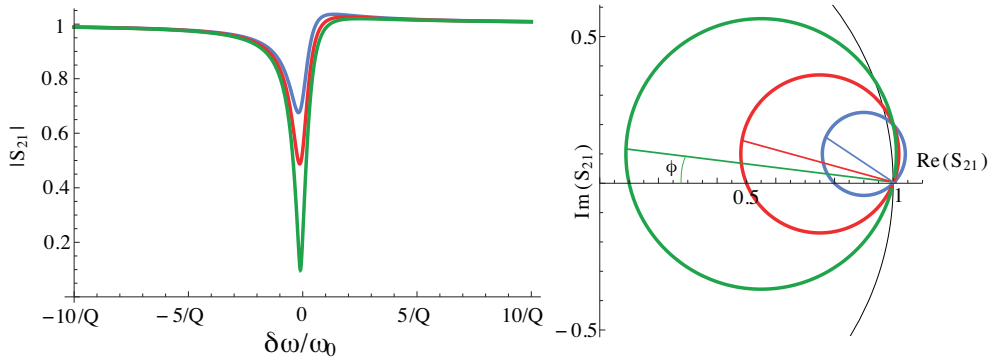
Figure 2.4: The result of an asymmertic coupling parameter $\varphi = 0.2$ for the same resonance conditions as in Fig. 2.3. The effects are best seen in the complex plane. The resonance circle is rotated around the point $[1, 0]$ in the complex plane with an angle that is increasing as internal Q is lowered. Black line is a guide for the eye at $|S_{21}| = 1$.

The physical reason for the asymmetry could be due to several factors. An impedance mismatch can easily result in asymmetry [30, 31]. Another reason may be due to spurious wide resonances in round planes and other structures that couples to the resonant mode. Using inductive coupling can often result in asymmetry, especially if the coupling element is large since it then also can obtain a significant capacitive coupling contribution. Furthermore, placing several resonators close to each other on the same feedline results in the resonators at the ends of the array usually having a more asymetric lineshape, a result of increased impedance mismatch, each coupled resonator essentially working as an impedance transformer for the next.

2.2 Loss mechanisms in superconducting resonators

So far we have only treated the resonators using a single parameter describing its internal losses, the internal quality factor Q_i. There are, however, several different mechanisms that can contribute to the loss of energy in the resonator. In this section we will outline the most relevant of these mechanisms. For example, in a scanning probe setup, many technical solutions presented in literature [32, 33] have quality factors that are (at least partially) limited by radiation losses due to geometrical constraints. As another example, the superconducting CPW resonator geometry allows to greatly suppress radiation losses to such an extent that the dominant contribution instead now comes from dielectric loss. For both NSMM and ESR applications some of the otherwise small loss mechanisms become dominant. These, and other, mechanisms are outlined in this and the following section.

In general we may add upp all the different contributions reciprocally, such that the total internal loss rate becomes

$$\frac{1}{Q_i} = \frac{1}{Q_{rad}} + \frac{1}{Q_\sigma} + \frac{1}{Q_\epsilon} + \frac{1}{Q_B} + \text{etc.} \tag{2.21}$$

These different quality factors that contribute to losses will be discussed in the following sections.

2.2.1 Radiation losses

The first loss mechanism we will consider is one that is, for CPW resonators, usually very small and can be neglected. Physically, this loss is associated with energy simply radiating into free space, rather than being confined in the resonant structure. For the simple geometry of CPW resonators it can be evaluated analytically and was found to be [16] $Q_{\rm rad} \approx 3.4(l/(2S + W))^2$, where l is the length of the resonator and S the gap between ground planes and center conductor of width W, as in Fig. 2.1. The prefactor is derived from the specific CPW geometry. This results in radiation losses on the order of $Q_{\rm rad} = 10^6 - 10^7$ for typical CPW dimensions.

These high Q-values can be explained by the very low dipole moment of the CPW structure: any current flowing in the center-conductor will be screened by a current flowing in the opposite direction in the ground planes. However, increasing the distance to the ground planes (large S) will result in increased dissipation, and in the limit of no screening the resonator will instead work as a very good antenna.

As will be discussed further in Section 2.6, introducing any discontinuity or perturbation to the ideal CPW geometry will result in an increased dipole moment of the structure, and thus a lower $Q_{\rm rad}$.

2.2.2 Dielectric losses: two-level fluctuators

Dielectric substrates are characterized by their dielectric constant, which also has a complex part such that $\varepsilon = \varepsilon' + i\varepsilon''$. The the loss tangent is defined as $\tan \delta = -\varepsilon'/\varepsilon''$, and can be directly linked to the dielectric quality factor of the resonator:

$$Q_\epsilon = \frac{1}{\tan \delta}. \tag{2.22}$$

While this expression can be used to quantify the loss it does not tell much about the origin of the dissipation in the dielectric.

The dominant source of dissipation at low temperatures and low powers (single photon regime) in superconducting resonators are attributed to two-level fluctuators (TLFs). It has been shown that the contribution to TLF loss mainly comes from interfaces between the dielectric and the superconductor [34, 35]. Interestingly, for superconducting resonators it has been found [36, 37] that elevated temperatures may result in less dissipation since these TLFs get thermally saturated. Furthermore, because of the same saturation, the loss rate decreases with increasing energy stored in the resonator. The power dependence typically follows a phenomenological power law [38, 39]

$$Q_{\rm TLF}(P) = Q_{\rm TLF}^0 \left(1 + \frac{P}{P_0}\right)^\alpha, \tag{2.23}$$

where P is the internal power in the resonator, P_0 a material and geometry dependent saturation power, and α describes the strength of the coupling to the TLF ensemble. This type of loss is usually dominating in CPW resonators, and to reduce it the electric field strength across metal-dielectric interfaces should be reduced as much as possible [8].

2.2.3 Surface resistivity and kinetic inductance

Superconductivity is usually associated with zero resistance, but for higher frequencies superconductors still have an impedance which is not purely reactive. This can easily be seen

by deriving the Drude conductivity in the framework of the two-fluid model. Here it is assumed that the superconductor consists of both Cooper-pairs of density n_s and quasiparticles of density n_n, giving a total carrier density $n_t = n_s + n_n$. The following complex conductivity can then be derived, asuming that the relevant frequency is much smaller than the inverse scattering time, $\omega \ll \tau_n^{-1}$, for quasiparticles (typically valid for $\omega < 100$ GHz since $\tau_n \approx 10^{-12}$) and the scattering time for Cooper-pairs is assumed to be very long.

$$\sigma = \sigma_n + i\sigma_s = \frac{n_n e^2 \tau_n}{m_e} - i\frac{n_s e^2}{m_e \omega}. \tag{2.24}$$

In the dirty limit this results in a complex surface impedance

$$Z_s = \sqrt{\frac{i\mu_0 \omega}{\sigma_n + i\sigma_s}} = R_s + i\omega L_s. \tag{2.25}$$

The real part of the surface impedance gives rise to dissipation, while the imaginary part can be seen as an effective inductance, associated with the kinetic energy of the Cooper-pairs. From this complex impedance it is possible to derive expressions for the losses at finite temperatures [40–42].

$$Q_\sigma = \frac{\omega L_s}{R_s} = \frac{n_s}{n_n} \frac{Z_0}{\mu_0 \lambda_{\text{eff}}^2 \tau_n \sqrt{\varepsilon_r} \omega_0 cg}, \tag{2.26}$$

where g is a geometric factor obtained through conformal mapping [41]. For a thin-film we also note that the penetration depth in the limit $d < \lambda_L$, where λ_L is the London penetration depth, is given by $\lambda_{\text{eff}} = \lambda_L^2/d$. For a 50$\Omega$ CPW $g \approx 5$ while for a single superconducting strip $g = 2/\pi^2 \times \ln(4W/d) \approx 0.8$ for $W/d \approx 14$, as in our NbN fractal resonators (see end of this chapter). Since the currents in a CPW are more localized to the edges it will naturally result in increased resistive loss. From the BCS model we can also write down the temperatude rependence of eq. (2.26). The fraction of the superconducting and normal carrier densities follows the exponential dependence $n_s/n_n = \exp(-1.76T_c/T)$. The exponential supression of loss with temperature makes surface impedance comparable to other loss mechanisms only near $T = T_c$.

Another important effect of eq. (2.25) is that there is an excess inductance associated with the kinetic energy of the Cooper pairs. This kinetic inductance (per unit length) can be calculated from the kinetic energy of the Cooper-pairs.

$$L_k = \frac{\mu_0 \lambda_{\text{eff}}^2}{I_z^2} \int j^2(x, y) dx dy, \tag{2.27}$$

where $j(x, y)$ is the current density in the cross-section of wire carrying a total current I_z in the z-direction. For a CPW or a single strip it reduces to

$$L_k = \frac{\mu_0 \lambda_{\text{eff}}^2}{dW} g. \tag{2.28}$$

This should be compared to the geometric inductance obtained through conformal mapping

$$L_g = \frac{\mu_0}{4} \frac{K(k')}{K(k)}, \tag{2.29}$$

where K is the complete elliptic integral, $k = G/a$ and $k' = \sqrt{1 - k^2}$ The total inductance of a wire is then given as the sum of geometric and kinetic inductance.

$$L = L_g + L_k. \tag{2.30}$$

For resonators subjected to magnetic fields we should note that the observed quadratic shift in resonance frequency in magnetic field originates from the quadratic dependence of the kinetic inductance on magnetic field. From Ginzburg-Landau theory it follows that for a thin film, $d \leq \sqrt{5}\lambda_{\text{eff}}(B = 0, T = 0)$, $\lambda_{\text{eff}}(H) = \lambda_{\text{eff}}(0)(1 - \alpha H^2/H_{c||}^2)^{-1/2}$ [42, 43]. After a Taylor expansion this leads to

$$\frac{\omega(H) - \omega(0)}{\omega(0)} \approx -\alpha \frac{H^2}{H_{c||}^2} \frac{\beta \lambda_{\text{eff}}^2(0)}{L_g + \beta \lambda_{\text{eff}}^2(0)} = -\alpha \frac{H^2}{H_{c||}^2} \frac{L_k(0)}{L_g + L_k(0)}, \qquad (2.31)$$

where $\beta = L_k/\lambda_{\text{eff}}^2(0)$ is the geometric scaling factor for the kinetic inductance given by eq. (2.27), α is a proportionality constant, and $H_{c||}$ is the parallel critical field. From Mattis-Bardeen theory it follows that the zero-field zero-temperature kinetic inductance of a wire relates to the normal state resistance and the superconducting gap as $L_k(0) = \hbar R_n/\pi\Delta$ [44]. From a material where kinetic inductance dominates over geometric inductance (such as in NbN) we would expect to see a much stronger frequency shift with magnetic field, something that could become an issue for ESR-type experiments where the resonator is monitored over a large range of magnetic field. Nevertheless, as discussed in the next section, the best materials in terms of magnetic field induced losses typically comes with a large kinetic inductance. The specific measurement method that we have developed (described in Chapter 3) can conveniently be adapted to resolve this conflict.

2.2.4 Magnetic field-induced losses

This section aims to describe the effect of applying a static magnetic field to a superconducting resonator. In general, an applied field will suppress superconductivity at the edge of the superconductor on the length scale of $\lambda_L(B)$, which is increasing with applied magnetic field B. Thus, any current flowing near the edge of the superconductor will result in dissipation. For a (super-)conductor carrying a microwave current this becomes even more of an issue since the current will be localized to the edges of the conductor (skin-effect). We define a quality factor, Q_B, associated with the magnetic field-induced loss as

$$\frac{1}{Q_B} = \frac{1}{Q_i(B)} - \frac{1}{Q_i(B = 0)}, \qquad (2.32)$$

and in the rest of this section our aim is to derive an expression for Q_B. The main theoretical work was carried out by Norris [45] and later refined by Brandt and Indenbom [46] and generally the model is reffered to as the NBI model.

A single infinite strip (of width W and thickness d) of a superconductor carrying a current I_0 is subjected to a magnetic field. The NBI model explicitly treats the case of a DC current flowing in the strip, however, we are interested in the dissipation associated with the microwave currents in the strip. We may still apply the NBI model to evaluate this dissipation, but we have to consider the current density distribution of a microwave current in a coplanar geometry. For a superconducting coplanar geometry the current density in the conducting strip is given by [47]

$$j_{\text{CPW}}(x) = \frac{I_0}{K(W/a)W\sqrt{\xi(x)}}, \qquad (2.33)$$

where I_0 is the total current, $a = 2G + W$, $K(x)$ is the complete elliptic integral of the first

kind and

$$\xi(x) = \begin{cases} \frac{\lambda_{\text{eff}}}{W}[1 - (W/a)^2] & 0 \leq \frac{W}{2} - |x| < \lambda_{\text{eff}} \\ [1 - (2x/W)^2][1 - (2x/a)^2] & |x| \leq W/2 - \lambda_{\text{eff}} \end{cases} \tag{2.34}$$

While this is valid in the case of a CPW geometry we can easily evaluate the case of a single strip by taking the limit $a \to \infty$.

$$j_{\text{strip}}(x) = \frac{2I_0}{\pi W \sqrt{\xi_\infty(x)}}, \tag{2.35}$$

$$\xi_\infty(x) = \begin{cases} \frac{\lambda_{\text{eff}}}{W} & 0 \leq \frac{W}{2} - |x| < \lambda_{\text{eff}} \\ [1 - (2x/W)^2] & |x| \leq W/2 - \lambda_{\text{eff}} \end{cases} \tag{2.36}$$

Brojeny et al. [48] also derived approximate expressions for the current and magnetic field distribution in the case of two nearby remote strips carrying oppisite currents. These are considered in more detail in the context of ESR using the resonators developed in this thesis (Chapter 7). For the sake of this discussion we limit ourselves to the CPW and single strip geometry, the double strip geometry has little effect on the total Q_B in our devices.

In an applied magnetic field Abrikosov vortices are generated in the superconducting film. If, at the same time, the strip carries a current the vortex will be subject of a Lorentz force $F = j(x)\Phi_0 \sin(\omega t)$. In addition to this force there will be a restoring force due to the pinning potential of the vortex itself. The simplest model gives an equation of motion for the vortices $j(x)\Phi_0 \sin(\omega t) = \eta v$. This simple relation is valid if we consider weak microwave currents such that the the dynamics is not influenced by nonlinearities of the pinning potential; the vortices are just weakly disturbed from their equilibrium positions due to the driving force. The power dissipated is given by $P = Fv$ and due to the linear relationship between driving force and friction the energy dissipated per cycle of the driving force becomes proportional to $j(x)^2$

$$E(x) = \int_0^{2\pi/\omega} \frac{\Phi_0^2}{\eta} j(x)^2 \sin^2(\omega t) dt, \tag{2.37}$$

which can be associated with the change in quality factor of a superconducting resonator. In a macroscopic piece of superconductor the above approach becomes unfeasible since we have to sum up all the individual contributions from a large number of vortices located at different places and subjected to different microwave currents. To simplify the problem it is convenient to instead consider some continous vortex density distribution within the strip. The simplest model for the flux density would be a linear increase with magnetic field, starting at the edge of the strip at some critical field, and linearly increasing in both magnitude and penetration into the strip. This was first considered by Bean, and is commonly referred to as the Bean flux profile [49]. This model is suficcient to explain the most fundamental dependence of the dissipation on the magnetic field, however, a more accurate description is given by the NBI model. The central result is that the flux density inside the strip is [46]

$$H(x, H_0) = \begin{cases} H_c \text{arctanh} \frac{\sqrt{x^2 - \left(\frac{W}{2\cosh(H_0/H_c)}\right)^2}}{|x| \tanh(H_0/H_c)} & \frac{W}{2\cosh(H_0/H_c)} < |x| < \frac{W}{2} \\ 0 & \text{otherwise} \end{cases} \tag{2.38}$$
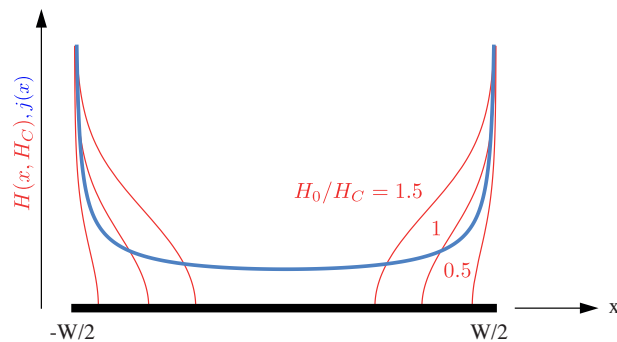
Figure 2.5: Flux density (red) for different applied fields (eq. (2.38)) together with current density eq. (2.35) in a superconducting strip of width W.

where H_0 is the applied field, and we define a critical field parameter $H_c = \mu_0 j_c d/\pi$ depending on the critical current density j_c of the superconductor. It should also be noted that both the magnetic field and the magnitude of the current influence the total flux density. However, in this case we consider the microwave currents to be small enough such that the dominant mechanism for flux redistribution is due to variations in magnetic field. The weak periodic driving merely assists the system into reaching an equilibrium configuration more efficiently. We can now set up an expression for the magnetic field induced dissipation per cycle

$$\frac{1}{Q_B} \propto E = \int_{-W/2}^{W/2} \int_0^L \int_0^{2\pi/\omega} |H(x, H_0)| j(x, z)|^2 \sin^2(\omega t) dx dz dt, \qquad (2.39)$$

where we also take into account the current distribution along the resonant structure. For the central line of a quarter wave CPW we can simply write $j(x, z) = j(x) \sin(\pi z/L)$ where L is the length of the resonator. In Fig. 2.5 the current density and flux density in the strip is shown as a function of applied magnetic field. Note that in a CPW geometry substantial contribution can also come from currents induced in the ground planes, which is not considered in the above expression. However, as described in Chapter 2 in the case of our fractal resonators this contribution can essentially be neglected.

It is evident that a very big problem for superconducting strips in magnetic fields carrying microwave currents is that not only is the current density peaked at the edge of the strip, but the vortex density is also the highest in the same region. It is thus very easy to arrange a significant amount of dissipation.

2.2.5 Flux focusing

Another effect that has to be taken into account is flux focusing. It is a direct result of the Meissner effect and for a superconductor in an external magnetic field the field strength will be increased close to the edges of the superconductor. For a single remote strip this is accounted for in the NBI model discussed in the previous section. However, in for example a CPW structure, ground planes can be very large and the expelled field will be localized to the narrow slots between ground planes and center conductor. The effective magnetic field in the resonator can be several hundred times larger than the actual applied field [50], thus increasing the dissipation substantially.

In this situation introducing holes in the ground plane will not improve the situation. Such holes will lead to vortex pinning and reduced dissipation, but will not reduce effects

of flux focusing. The only way to reduce flux focusing is to reduce the amount of superconductor in the device, minimize its filling factor and make sure that there is always an open path (not enclosed by superconductor) for flux to escape the structure.

2.2.6 Techniques for reducing magnetic field induced losses

Several techniques have been developed to improve the quality factors in magnetic fields. The general approach has so far been to trap vortices that have entered the superconducting film by artificially creating pinning centers. Such pinning centers usually involve holes in the ground plane on the length scale of the magnetic penetration depth λ_L [51–53] or slots in the center conductor [54, 55]. The main purpose is to create a strong pinning potential for vortices such that the trapped vortices are no longer perturbed by microwave currents, reducing dissipation. Note that such pinning is not explicitly taken into account in eq. (2.39), but it will result in a reduced proportionality constant.

Another common approach is to reduce the width of the conducting strip. The effect of this is that the vortex entry field is increased [56]:

$$H_S^\perp \approx \frac{\Phi_0}{2\pi\lambda_{\text{eff}}\xi}\sqrt{\frac{2d}{\pi W}}. \tag{2.40}$$

Similarly for fields parallel to the film the dynamics are different and we can use the bulk critical field [42, 57, 58]

$$H_S^\parallel \approx H_c = \frac{\Phi_0}{2\sqrt{2}\pi\lambda_{\text{eff}}\xi}. \tag{2.41}$$

This field can be interpreted as the field required to suppress the free energy barrier for vortices to enter the center of the strip [57]. At lower fields vortices tend to locate to the edge of the strip (as is also seen in eq. (2.38)). Qualitatively we can think of the vortex as experiencing the field and currents from an image vortex outside the strip, similar to the method of image charges. Physically this is justified by the current circulating the vortex, which close to the edge of the strip becomes deformed from its otherwise circular pattern. There is thus a net attractive force pulling the vortex towards the edge of the strip, and to overcome this 'barrier' and escape the image potential a substantial magnetic field has to be applied. $H_S^\perp$ is the field at which this barrier is completely suppressed.

As discussed in [Paper I], the dissipation caused by magnetic field can be divided into two categories: edge dissipation and bulk dissipation. It turns out that the former is independent of strip width W, while the latter is not. $H_S^\perp$ defines the cross-over field where bulk dissipation starts to dominate over edge dissipation. Thus, reducing the width of the strip will increase the field that results in bulk dissipation, however, once the vortices enter the strip they will result in more dissipation for a narrow strip since the current density is increased. This is also important in the fractal geometry since we here predominantly rely on edge dissipation for enhanced field performance.

The choice of superconducting material also becomes important. For example, for NbN the product $\lambda_{\text{eff}}\xi$ is roughly 4 times smaller as compared to Nb thin films. This number qualitatively agrees with the observed performance of fractal resonators made from these two materials, discussed later in this chapter. Also using thin films in the dirty limit, where the mean free path is shorter than the coherence length, will reduce the effective coherence length and increase $H_S^\perp$, but this becomes unpractical for NbN since $\xi < 5$nm. Another common material used for high-Q CPW resonators is $\text{Nb}_{1-x}\text{Ti}_x\text{N}$, which when

	Al	Nb	NbN	NbTiN
Δ [GHz]	90	700	750	700
$\lambda_L(0)$ [nm]	16	95	194	500-230
ξ [nm]	1600	39	$4-5$	3.8
$\lambda_{\text{eff}}\xi^{\dagger}$ [nm^2]	$2.5 \cdot 10^4$	3700	$\gtrsim 780$	$\gtrsim 875$
T_c [K]	1.18	9.25	16	18
H_{c1} [T]	$H_c = 0.01$	0.17	0.004	0.028
H_{c2} [T]	-	0.4	15-20	14

Table 2.1: Thin-film properties of some superconducting materials commonly used for superconducting resonators. † Assuming $d = 140$ nm. Data collected from refs. [53, 59–62].

optimized shows similar magnetic field properties as compared to NbN [59]. Some properties of commonly used materials are summarized in Table 2.1.

2.3 Design of the fractal resonator

Having discussed some of the most important properties of resonators for our applications this section now aims towards outlining the technological requirements set by the two main applications considered in this thesis, NSMM and ESR. The fractal resonator is presented as the solution to most of these problems and the details of its design and operation is discussed. From our applications we can set up the following requirements for the resonators:

- For NSMM applications we cannot have very large ground planes, which for a CPW resonator would increase radiation losses significantly.

- The above condition requires that the total intrinsic dipole moment of the resonant structure should be very small.

- The resonator have to be compact so it can be integrated with an AFM probe.

- For NSMM we want an electrical probe (tip) and thus we cannot couple the resonator to the same voltage maximum in the resonator: we need to use inductive coupling.

- For magnetic field applications we identify that dissipation originates from the currents flowing in the structure and scales as $P \propto I^2$. It would therefore be advantageous to split the same total current into several parallel branches.

- Narrow superconducting strips will push bulk induced dissipation to higher fields.

- Symmetry must be maintained such that we can DC-bias the resonator without introducing radiation losses.

The final design is inspired by its mechanical analog of a tuning-fork (discussed in Chapter 4). Its derivation from a piece of transmission line of length $\lambda/2$ is shown in Fig. 2.7, and is described in detail in [Paper I]. The final structure has an increased capacitance per unit length which results in a reduced propagation velocity in the structure. By fine-tuning the geometry it is thus possible to design a resonator of given frequency *and* physical length while maintaining a distributed mode. This enables easy integration of the resonator onto
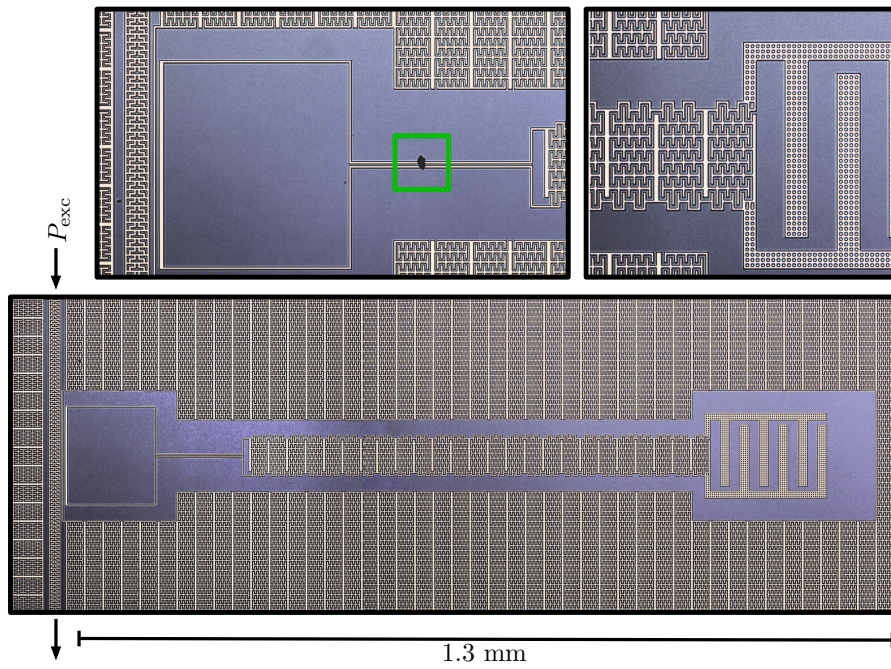
Figure 2.6: Optical image of the fractal resonator.
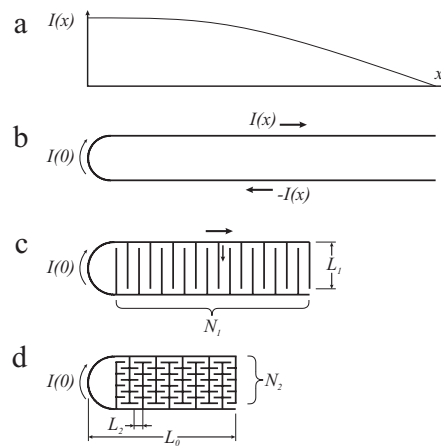
Figure 2.7: a) Current distribution along the resonant structure shown in b-d. b-d) evolution of the folded half-wave strip into the fractal geometry.

an AFM probe, and as will be discussed later it is also of great importance for applications requiring magnetic fields.

The name 'fractal resonator' may seem a bit of a stretch if only looking at the geometrical design of the structure. A fractal structure generally is self-repeating and looks the same no matter at what length-scale it is observed. Geometrically this only applies to one dimension of the structure. If we instead consider the distributed circuit-representation of the resonator each fractal iteration can be seen as a set of inductors connected in parallel, and each inductor is also capacitively connected in series to its neighbors. This schematic repeats itself for any interation of the 'fractal', albeit in the presented design it is limited to three iterations.

2.4   Magnetic field properties

We will now try to put the properties of the fractal resonator in magnetic fields in relation to the standard CPWR geometry (and also compared to lumped element resonators). We start by looking at the current density in different parts of the fractal structure. While in a $\lambda/2$ CPWR the current scales with coordinate (x) as $I(x) = I_0 \sin(2\pi x/\lambda)$, the situation in the fractal geometry is much more complex. However, what is clear is that only the main branches carry a significant current, and this current is then divided among higher order branches.

If we assume that the current density is homogeneous across the section of superconducting strips, as well as along the strips length (which is actually a very rough assumption that we will refine later) then the total dissipation is

$$P_{\text{fractal}} \approx p_0 \left[L_{0,\text{eff}} + \frac{L_1}{N_1} + \frac{L_2}{N_1 N_2} + \frac{L_3}{N_1 N_2 N_3} + ... \right], \tag{2.42}$$

where p_0 is the dissipation per unit length of a superconducting line and N_k is the number of sub-branches of the k-th order. In our designs we have $N_k = [N_1, 6, 8]$, where the frequency of the resonator is adjusted by varying the number of segments N_1, typically in the range 8-14 for frequencies between 4-8 GHz. The major contributions to dissipation thus come from the first term in eq. (2.42).

We can refine the above expression by considering also how the current is distributed along each branch. For the first branch we expect a half-sinusoidal dependence on the current versus coordinate. This is somewhat distorted by the splitting of the current into higher order branches but as a relatively good approximation we can write $I_0 = I \sin 2\pi x/\lambda$.

For higher order branches we can treat the current distribution along each line as constant. This approximation is justified as a result of the fractal structure itself: each high order branch is neighboring branches of lower order. The result is that the current distribution becomes more uniform throughout the center of the fractal capacitor in an effort from the structure to minimize its own dipole moment. This approximation becomes more accurate as the order of the fractal capacitor is increased. We may also put this discussion in the context of other similar resonators commonly used in literature. The closest example is the lumped element resonator, which closely resembles the first iteration of the fractal resonator, Fig. 2.7c, (but with a longer inductive part). In such a structure the only two existing branches are orthogonal and cannot compensate for dipole moments generated in the opposite branch. For this to happen the 'fractal order' has to be increased at least once more. For the second interation in Fig. 2.7d branch 0 and branch 2 become parallel, and actively participate in cancelling the total dipole moment of the device. This increases the effectiveness of the current branching into the center of the fractal structure and reduces the current in the main branch.

This discussion is supported by our numeric simulation presented in Fig. 2.8. The current density in the first branch is reduced more than an order of magnitude as compared to the main branch. It is also clear that the second order branch which runs parallel and nearby the main branch has a somewhat elevated current density, a signature of the increased effectiveness of the current branching for higher order fractal structures. Increasing the fractal order even further would improve the performance in magnetic field, but with the third order shown in Fig. 2.6 we have reached the limit of what is practical considering lithographic techniques used to pattern the superconductor. However, as discussed, the
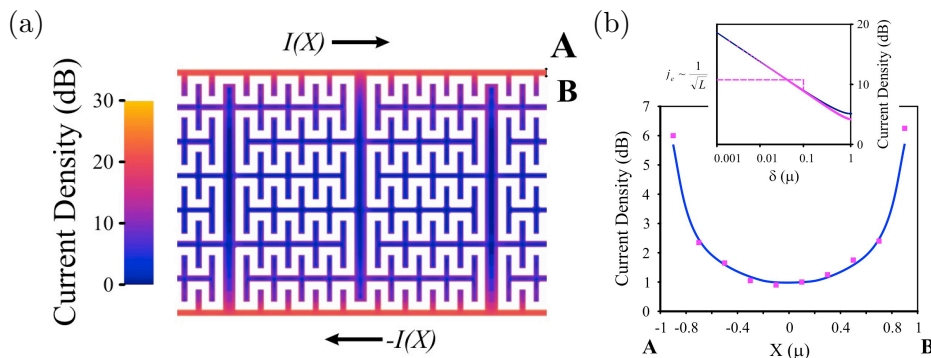
Figure 2.8: a) Numerically calculated current distribution in a segment of the fractal resonator. Simulations were done using AWR Microwave Office and the EMsight simulator. Note that the current in the secondary brances is around 20-23 dB lower than in the primary branch, consistent with the division of the main current into $N \sim 10$ branches. b) Current density along the cross-section of the fractal main branch (points A to B in the top panel). Points are extracted from simulation and solid line is calculated using eq. (2.35). Inset: Current density at a distance δ from the edge of a single strip (blue) and a equivalent coplanar strip (purple) for an ideal conductor. Dashed line indicates the simplest model for a superconductor with a constant density up to the penetration depth λ_L.

major advantage of the fractal structure already comes when going from the structure shown in Fig. 2.7c to the one in Fig. 2.7d.

It should also be noted that a lumped element resonator would outperform a CPWR in magnetic fields since it shares some characteristics of the 'fractal' design such as narrow strips and somewhat reduced flux focusing. However, a lumped element design should be regarded as a zero-dimensional resonator, and is thus less applicable for large scale QIP applications, where a one- (or multi-) dimensional resonator can transfer information in real space, and operate at different resonance modes.

We observe higher harmonics in our fractal resonators. For example, the $3\lambda/2$-mode has a frequency $f_3 = \alpha f_1$, where $\alpha = 3.1 - 3.4$ for N_1 ranging between 14 and 7, an indication of a small deviation from being a purely distributed resonance mode.

Having established that the main part of the dissipation in the fractal structure comes from the main branches (c.f. eq. (2.42)) and that the main branch can be reduced an order of magnitude in length for the fractal design, the next question is how we can compare the measured dissipation in the fractal against CPW geometries found in literature. From the detailed discussion in [Paper I] we come to the following conclusions.

- The current distribution in the main branches of the fractal resonator can be treated as the current distribution of a single, remote strip. The screening currents in the higher order branches only perturbs the main branch slightly, and they can be neglected.

- A single remote strip of width $W = 2\mu$m has a current distribution which is equivalent to a CPW of width $W = 2.3\mu$m. (See also Fig. 2.8b)

- The dissipation can be divided into two terms, edge and bulk dissipation for which the cross-over is defined by eq. (2.40). The former does not depend on the width of

the strip:

$$P_e = \int_0^{\lambda_{\text{eff}}} B(x/W)j_e^2 dx \sim I^2 \int_0^{\lambda_{\text{eff}}} B(x/W)d(x/W). \tag{2.43}$$

while the bulk dissipation scales as W^{-1}:

$$P_b \sim \frac{I^2}{W} \int_{-W/2+\lambda_{\text{eff}}}^{W/2-\lambda_{\text{eff}}} B(x/W)\frac{1}{1-(2x/W)^2}d(x/W). \tag{2.44}$$

This means that if we were to compare the fractal resonator to a CPW of arbitrary width W for fields below $H_S^{\perp}$ or $H_S^{\parallel}$ the fractal structure dissipates $L_{\text{CPW}}/L_{0,\text{fractal}} \approx 10$ times less (asuming no flux focusing), but for fields $H > H_S^{\perp}$ or $H > H_S^{\parallel}$ the scaling factor is instead $(L_{\text{CPW}}/L_{0,\text{fractal}}) \times (W_{\text{CPW}}/2.3)$. This factor 10 improvement due to current branching is a straightforward but naive estimation, and several factors contribute to an actual scaling factor that is lower. For example, the impedance of the fractal resonator is $Z \approx 30\ \Omega$ (determined through numerical simulations), i.e. the total inductance of the resonator is reduced by roughly a factor 2.6. This means that the current in the structure is reduced a factor $\sqrt{2.6}$ for a given number of photons in the cavity. The length of the coupling loop also constitutes a part of the resonator where effects of current branching do not apply.

2.5 Results: magnetic field performance

We used Nb resonators to be able to better make a comparison with existing experiments on resonators in magnetic field found in literature [51–53]. High quality Nb is relatively easy to obtain, and it has relatively good magnetic field properties as well as low microwave losses. However, our recently developed high quality NbN thin-films has shown much better field properties and comparable microwave losses. In the next section some of the results obtained with NbN are discussed.

2.5.1 Nb resonators

The main result is presented in Fig. 2.9 for parallel and perpendicular field orientations. The main findings are (see [Paper I] for detailed discussion):

- By comparing the data in Fig. 2.9b and 2.9d to theoretical predictions of $H_S^{\perp}$ and $H_S^{\parallel}$ it is possible to estimate the flux focusing factor. We arrive at $k \approx 3$. This is up to 100 times lower than for a CPWR [50]. For perfectly aligned parallel fields this does not contribute to the performance of the devices, but as soon as there is the slightest misalignment of the field, the small perpendicular component will be enhanced k times. For such small k we do not have to align the resonators very carefully.

- Q_B is power independent over a wide range of powers, even down to single photon population, extending the results from Ref. [47] and [51].

- In the given temperature range of 20 mK to 1.8 K Q_B is at most only weakly dependent on temperature.

- For perpendicular fields the loss rate is around one order of magnitude lower at ~ 5 times higher magnetic fields than previously reported [51]. Qualitatively this factor
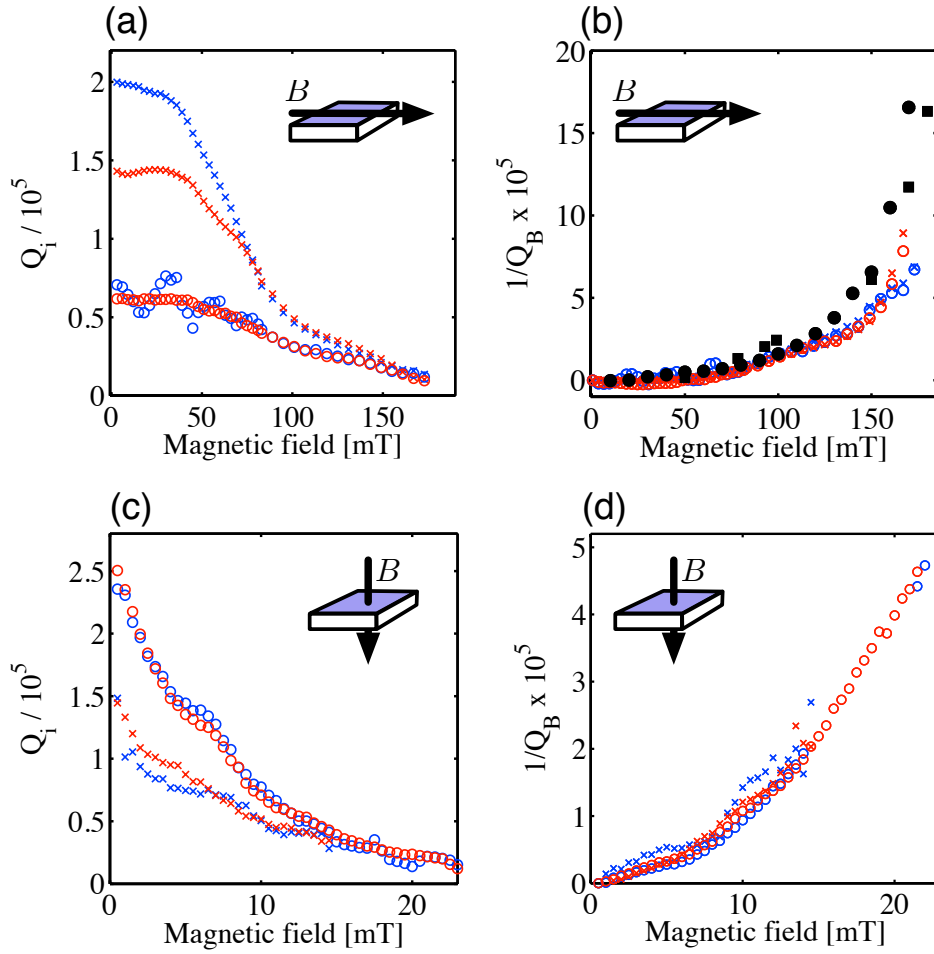
Figure 2.9: a-d) Resonator response to external magnetic field. Different colors indicate a different resonator. The data in this figure comes from a fractal resonator with a ground configuration of type "B", discussed later in Sec. IV.3. a) Internal quality factor for in-plane magnetic field. b) Extracted field induced energy loss $1/Q_B$ for the same measurement. In both a) and b) circles indicate measurement performed at low power (-143 dBm) and crosses at high power (-108 dBm). (■) and (●) indicates measurements performed at T=1.8K and -70 dBm for two resonators identical to the ones measured at 20 mK, but from a different wafer. c) Internal quality factor for normal-to-plane orientation of the magnetic field. d) Q_B^{-1} for normal-to-plane orientation of the magnetic field. In both c) and d) applied powers are -105 dBm (○) and -70 dBm (×).

of 50 is expected from the roughly 10 times lower flux focusing factor in the fractal geometry compared to Ref. [51], combined with the expected ∼ 10 times reduced dissipation in the fractal resonator.

• For parallel fields we assume no flux focusing and the observed quality factors in Fig. 2.9 is roughly 10 times higher than previously reported [53], mainly due to current branching.
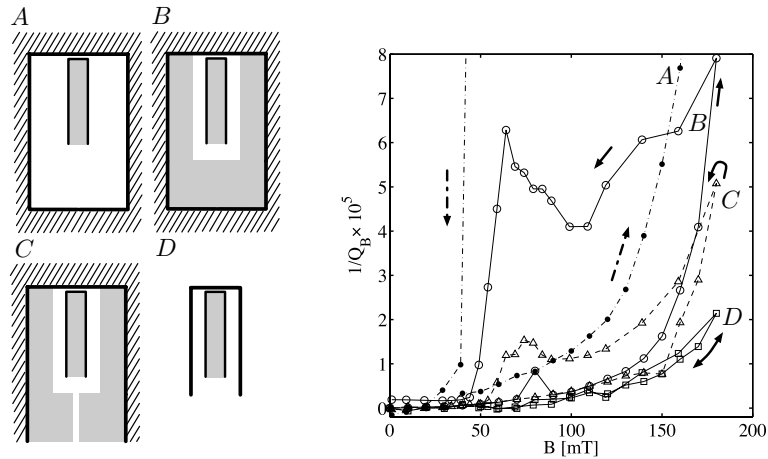
Figure 2.10: Magnetic field dependence of the loss rate for four different ground plane topologies. Grey areas are a fractal-type structure while hatched areas and solid lines indicate solid ground planes.

2.5.2 Ground plane optimization

Before moving on to other materials more suitable for extreme field performance, we also looked at how the ground plane around the resonator contributes to the loss in magnetic fields. The design details are again outlined in [Paper I]. We look at the quality factor of the resonator when (i) a solid ground plane is present nearby. (ii) a perforated ground plane for vortex pinning, similar to Refs. [38, 63]. (iii) a fractal style ground plane having a large capacitance, appearing transparent at microwave frequencies but with a continous path for flux to escape the structure, reducing flux focusing. (iv) Essentially no ground plane at all (the NSMM design). These situations are conceptually shown in Fig. 2.10 together with the obtained results. We identify two important design considerations. Removing the ground planes decrease the zero field Q_i. This is expected since radiation losses increase as a result of the reduced screening. However, since the total dipole moment of the fractal resonator is relatively small, removing the ground is by far not as detrimental as it would be for a CPWR. This is discussed further in Section 2.6. Removing the ground planes significantly reduces the hysteretic effects observed when sweeping the magnetic field back and forth. This is mainly due to reduced flux focusing.

2.5.3 NbN resonators

Having demonstrated the advantages of the fractal design using Nb resonators we can change to a material with higher critical field H_c. Due to the available materials in our cleanroom we resorted to NbN. As expected this significantly increases the onset of strong dissipation compared to Nb, and our NbN resonators can be applied in fields up to 400 mT without significant change in quality factor, as shown in Fig. 2.11. At zero field and 300 mK these resonators show exceptionally high internal Q in the range $1 \cdot 10^6 - 3 \cdot 10^6$, limited by dielectric losses. The exceptionally good resilience to magnetic fields of these resonators makes them suitable for a wide range of measurements, for example as a way to interrogate very small number of free spins. Conventional X-band ESR spectrometers require magnetic fields up to ~350 mT for free spin interrogation, which in our case now becomes possible with more than two orders of magnitude higher Q compared to standard dielectric resonators in ESR
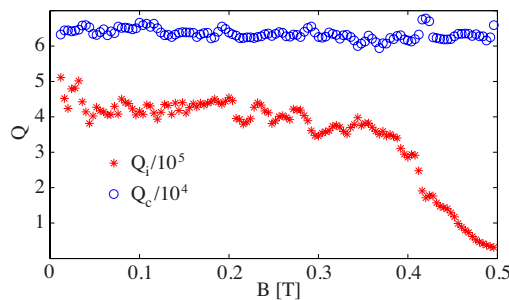
Figure 2.11: Quality factor versus parallel magnetic field for a typical fractal resonator made of NbN on sapphire, measured at 1.8 K.

spectrometers [64]. This will be discussed further in Chapter 7.

2.6 DC-biased fractal resonators

Added functionality becomes more and more important for circuit-QED applications as new physical systems are explored for promising applications within circuit-QED. Storing quantum information in spin degrees of freedom has potential to be advantageous since some spin systems can have very long coherence times [18]. However, one technological limitation is that spins typically are manipulated using strong magnetic fields making it difficult to achieve fast and local tuning. To this end there is a growing interest in exploring a new class of spin systems that would allow for interaction of spin degrees of freedom with electric fields. Specifically, we are interested in molecular compounds that have been chemically engineered to have a spin-orbit coupling which can be tuned by electric fields [19, 65–69]. This means that the resonance between the resonator and the spin system can be shifted both magnetically and electrically.

The specifics of some of these molecules will be discussed further in Chapter 7, in this section we will only keep in mind one important requirement: In many cases this type of tuning requires a static electric field across the molecular crystal on the order of $10^6 - 10^8$ V/m. Typically the electric field dependence in these molecules enters the Hamiltonian orthogonal to the magnetic coupling. An ideal solution would therefore be to have the DC electric field generated in the same leads that carry microwave currents. To produce electric fields of this magnitude requires electrodes to be separated by only a few μm. Incorporating dedicated probes into the microwave circuit becomes then rather difficult since they tend to couple strongly to the microwave field and they will thus introduce significant dissipation. As discussed in Sec. 2.2.1 any disruptions to a CPW resonator will result in a dipole moment of the total structure that leads to radiation losses. A few different approaches to introducing DC bias have been demonstrated. This includes connecting high-impedance lines to low impedance points in the resonator [70, 71] or to couple DC lines via band-stop filters [72].

Here we instead chose a different approach: to split the resonant structure itself into two parts which are not electrically connected at DC. The general concept is presented in Fig. 2.12c and in [Paper V]. Each segment is connected at its voltage node to the ground. Due to the low dipole moment in the fractal structure this connection does not result in significant dissipation. Furthermore, the ground plane is divided into two parts that can be electrically biased. The ground is still transparent for microwaves since the two planes
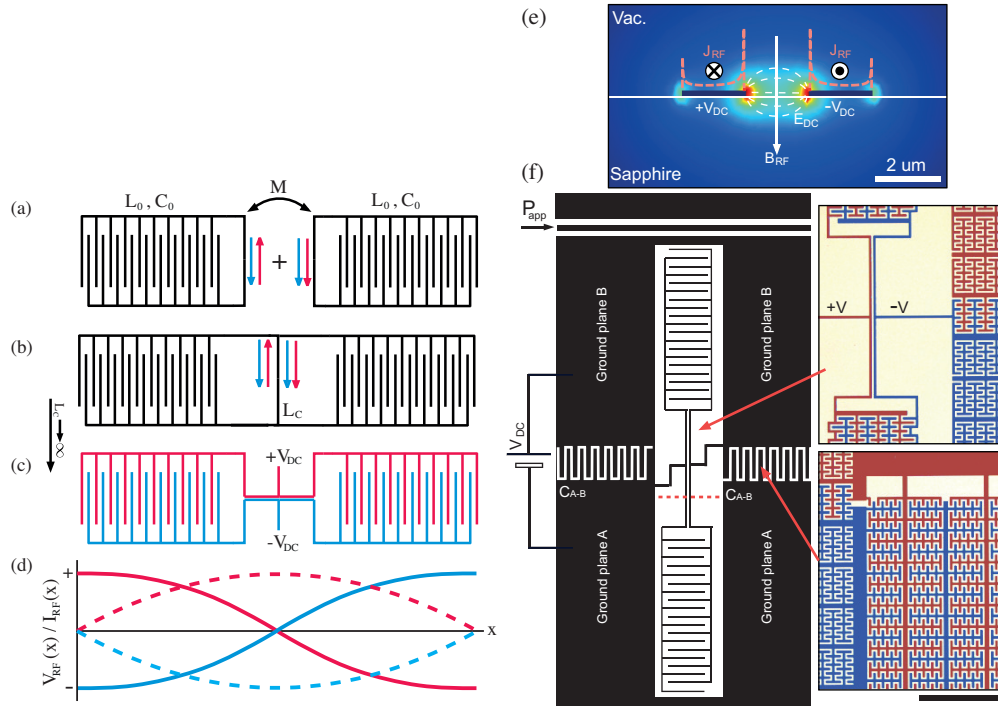
Figure 2.12: a) Two identical resonators coupled through a mutual inductance M. Direction of currents for the two modes (red, blue) is indicated by arrows. b) Two identical resonators coupled through a shared inductive link with inductance L_C. c) the resonator in b) in the limit $L_C \to \infty$, forming two galvanically split segments of the resonator to which a DC bias can be applied. One resonance mode persists with voltage and current distribution shown in d). e) Magnetic field density in a cross section near the voltage node of the resonator. f) Sketch of the resonator and its surrounding split ground planes. Scale bar is 60 μm.

are interconnected by a dense large area capacitance. Electric and magnetic fields thus get localized to the *same* volume in space, maximizing the magnitude of both. For a single spin placed in the center between the two conductors of the resonator the magnetic and electric fields are orthogonal.

The final design can be derived from two coupled resonators in Fig. 2.12a, where the two resonators are coupled through the mutual inductance $M = kL_C$ where L_C is the inductance of the individual (identical) coupling segments and k the coupling strength. It results in the following coupled equations.

$$C_0\dot{V}_1 + I_1 = 0, \tag{2.45}$$
$$L_0\dot{I}_1 - V_1 = -M\dot{I}_2, \tag{2.46}$$
$$C_0\dot{V}_2 + I_2 = 0, \tag{2.47}$$
$$L_0\dot{I}_2 - V_2 = -M\dot{I}_1. \tag{2.48}$$

With solution

$$\omega_\pm = \frac{1}{\sqrt{C_0(L_0 \pm M)}}. \tag{2.49}$$

In the situation depicted in Fig. 2.12b the two resonators instead share the common induc-

tance L_C, and we get

$$C_0 \dot{V}_1 + I_1 = 0, \tag{2.50}$$
$$(L_0 + L_C)\dot{I}_1 - V_1 = -L_C \dot{I}_2, \tag{2.51}$$
$$C_0 \dot{V}_2 + I_2 = 0, \tag{2.52}$$
$$(L_0 + L_C)\dot{I}_2 - V_2 = -L_C \dot{I}_1. \tag{2.53}$$

The above equations have the solution

$$\omega_\pm = \frac{1}{\sqrt{C_0(L_0 + L_C \pm L_C)}}. \tag{2.54}$$

Thus, for the two modes we see that there exists a symmetric mode (blue arrows in Fig. 2.12b) where the currents in the common link add together in phase and the mode experience the additional inductance $2L_C$. However, for the antisymmetric mode (red arrows) the currents in the link are out of phase, cancelling each other resulting only in the fundamental frequency $\omega_- = 1/\sqrt{L_0 C_0}$. Thus in the limit $L_C \to \infty$ it follows that $\omega_+ \to 0$ and we are only left with one mode ω_-. This is the step we take in order to arrive at the design in Fig. 2.12c, which have a fundamental mode (ω_-) with current and voltage distribution as shown in Fig. 2.12d.

The measurements on several of these resonators are presented in [Paper V] and we see that the introduced DC bias works very well. We maintain the high Q-factors ($Q_i > 10^5$) that we see for the standard fractal resonator, which is limited by dielectric loss. This is a significant improvement from earlier studies where resonators were limited by large radiation losses as a result of the DC bias connection [70, 72].

2.7 Summary and outlook

In this chapter we have outlined the design and performance of fractal resonators which show very low loss rates in strong magnetic fields. We have discussed the main reasons for this enhanced performance and concluded several design aspects that should be considered to improve the performance in magnetic fields.

There is still, however, much room for improvement. While materials optimization is one key component to achieving high Q, we can also improve the fractal design by going to smaller length scales and even more reduced flux focusing. Eventually, this may lead to new interesting experiments where high-field physics can be integrated with superconducting resonators, for example quantum Hall effect.

We then moved on to include more functionality in the resonator: DC bias. This extends the number of available quantum systems that we can integrate with the resonator to get added functionality in a circuit-QED toolbox. In Chapter 7 we discuss some of the novel systems that we can start to explore.

It should be noted that not only voltage bias can be introduced in the way we demonstrate in [Paper V], but also DC current bias, by connecting another set of probes to the voltage nodes of the $3\lambda/2$-mode of the same structure. As another interesting application the resonator shown in Fig. 2.12b can also be used in the limit $L_C \ll L_0$. Here the two modes are split in frequency by a small amount and they share exactly the same electrical mode volume (neglecting the tiny electric fields in the common link). The two modes could thus be used to interrogate the linewidth of a coupled TLF ensemble in the substrate, by pumping one mode and monitoring the other for TLF saturation effects.

3
MEASUREMENT TECHNIQUES

The most straightforward way to measure the properties of a resonator at GHz frequencies is to use a Vector Network Analyzer (VNA) to directly measure S_{21} (eq. (2.12)). However, this method is very slow and not very suitable for real-time applications. Due to being very slow it tends to average over a large amount of low-frequency drifts and fluctuations which can result in a less precise measurement. For ESR, and especially for NSMM applications we would like to have a precise and fast way of reading out the state of a resonator, and we also need to have a wide dynamic range in frequency, much wider than the resonance linewidth so that it is possible to track large perturbations to the resonance.

For many measurements done in this thesis we have used a technique called Pound-Drever-Hall (PDH) locking to accurately track the central frequency of a microwave resonator. While originally developed for microwave oscillators [73], this technique is today commonly used in optics for frequency stabilization in for example lasers. For a review see for example Ref. [74]. Typically the PDH locking technique is used for high power applications at optical frequencies, but it was recently demonstrated in the very low power regime for microwave frequencies [75], and thanks to its excellent stability it has successfully been used to measure sub-Hz noise in superconducting resonators [36, 37], showing that superconducting resonators also exhibit $1/f$ noise. The advantage of this technique is that it can be used to very accurately measure the frequency of any device with a nonlinear phase response in real time. In fact, the bandwidth is limited only by the low frequency control electronics, typically working up to 100 kHz, and in our case tracking is limited by the feedback circuit which has a 5 kHz bandwidth. As will be shown in this chapter, the frequency accuracy can be made very high, typically by sacrificing dynamic range of the frequency measurement and we may also modify this technique to also allow for fast measurements of the quality factor of a resonator, i.e. its dissipation.

This chapter is organized as follows. First we take a look at other techniques commonly used to read out resonators, namely homo- and heterodyne detection techniques, and discuss their shortcomings to motivate the use of the PDH technique. The general theory behind the PDH technique applied to a microwave resonator measured in transmission is then outlined in Sec. 3.2. In Sec. 3.3 we conclude the theoretical overview by deriving the theory and discuss the implications behind the extended q-PDH technique used to simultaneously measure the quality factor. The actual measurement setup used is presented in Sec. 3.4.

3.1   Homodyne and Heterodyne detection techniques

The two most commonly used techniques for measuring the amplitude and phase of a high frequency signal are homodyne and heterodyne detection. The former, being the simplest
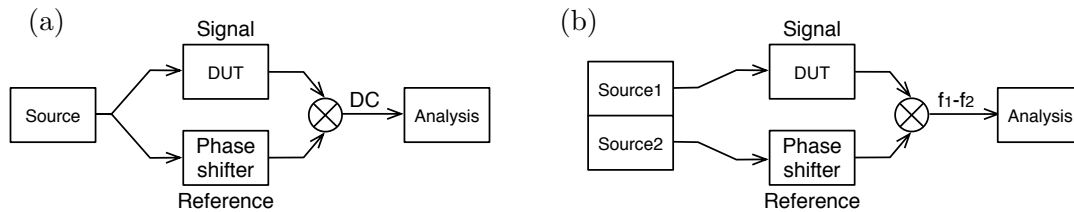
Figure 3.1: Basic schematics of (a) Homodyne detection and (b) Heterodyne detection (downconversion).

to realize, downconverts the signal of interest by mixing it with a reference signal generated by the same source (see Fig. 3.1a). This way the phase response of the DUT is recovered by measuring the phase difference $\delta\phi$ between the two paths and it results in a DC output from the mixer $V_{\mathrm{DC}} = A_{\mathrm{DUT}}A_{\mathrm{ref}}\cos{(\delta\phi)}/2$. This method will suffer from low frequency noise from the mixer and following amplifier chains and it is also susceptible to amplitude and phase fluctuations in each path. It is possible to overcome some of the limitations of this setup by downconverting the measured signal to a non-zero frequency. This technique, known as heterodyne detection is shown in Fig. 3.1b and mixes the signal from the DUT with a different frequency, coming from a different (phase locked) source. In this way the phase response of the DUT can be encoded in the amplitude of a signal with frequency $f_1 - f_2$ well above the cut-off frequency for low frequency noise. Sampling using high-frequency digital electronics can then recover the response from the DUT. Both these techniques suffer from fluctuations in the signal and reference lines which are not correlated. Especially in cryogenic environments, this can become an issue. For example, gradual shifts in liquid helium levels leads to changing phase response of coaxial lines. In order to track a resonance on a frequency scale much larger than the resonance linewidth some kind of feedback has to be implemented that shifts the source frequency. While this easily can be implemented for both of these techniques, it naturally comes into the Pound-Drever-Hall method described in the next section.

3.2 Pound-Drever-Hall locking on a superconducting resonator

The Pound-Drever-Hall (PDH) technique can be thought of as a type of heterodyne detection, but rather than feeding a mixer with two separate signals the PDH technique uses a phase modulated (PM) signal. A square law detection (self-mixing) results in an interference between the PM sidebands and the main signal. This resulting interference signal is then fed to control electronics that strive to obtain complete destructive interference. One major advantage of using this technique in a cryogenic environment is that any phase shift caused by, for example, a temperature change along the coaxial lines will affect *both* the carrier and the "reference" signal in a similar way. Many other potential sources of noise also become correlated and cancel out.

To understand the basics behind PDH locking we start by considering a phase modulated signal and then pass this signal through a resonator. In general a PM signal can be written

$$E = E_0 e^{i\omega t + \beta i \sin \Omega t}, \tag{3.1}$$

where ω is the carrier angular frequency, $\Omega/2\pi$ the phase modulation frequency and $\beta =$

$A_m D_p$ the modulation depth given by the modulation signal amplitude and the sensitivity of the modulator respectively. For all t and β we can rewrite this expression using the Jacobi-Anger expansion

$$E = E_0 e^{i\omega t} \sum_{n=-\infty}^{\infty} c_n e^{in\Omega t}, \qquad (3.2)$$

with coefficients that can be expressed as Bessel functions

$$c_n = \frac{1}{2\pi} \int_{-\pi}^{\pi} e^{i(\beta \sin\theta - n\theta)} d\theta = J_n(\beta). \qquad (3.3)$$

To first order we end up with

$$E \approx E_0 \left[J_0(\beta) e^{i\omega t} + J_1(\beta) e^{i(\omega+\Omega)t} - J_1(\beta) e^{i(\omega-\Omega)t} \right] = E_0 e^{i\omega t} \left[J_0(\beta) + 2i J_1(\beta) \sin\Omega t \right]. \qquad (3.4)$$

Higher order terms can usually be neglected if the modulation depth is relatively small since $|J_n| \to 0$ as $n \to \infty$. Sending this signal through some device to be measured, in our case the resonator, will give the following output

$$E_{trans} = E_0 \left[S(\omega) J_0(\beta) e^{i\omega t} + S(\omega+\Omega) J_1(\beta) e^{i(\omega+\Omega)t} - S(\omega-\Omega) J_1(\beta) e^{i(\omega-\Omega)t} \right], \qquad (3.5)$$

where $S(x)$ is the transmission through the resonator at frequency x. The signal is then detected in a high frequency power diode. This is a nonlinear detector, resulting in mixing of all involved frequency components. The incident power is $P_{trans} = |E_{trans}|^2$

$$\begin{aligned} P_{trans} = {}& P_0 J_0^2(\beta) S^2(\omega) + P_0 J_1^2(\beta) \left[S^2(\omega+\Omega) + S^2(\omega-\Omega) \right] \\ &+ 2P_0 J_0(\beta) J_1(\beta) \Big[\mathrm{Re}\left[\mathrm{S}(\omega)\mathrm{S}^*(\omega+\Omega) - \mathrm{S}^*(\omega)\mathrm{S}(\omega-\Omega) \right] \cos\Omega t \\ &+ \mathrm{Im}\left[\mathrm{S}(\omega)\mathrm{S}^*(\omega+\Omega) - \mathrm{S}^*(\omega)\mathrm{S}(\omega-\Omega) \right] \sin\Omega t \Big] \\ &+ 2\Omega \text{ terms.} \end{aligned} \qquad (3.6)$$

Here we are now interested in the two terms oscillating with frequency Ω. If we assume that the sidebands do not enter the resonator (the phase modulation is invasive and does not pump extra energy into the resonator) the value of $S(\omega \pm \Omega)$ is very close to unity. Then we have

$$S(\omega)S^*(\omega+\Omega) - S^*(\omega)S(\omega-\Omega) \approx S(\omega) - S^*(\omega) = 2i\mathrm{Im}[\mathrm{S}(\omega)], \qquad (3.7)$$

which is purely imaginary. The $\cos\Omega t$ term in eq. (3.6) is thus negligeble. After a lockin measurement of the remaining $\sin\Omega t$ component we are left with the error signal

$$\varepsilon = 2P_0 G_{RF} G_L G_D J_0(\beta) J_1(\beta) \mathrm{Im}\left[\mathrm{S}(\omega)\mathrm{S}^*(\omega+\Omega) - \mathrm{S}^*(\omega)\mathrm{S}(\omega-\Omega) \right] \cos(\Delta\phi), \qquad (3.8)$$

where $\Delta\phi$ describes the phase difference between the measured signal and the reference signal in the lockin, and G_{RF}, G_L and G_D is the gain of the RF circuit after the resonator, the lockin and the detector diode respectively. If the circuit is locked to the center frequency of the resonator $\mathrm{Im}[\mathrm{S}(\omega)] = 0$ and the error signal becomes very small.

This signal is then fed to a PID controller used to track the center frequency of the resonator. The output of the PID is sent to the frequency generator that changes the carrier frequency accordingly. A few things can be noted in equation (3.8). The maximum
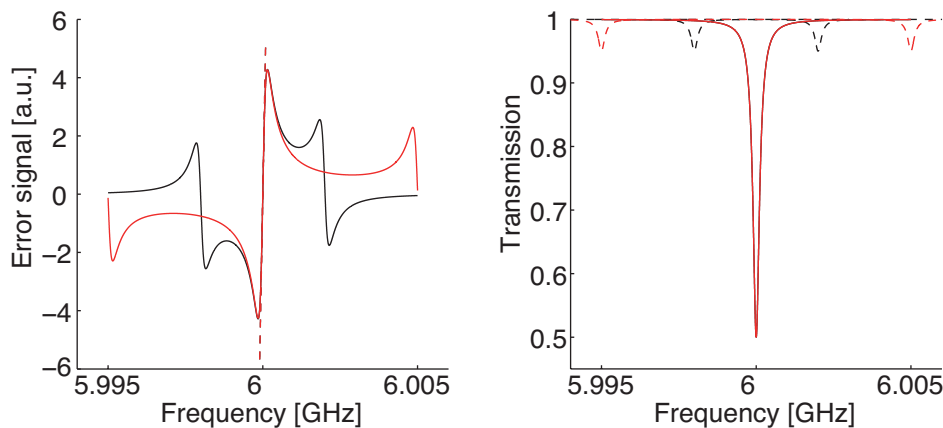
Figure 3.2: Left: Pound loop error signal for two choices of sideband frequencies. Dashed line shows linearized error response. Right: Transmission function of the same resonator. Dashed lines indicate location of the sidebands.

signal is achieved for $\beta = 1.08$, where the product of the two Bessel functions reach its maximum. We would therefore like to operate around this value to reduce the noise of the measurement. The choice of the modulation frequency is not important as long as the sidebands are sufficiently far outside the resonator to be measured, as shown in Fig. 3.2. If the sidebands gets to close to the carrier, they will give a reduced phase shift and gain, and they will start to inject power into the resonator. However, if the sidebands are too far away, variations in the transmitted signal due to reflections in cables etc may influence the response. If the amplitude of the sidebands differ too much, the error signal will be skewed. The same thing is true if the resonance itself is asymmetric. This will result in a non-symmetric error signal as shown in Fig. 3.3. For practical purposes this situation results in a constant offset of the "zero-locking" frequency versus the actual resonance frequency. This can be compensated for by a DC offset in the PID setpoint, but this offset becomes gain dependent, making power sweeps using the PDH method more complicated.

If we linearize eq. (3.8) around the center frequency we end up with the following simple expression for the slope of the error signal

$$\varepsilon_{lin}(\omega) = 4G_{tot}Q_{tot}(1 - S_{21min})\frac{\omega - \omega_0}{\omega_0}, \tag{3.9}$$

where $G_{tot} = 2P_0 G_{RF} G_L G_D J_0(\beta) J_1(\beta) \cos(\Delta\phi)$. This linearization holds even for strongly asymmetric resonators. One important outcome is that the phase response scales with the total gain of the loop. This can be used to perform more accurate phase measurements.

When the carrier signal is off resonance the resulting error signal stems from the phase modulated signal being partially converted into an amplitude modulated signal, as shown conceptually in Fig. 3.4. This PM-to-AM conversion is minimized by the feedback.

3.3 Frequency modulated PDH-loop for Q-factor measurements

In this section the effects of modulation from the previous section is extended and we consider what happens if we were to weakly modulate the error signal. Already from eq. (3.9) we
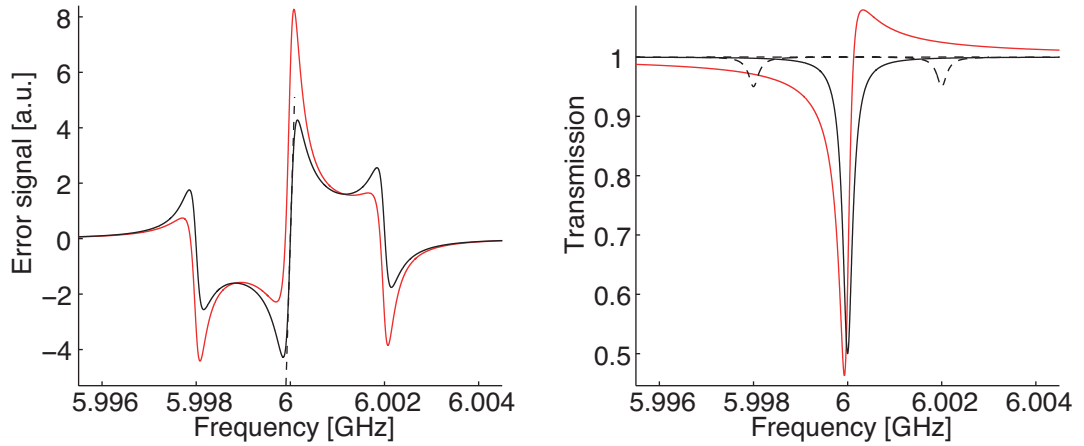
Figure 3.3: Left: Pound loop error signal for a symmetric resonator (black) and asymmetric resonator (red). Dashed line shows linearized error response. Right: Transmission function of the same resonators. Dashed lines indicate location of the sidebands.

see that such a modulation will result in a signal proportional to $\partial\phi/\partial f \propto Q_{\text{tot}}$. Using this approach it should therefore be possible to extract information about the dissipation in the resonator. We call this extended PDH locking "q-PDH locking".

The most simple way to also measure the quality factor of the circuit would be to measure the DC component of the power from the detector. The contribution from the sidebands can be considered very small if the loop is locked on the center frequency of the resonator and the sidebands are outside the resonator, $\Omega/2\pi \gg \Delta f$. The DC component of eq. (3.6) would then be directly related to $S_{21,min}$, which can be traced back to the internal quality factor of the resonator (if the external quality factor is known) using the following relation

$$V_{\text{DC}} = \sqrt{P_0 Z_0} J_0(\beta) S_{21,\text{min}} + C. \tag{3.10}$$

However, this approach suffers from low frequency noise and also from added broadband noise from amplifiers (C). For this reason we instead would like to measure the slope of the error signal. This can be done by introducing one additional modulation to the carrier frequency:

$$E = E_0 e^{i\omega t + \beta i \sin \Omega_1 t + \alpha i \sin \Omega_2 t}. \tag{3.11}$$

Here $\Omega_1 = \Omega$ is the angular PM fequency from before and α and Ω_2 are the modulation depth and the angular frequency of the added modulation respectively. By following the same steps as in the derivation of eq. (3.6) (see Appendix B) the following error signal can be derived:

$$\varepsilon \approx J_0(\alpha)^2 \varepsilon_0 + G[\omega \pm \Omega_1] + F[\omega \pm \Omega_1 \pm \Omega_2]. \tag{3.12}$$

Here ε_0 is the error signal without the additional frequency modulation, equivalent to eq. (3.8), and G and F are other terms grouped according to the frequency components they contain. If the PDH loop is locked to resonance it is easy to see that both the error ε_0 and the additional term G vanishes (see Appendix B). Furthermore, the terms in G will be negligibly small compared to ε_0 if the modulation depth α is small. Since some of the signal power is redistributed into the Ω_2 sidebands the power in the carrier is reduced. The result
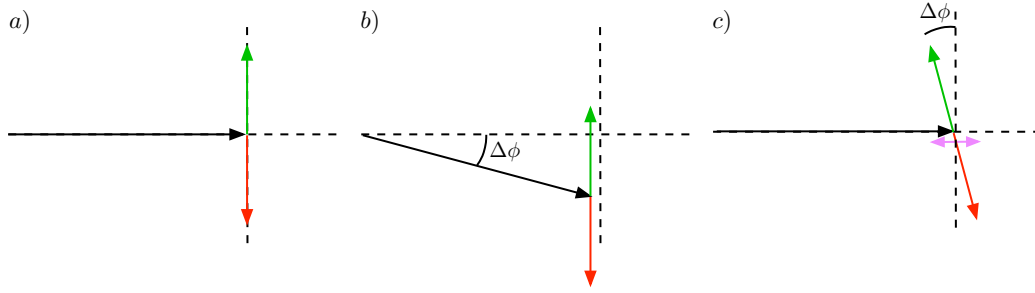
Figure 3.4: Phasor representation of the evolution of the Pound signal, illustrating the PM-to-AM conversion. Black is carrier, green and red corresponds to the first phase modulated sideband. a) The resultant of the phase modulation is exactly the carrier when the resonator is probed at its resonance frequency. b) Slightly off resonance the output signal aquires a phase shift $\Delta\phi$, but not the sidebands. c) In the downconversion we measure the signal in phase with the carrier. Rotated to the carriers reference frame it is easy to see that the resultant of the asymmetric sideband phasors will be projected as an amplitude modulation of the carrier (purple), resulting in partial PM-to-AM conversion.

is that the total gain of the PDH loop is reduced, however, for most practical purposes $J_0(\alpha)$ is close to unity, and the frequency stability of the PDH loop is essentially unaffected, as shown in Fig. 3.5. For example, if we tune α such that the modulation sidebands are 10 dB below the carrier then $J_0(\alpha = 0.1)^2 = 0.995$. The gain and stability of the PDH loop is thus affected with less than 1%. For such weak modulation we can safely neglect higher order contributions.

The only difference for the modulated PDH loop is that the power injected into the resonator is different. From eq. (B.2) it is possible to identify the relative power injected
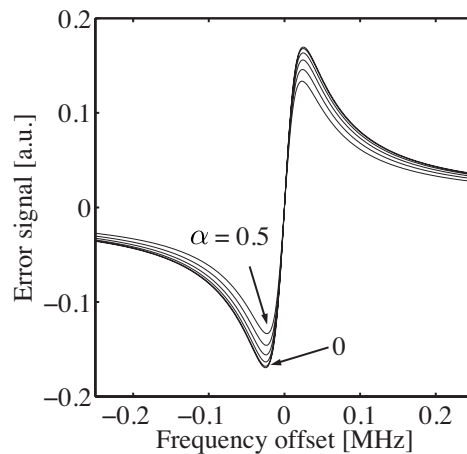
Figure 3.5: The influence of the additional modulation on the main PDH error signal ($\varepsilon + G$, eq. B.6) for $\alpha = 0, 0.1, 0.2, 0.3, 0.4, 0.5$. and $\Omega_2/\Delta f = 0.2$. For small α the additional FM has essentially no effect on the frequency lock stability.
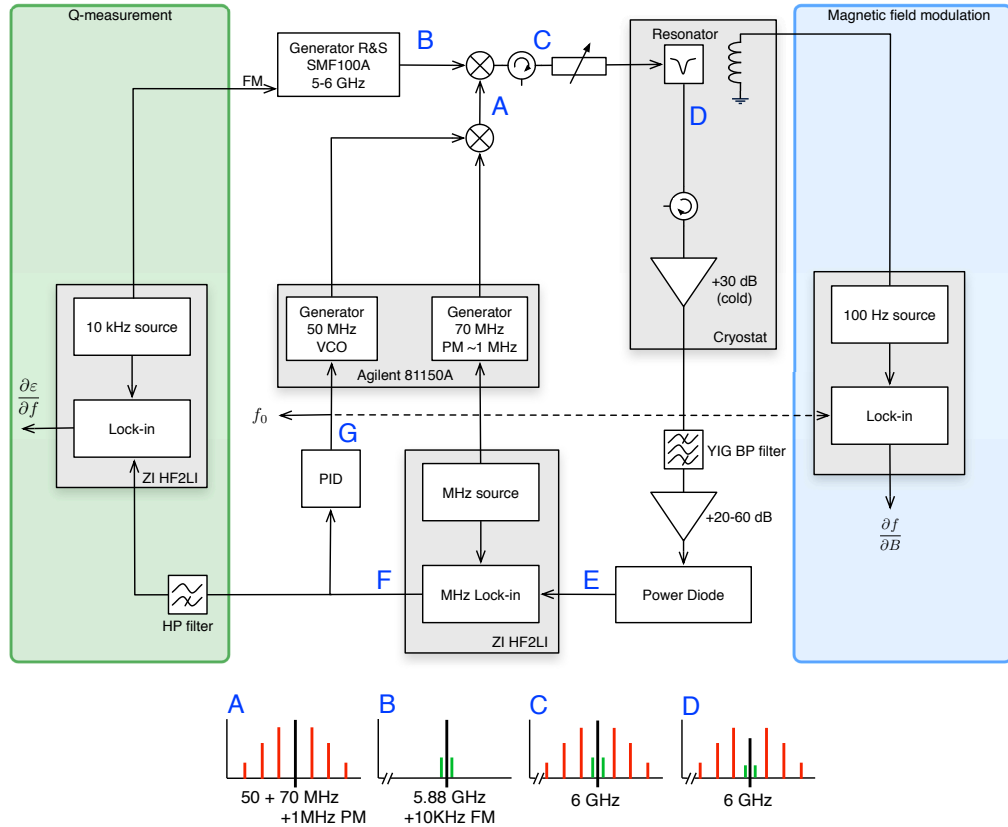
Figure 3.6: Schematic representation of the PDH measurement setup and frequency spectrum at various points in the schematic. Green area shows additional circuit for measuring dissipation and blue area shows additional circuit for measuring $\partial f/\partial B$ and $\partial^2 f/\partial B^2$. Details are discussed in the text.

into the resonator

$$P_{exc}/P_0 = J_0^2(\beta) \sum_{n=-\infty}^{\infty} J_n^2(\alpha)(1 - |S_{21}(\omega_0 + n\Omega_2)|)^2. \tag{3.13}$$

If the modulation depth α is kept small the sum can be truncated around zero. In the limit $\alpha \to 0$ we recover the case without the additional modulation. The remaining term F in eq. (B.6) will consist of a mix of the two modulation frequencies, and we can write it as a main component Ω_1 amplitude modulated by Ω_2. This is the signal that will be detected when measuring the dissipation in the cavity. The exact form of this signal is derived in Appendix B, and it has the form

$$P_{\Omega_1} \approx G_{tot} J_0(\alpha) J_0(\beta) J_1(\alpha) J_1(\beta) Q \frac{\Omega_2}{\omega_0}(1 - S_{21,min}). \tag{3.14}$$

3.4 Experimental setup

The experimental setup that we have used for our PDH measurements is shown in Fig. 3.6, including the schematics for measuring the quality factor. Starting from the point labelled

'A' we use a MHz source to generate a phase modulated signal. This signal is then mixed, using an ADL5391 evaluation board, with another MHz signal that can be tuned by an analog voltage (VCO). The spectrum of these signals should be chosen having the following considerations in mind:

- PM frequency should be larger than the resonance linewidth, but not too large such that it captures a phase dependence of the background spectrum due to cable resonances etc. The detector diode also has a frequency range of optimal responsivity (in our case around 1.5 MHz).

- The PM base and VCO frequencies should chosen such that only one mixing product (sum or difference) can be selected through filtering, typically we use 50 and 70 MHz for this and use the upper mixing product at 120 MHz.

In our case the PM is generated externally using a sinusoidal signal generated in a digital lock-in amplifier. For greater stability and control we use the internal reference of our lock-in rather than an external source. The generated VCO-controlled PM spectrum (A) is then mixed (Marki M8-0326) with a high frequency microwave signal (B) that upconverts the PM spectrum to the resonance frequency (C)(Fig. 3.6 also includes a frequency modulation on the GHz signal, this is used for Q-factor measurements, but for now we ignore this). After proper attenuation and conditioning the signal is then passed to the resonator under study. The signal is then amplified and filtered using a narrow YIG filter to remove broadband noise and other mixing products. Note that the use of a YIG filter will reduce noise but it becomes less convenient when tracking very large frequency changes (such as magnetic field dependence and ESR measurements), as one easily ends up measuring the filter characteristics instead.

The total amount of amplification should eventually be chosen such that the signal is well within the linear regime (here 0 - -20 dBm) of the Power diode (Pasternack PE8016) used in the next step. This detector rectifies the signal and low-pass filter the output such that the GHz signal becomes downconverted to DC, with the PM spectrum intact (point E). The MHz PM spectrum is then demodulated in a lock-in and it results in the error signal eq. (3.8) at point F. A feedback-loop using an analog PID controller (SRS SIM960) then tries to minimize this signal and it gives an output that is directly proportional to the shift in resonance frequency (point F) of the resonator. The proportionality constant is given by the frequency-to-voltage conversion factor of the VCO that tunes the excitation frequency.

To measure the quality factor of the resonator we add the leftmost block in Fig. 3.6. Here we apply an external frequency modulation[1] typically at 11 kHz to the main GHz signal. The FM frequency is chosen such that it is faster than what the PID can track, but slower than the bandwidth of the first PM lock-in stage such that the error signal contains the FM component. Demodulating this FM component from the error signal then gives the signal derived in eq. (3.14). The FM sidebands should also be close enough to the carrier signal such that the phase response of the resonator is linear within this frequency range.

In some cases it can also be advantageous to simultaneously measure and demodulate the response due to an external stimuli. For NSMM applications this can be used to enhance the sensitivity by looking at the response at the tuning-fork oscillation frequency, and for ESR measurements a direct measurement of $\partial f_0/\partial B$ or $\partial^2 f_0/\partial B^2$ can reveal much more information than simply tracking the resonance frequency, especially in a situation of weak

---

[1]The theoretical analysis was done using PM instead of FM. The final result is the same and we could use either method. However, experimentally it is more convenient to use FM in our case.

(a)

(b)

(c)
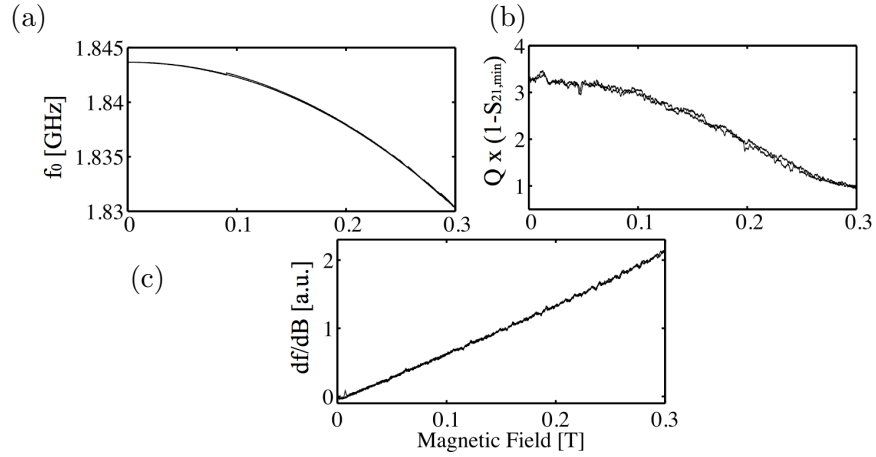
Figure 3.7: Example of a pristine resonator (fractal with fractal ground, NbN on Si) tracked with the PDH technique as a magnetic field is applied parallell to the superconducting film from 0 to 300 mT and then back to 0. a) Resonance frequency. b) Dissipation. c) Analog derivative of frequency due to a small (2 Oe) oscillating applied magnetic field. All traces show small (some reproducible) deviations from a smooth dependence due to non-linear disturbances to the resonator, such as flux avalanches in the superconducting film. Note the absence of hysteresis.

coupling to a spin ensemble. In the rightmost block in Fig. 3.6 this circuit is shown for the case of ESR measurements, but for NSMM applications the shown magnetic field modulation is instead replaced with the cantilever oscillation/excitation. Fig. 3.7 shows an example of a q-PDH measurement with magnetic field modulation on a pristine NbN resonator in an applied magnetic field. f_0, Q and $\partial f \partial B$ is recorded simultaneously.

4
NEAR-FIELD SCANNING MICROWAVE MICROSCOPY

4.1   Introduction to near-field scanning microwave microscopy

Near-field scanning microwave microscopy (NSMM)[1] is a technique that localizes microwave radiation to a small aperture or tip. Around this aperture energy is stored in the evanescent (near-) fields, and the technique is then concerned with measuring small perturbations to the enegy stored in these fields, that may be a result of a change in the local environment due to local variations in the sample that is investigated.

Near-field probing has a relatively long history. The first ideas originated already in 1930's [76]. However, due to the technological difficulties involved the first experimental attempts were made in the late 1950's [77] with apertures in waveguides. But it was not until the development of very precise distance control and nanoimaging, i.e. the invention of the STM [78] and AFM [11] and the following revolution in nanoscience, that the field of near-field probing could reach its full potential. Today, there exist many different types of near-field microscopes, see for example Refs. [33, 79] for a review.

The choice of distance control will influence the possible applications of the microscope. The most common implementation is by using STM [80, 81] to maintain a constant distance to the sample. The advantage is that the tip is brought close to the sample, which will result in a very good spatial resolution for the microwaves. However, one drawback of STM is that it can only be used on conductive substrates. This limited selection of samples is why effort was put in to develope AFM based microscopes [82–86], and this is also the main reason why we choose to work with AFM in this thesis. Here we can image any material and we can achieve precise distance control at greater separations from the sample, making the combined AFM/NSMM technique non-invasive.

While one promising application of NSMM has been to reach beyond scanning capacitance microscopes in sensitivity and functionality for CMOS and semiconductor optimization [79, 84, 86, 87], NSMM have successfully been applied to a wide range of samples. Recent studies include graphene flakes and how they interconnect with other flakes [88], phase transitions in high-Tc superconductors [89] and their material properties [90–92], ferroelectric [93] and magnetic [94] domain imaging, photovoltaics [32] and to map out Hall resistivity in semiconductors [95]. They have also found use as characterization tools for organic semiconductor circuits [96–98], biological samples such as DNA [99] and cell membranes [100]. Some efforts have also been made towards developing microwave current

---

[1]Several names for the same technique exist in literature: SNMM, NFMM, SMM (Agilent), EMM ("evanescent microwave microscopy") and MIM ("microwave impedance microscopy").

probes (as opposed to electric field probes) and scanning electron spin resonance (ESR) measurements have been demonstrated [101, 102].

While NSMM being the common name for this type of microscope, the underlying technology can be very different. In the context of this thesis we may group the types of instruments into two different categories.

(i) Non-resonant NSMM. This meathod measures the reflection coefficient of a transmission line terminated by the tip [82, 83]. It has the advantage of being a very broadband technique, the response can typically be measured from a few up to several tens of GHz simultaneously.

(ii) Resonant NSMM. This technique involves different types of microwave resonators, such as striplines [32, 84] or dielectric resonators [85, 98]. In this type of microscope a microwave photon will be stored a long time ($\tau \sim 2Q/\omega$) at the tip. For quantum coherent measurements we would like to have a photon lifetime longer than the interaction time (coupling) to the quantum object we are studying. Resonant NSMM has shown to be the most useful technique for quantitative analysis [103] due to its enhanced sensitivity, however, the bandwidth becomes inversely proportional to the Q-factor (and sensitivity). For the "coherent" NSMM considered in this thesis we must resort to a resonant NSMM since this significantly increases the interaction time of a single photon with the quantum device we want to investigate.

In this work we chose superconducting resonators for their potentially high quality factors (resulting in a higher microscope sensitivity and longer photon life time). We must also operate the microscope at low temperatures, such that the thermal energy is smaller than the photon energy $\hbar\omega \gtrsim k_B T$. At the time of writing this thesis several cryogenic NSMMs have been demonstrated [86, 93, 104], however, they all operate in a classical regime with a high number of photons in the resonator (or without resonant probes).

The main technological achievement demonstrated in this thesis shows that NSMM can be employed down to very low probing powers, such that it can be used for coherent interaction with quantum systems in the sample. This chapter describes the principles and technology behind our NSMM in the classical regime, and the next chapter specifically considers the interesting regime of "coherent" NSMM and its possible future applications among other SPM techniques in materials science [10]. In [Paper II] we demonstrate that in this regime it is possible to reach a sensitivity (and resolution) that is comparable to other NSMMs, and we also show that even in this low power regime our microwave readout is fast enough such that we can run the microscope without AFM height control, and instead follow a surface of constant capacitance, as sensed by the microwave resonator.

4.2 Theoretical overview

In our case we use a superconducting fractal microwave resonator as our near-field probe, and the resonator can be thought of as an antenna. To suppress far-field radiation and maintain a high Q it is shielded by ground planes. The open end of the resonator, where the microwave electric field is at maximum, it is terminated by an unshielded, sharp tip. This tip will work as a sub-wavelength antenna, which can radiate energy. In the near-field of this antenna reactive energy is stored in evanescent fields which are non-propagating in space, localized around the tip, and strongly dependent on geometry. Another way to understand this is by considering a dispersionless waveguide. It has a very low cut-off frequency, and the propagating mode always has a higher frequency $f > f_c$ than the cut-off.

However, the open end of the resonator introduces dispersion and the cut-off frequency for propagating waves becomes very large. In this case the propagation constant (eq. (2.2)), which also can be written $\gamma = \alpha = jk\sqrt{1 - (f_c/f)^2}$, becomes real. Thus the propagating wave $Ae^{\gamma z + i\omega t} = e^{-\alpha z}e^{-i\omega t}$ becomes evanescent, with an exponential decay, at the end of the waveguide.

By placing some object nearby the tip we can perturb these evanescent fields, changing the properties of the reflected wave from the tip (and the properties of the resonator). Thus, the closer we place our perturbing object, the stronger the perturbation will be, and the dominant contribution will always come from the region near the apex of the tip. By having a very sharp tip it is therefore possible to overcome the Abbe resolution limit $d = \lambda/2n\sin\theta$ for microwave radiation by many orders of magnitude by using a near-field probe. For example, in the work presented here we achieve a resolution $d < 10^{-5}\lambda$.

From Maxwell's equations it is possible to obtain the frequency shift of a cavity due to a perturbation [24]

$$\frac{\omega - \omega_0}{\omega} = -\frac{\int_V [\Delta\varepsilon E \cdot \tilde{E} - \Delta\mu H \cdot \tilde{H}]dV}{\int_V [\varepsilon_0 E \cdot E + \mu_0 H \cdot H]dV}, \tag{4.1}$$

where $|H| = \sqrt{\varepsilon/\mu}|E|$ and E and $\tilde{E}$ are the unperturbed and perturbed fields respectively. A similar expression can be obtained for the change in Q-factor of the cavity. While exact, these expressions are not very practical, especially not in the case of tip-based NSMM, since exact knowledge of the tip and sample geometry is required.

Here we will instead consider the NSMM response to a perturbation in the classical regime in terms of a simplified circuit model. The picture is as given in Fig. 4.1. A quarter wave resonator is inductively coupled to a transmission line and we introduce the sample modelled as an arbirtary RLC-circuit capacitively coupled to the electric tip. This results in a reflection coefficient Γ at the tip, which is close to the unperturbed case $\Gamma = 1$ due to a small perturbation in the sample. The following derivation of the NSMM response initially follows that given in Ref. [25], but we now also consider the additional reflection coefficient Γ. The propagation of a microwave signal in a transmission line can be described by

$$I_0(x) = I_0 e^{\gamma x}. \tag{4.2}$$

For a resonator in a 3-port network with two external ports as depicted in Fig. 4.1, we consider the microwave field inside the resonator. The feedline acts as a virtual current source (voltage source if capacitively coupled) and the signal entering the resonator at the coupler ($x = 0$) is $-I_0 S_{13} e^{i\omega t}$. This signal then travels the length of the resonator, represented by multiplying the initial signal with $e^{-\gamma l}$, where l is the length of the resonator. At the end of the resonator terminated by the tip the signal can go two ways. It can escape into the sample with amplitude $1 - \Gamma$, or it can be reflected back with amplitude Γ. The signal that travels again through the resonator reaches the coupling element, and also here it can either be reflected again, or escape into the feedline. The signal that ultimately leaks back into the feedline can thus be expressed as

$$I = -I_0 S_{13} \left[\sum_{n=0}^{\infty} (S_{33}\Gamma e^{-2\gamma l})^n\right](-S_{31}\Gamma e^{-2\gamma l}) = \frac{I_0 S_{13} S_{31} \Gamma e^{-2\gamma l}}{1 - S_{33}\Gamma e^{-2\gamma l}}. \tag{4.3}$$

Due to symmetry we have that $S_{13} = S_{31}^* = i\sqrt{\pi/2Q_c}$, and $S_{33} = \sqrt{1 - \pi/Q_c}$. Using $S_{21} = (I_0 - I)/I_0$ and a first order expansion of the propagating wave [15]

$$e^{-2\gamma l} \approx 1 + \frac{\pi}{2Q_i} + i\pi\frac{\omega - \omega_{1/4}}{\omega_{1/4}}, \tag{4.4}$$
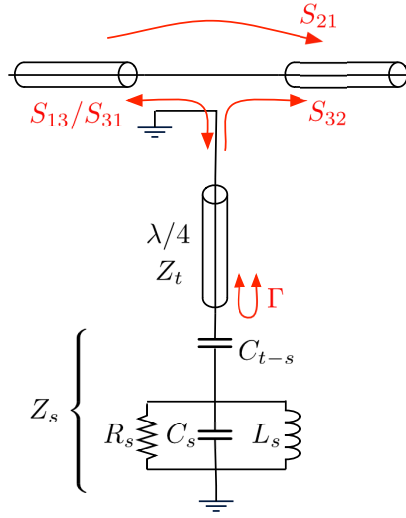
Figure 4.1: Circuit considered when deriving the response of the NSMM probe with respect to the tip-sample impedance Z_s.

we arrive at the standard form of S_{21}

$$S_{21} \simeq \frac{1 + \frac{Q}{Q_c}|\Gamma|e^{i\arg\Gamma} + i2Qdx}{1 + i2Qdx},$$ (4.5)

where

$$Q \simeq \frac{1}{1/Q_i + 1/Q_c + 1/Q_s},$$ (4.6)

$$dx \simeq \frac{\omega - \omega_{1/4}}{\omega_{1/4}} - \frac{2x_s}{\pi}.$$ (4.7)

Q_s and x_s are obtained by taking the real and imaginary parts of the reflection coefficient. If we assume that the load has a much higher impedance than the resonator, $Z_s \gg Z_t$ then $\Gamma \approx 1$, i.e. almost perfect reflection, and we can write

$$\Gamma = \frac{Z_s - Z_t}{Z_s + Z_t} = \frac{1 - Z_t/Z_s}{Z_t/Z_s + 1} \approx 1 - 2\frac{Z_t}{Z_s} = 1 - \frac{\pi}{2Q_s} - 2ix_s,$$ (4.8)

The sample quality factor is defined as $Q_s = \pi/4r_s$, $r_s = \mathrm{Re}(Z_t/Z_s)$ and $x_s = \mathrm{Im}(Z_t/Z_s)$. For a general load on the resonator as depicted in Fig. 4.1 we can write the total impedance as

$$Z_s = \frac{1}{i\omega C_{t-s}} + \frac{1}{1/R_s + \frac{1}{i\omega L_s} + i\omega C_s}.$$ (4.9)

Using this approach it is possible to obtain information about the impedance of the sample by monitoring the frequency and Q-factor of the resonant probe. While this describes the response of a "classical" resonant NSMM probe we consider in the next chapter other effects in the quantum limit that can have much more pronounced effects on the NSMM probe response on top of the response derived here.

In the previous section we see that the response of the NSMM probe to first order is linear in Z_s, it is also clear that in most situations C_{t-s} will be the parameter that dominates in eq. (4.9). This means that variations in C_{t-s} due to variations in sample topography will answer for a significant contribution to the probe response, masking more interesting effects from the sample. This is a big issue for qualitative analysis, where both tip shape and distance masks the response, and topographic cross talk becomes inevitable.

4.3   Tuning-fork AFM

The Atomic Force Microscope (AFM) was invented in 1986 by Binning *et al.* [11]. It measures the force acting on a nanometer sized tip apex as it is scanned in close proximity over a sample surface. The force detected includes both short-range repulsive atomic forces, attractive van der Waals forces and, long range electromagnetic forces exterted on the tip. The response is typically read out as the deflection of an oscillating cantilever, by letting a laser beam reflect off its surface. The oscillating photoresponse is then converted to a current in a photodiode and detected using conventional electronics. However, this type of setup obviously takes up a large amount of space, and in a cryogenic environment a laser can be a source of local heating. The use of a piezoelectric quartz tuning-fork for scanning probe applications was pioneered by Karrai in 1995 [105], where he used it for distance control in a SNOM. A few years later atomic resolution tuning-fork AFM was demonstrated by Giessibl [106]. The tuning-fork is a compact solution and readout is purely electronic, making it very suitable for cryogenic microscopes. Another advantage is its high spring constant $k \sim 1000$ N/m, making it suitable for non-contact AFM (nc-AFM), thus combining nc-AFM with microwaves (NSMM) allows for truly non-invasive measurements.

The principle of operation is the following; when a vibrating beam is subject to an additional force, the resonant conditions for the beam will change, altering its phase, amplitude and dissipation, depending on the nature of the force. The tuning-fork resonance is monitored by detecting its output current as it is excited by a voltage at its resonance frequency. The piezoelectricity of the tuning-fork converts the applied ac-voltage to a mechanical oscillation.

For an (unbalanced) tuning-fork the amplitude of oscillation can be estimated using the following formula [107]

$$A(\omega_0) = \frac{1}{\alpha\omega_0}\left[i_{\text{tot,rms}}(\omega_0) - \frac{V_{\text{in,rms}}(\omega_0)}{2R_{\text{tf}}}\right], \tag{4.10}$$

where $\alpha \approx 5$ μC/m is the piezoelectric coupling constant, and R_{tf} is the effective resistance of the tuning-fork. This quantity can be obtained by fitting the measured line shape of the resonance to that of a series RLC-circuit and the quality factor relates to the resistance as $Q = \omega_0 L_{\text{tf}}/R_{\text{tf}}$. It has been shown that the optimal resolution in tuning-fork AFM is obtained with an amplitude of 0.3-1 nm [108]. For the type of tuning-forks we use here the amplitude of oscillation relates to the excitation voltage roughly as $A \approx 1$ Å/mV. In constant excitation mode the AFM feedback tries to keep the time-averaged frequency shift Δf of the tuning-fork constant by controlling the tip-sample separation. The time-averaged frequency shift relates to the instantaneous force $F(z,t)$ acting on the tip as [109]

$$\Delta f(x,y,z_0) = \frac{f_0^2}{kA^2}\int_0^{1/f_0} F(x,y,z_0+z(t))z(t)dt, \tag{4.11}$$
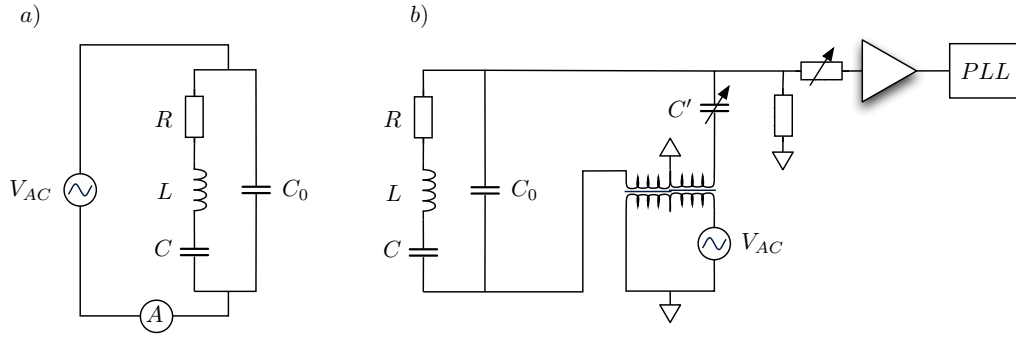
Figure 4.2: a) Simple electrical model for the piezoelectric tuning-fork. A driving voltage is applied and the resulting current is measured. b) The tuning-fork coupled to a circuit which compensates for the stray capacitance C_0 by adding a signal phase shifted 180 degrees with the same capacitance $C' = C_0$. The phase response near resonance is then detected in a phase locked loop (PLL).

where $z(t) = A \cos(2\pi f_0 t)$ and z_0 is the time-averaged tip height.

The quartz tuning-forks used for scanning applications typically have a frequency around 32.7 kHz, and a perfectly balanced tuning-fork can have a quality factor in excess of 10^5. However, if the symmetry of the two prongs is broken, for example by attaching a tip to one of the prongs, the quality factor can drop several orders of magnitude, depending on the mass of the attached object [110]. In general, a tuning-fork can be modeled as a series RLC-circuit, as shown in Fig. 4.2a, shunted by a stray capacitance C_0. This capacitance mainly constitutes extra capacitance due to wiring but can also be intrinsic to the tuning-fork, especially if the prongs are loaded asymmetrically. This capacitance skews the resonance lineshape and the phase response of the tuning-fork. To avoid this we use the circuit described in Fig. 4.2b. The purpose of the transformer and the variable capacitance is to create an identical signal as the one used to excite the tuning-fork, but shifted 180 degrees in phase. If the capacitance is tuned such that $C' = C_0$ the stray contribution will destructively interfere at the input of the amplifier (FEMTO LCA-200K-20M). A phase locked loop (PLL) can then be used to measure the response of the tuning-fork itself.

Phase-Locked-Loop (PLL)

For a tuning-fork having a high quality factor its response time ($\tau = 2Q/\omega$) can be very large (several seconds). It thus becomes impractical to measure the amplitude of oscillations near resonance. By instead monitoring the phase response it is possible to detect shifts on a timescale of just a few cycles. For this purpose we use a phase locked loop (PLL) that always tries to minimize the phase difference between a reference and the measured signal. Similar to a homodyne measurement, it relies on the mixing of a reference signal with the measured signal

$$\sin(\omega_0 t + \phi_{\text{ref}}) \cos(\omega_0 t + \phi) \approx \frac{\phi_{\text{ref}} - \phi}{2}, \tag{4.12}$$

where higher order terms have been neglected (filtered out). If the resonance frequency of the tuning-fork suddenly changes it will result in a phase shift of the probe signal $\cos(\omega_0 t + \phi)$. A feedback loop then tries to minimize this phase difference by adjusting the frequency of
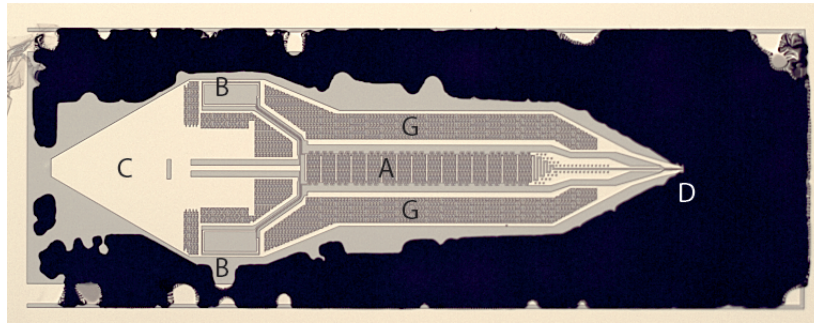
Figure 4.3: Optical image of a scanning probe as fabricated in its silicon frame. A: fractal resonator. B: Coupling loops. C: Ground bonding pad for connecting ground/DC bias. D: Tip. G: Microwave ground and screening electrodes.

the excitation, ω_0. Typically this is done using a voltage controlled oscillator (VCO).

4.4 NSMM design

In this section the most important aspects of the design of our cryogenic AFM/ NSMM will be discussed. Starting from probe design and fabrication we continue with a general description of the cryostat. The details of the scanner unit itself are then outlined and finally the general principles behind the operation of the NSMM and the obtained results are presented.

4.4.1 Scanning probe design

The fabrication of the scanning probes are covered in the next section and their general microwave properties in Chapter 2. The specific design variation used for NSMM probes is shown in Fig. 4.3 and here we will briefly look at the specific resonator design used for scanning probes and highlight the most important characteristics.

- The size should be kept at minimum to reduce the mass and maintain a high mechanical quality factor of the AFM tuning-fork.

- The coupling loop have to be placed sufficiently far from the tip. In our design the external transmission line to which the resonator is coupled determines this distance which is around 1 mm.

- The resonator itself thus has to be around 1 mm long and still have a frequency of around 6 GHz (compatible with our microwave equipment).

- The coupling loop have to be large enough to ensure sufficient coupling at distances of 10-50 μm from the external feeding-line.

- The structure has to be symmetric with respect to the DC bias pad since otherwise microwave currents will be induced in the connected wire, resulting in a lower quality factor. To maintain symmetry in the design the coupling loop is balanced with an identical dummy loop on the opposite side of the probe.
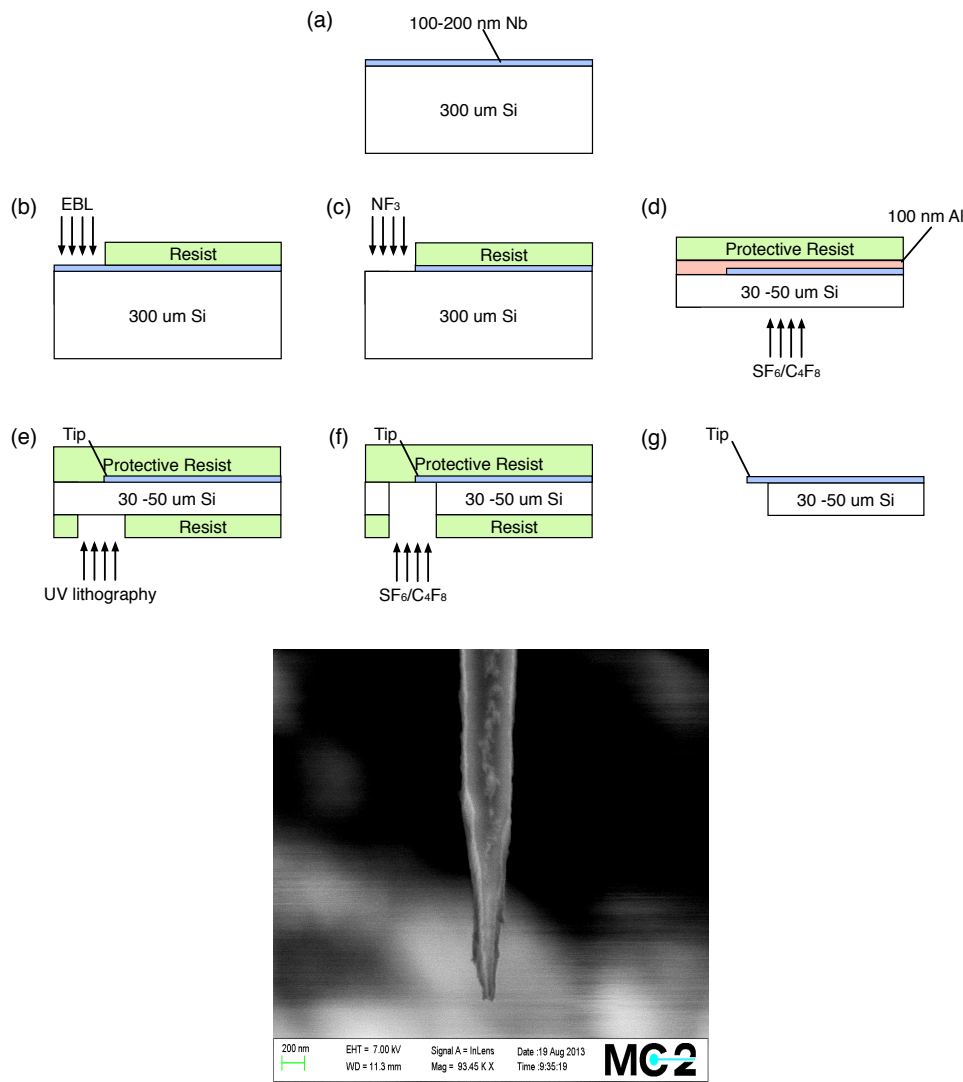
Figure 4.4: Top: Fabrication steps for making the NSMM probes. Bottom: As fabricated SEM image of a typical Nb tip.

4.4.2 NSMM probe fabrication

NSMM probes on both silicon and sapphire were fabricated, however, ultimately the use of silicon as the substrate material was chosen since it can easily be isotropically etched to yield a sharp tip. Initially the motivation for using sapphire was its lower loss tangent. For this purpose ultrathin sapphire (50 μm) was used, and individual scanning probes were cut out by mechanical dicing. While this technique gave good resonators, tip fabrication became an issue. To create a sharp tip Focused Ion Beam (FIB) milling was used. While this eventually gave sharp tips, it also resulted in a strong decrease of the resonator quality factor, sometimes down to just a few thousands. Due to the hardness of sapphire FIB milling also takes a long time, and during this time remaining parts of the sapphire substrate near the tip becomes heavily doped with Gallium ions. Since the milled region is at the resonators electric field maximum, these implanted ions becomes a source of dissipation. Silicon, while having a

lower loss tangent than sapphire, still has the advantage of being easily micromachined.

The detailed Si-probe fabrication technique is outlined in Appendix A. The general procedure outlined in Fig. 4.4 is as follows. The sputtered Nb film is patterned using electron beam lithography. The niobium is then etched in a reactive plasma of either CF_4/O_2 or NF_3[2]. The wafer is cleaned and then a layer of Aluminium is evaporated and on top a resist layer is spin coated, both as protection when later thinning down the substrate. The wafer is then diced and the remaining processing is done on one chip at a time. The chips are thinned town using a Bosh process (reactive isotropic plasma etching) to 50-30 μm. A resist mask is then made on the backside by using infrared alignment[3], and the outline of the NSMM probe is defined. Another etching step is the used to remove the remaining Si and to cut out the NSMM probes. Etching throught the last few μm is monitored carefully in order to stop the etching at the right moment such that suspended Nb is produced at the tip. When producing Josephson devices on the probe additional steps inbetween (e) and (g) in Fig. 4.4 are inserted, see Chapter 6.

4.4.3   Cryostat design

The cryostat used for the NSMM was initially intended for use at liquid Helium temperature (4 K). To accomodate the NSMM setup we have made several modifications and also installed a single-shot ^{3}He cooling unit. A sketch of the cryostat is shown in Fig. 4.5. One major modification is the inclusion of an intermediate thermalization stage to reduce the heat load from all the required wiring on the helium bath and the ^{3}He-stage. For DC measurements it is common to use resistive wires to reduce heat conduction (Wiedemann-Franz law: $\kappa/\sigma = LT$). As long as they do not carry any substantial currents this is not a problem, and it can reduce the heat load on the cold stage significantly. When it comes to constructing a cryogenic piezo tube scanner, this approach is not possible. In order to be able to operate the scanner properly the piezoelectric material needs to be charged (i.e. we need a current), and this should be done within a timescale set by the feedback control of the microscope (kHz) such that it has time to compensate for mechanical vibrations etc. Furthermore, the interial sliders we use for coarse positioning needs to develope a large enough inertial moment, which will also be limited by the RC-constant of the wiring and the capacitance of the piezoelements. Low ohmic wiring is therefore a necessity, and thermal conductivity becomes an issue. This has had a significant impact on the boil-off rate of helium in the used cryostat. To make the best of this situation we have therefore implemented an additional thermalisation stage for the ingoing cables. This thermalization is anchored to the tubes from which cold helium gas leaves the cryostat, at an estimated temperature of 30-40 K. To suppress the influence of mechanical vibrations the cryostat is suspended using pressurised air, however there is no internal suspension or acoustic isolation, making the setup sensitive to for example boiling nitrogen.

---

[2]While the reactive etching of these two processes involves flouride, thus resulting in similar etching conditions, the former gas results in a polymer film originating from the resist mask, containing also Nb residuals. This film is very hard to remove later on and it results in increased losses in the resonator if present. For this reason the NF_3 process is preffered. On the other hand the added oxygen in the CF_4 process can be used to control the etch rate of the mask, thus producing Nb-sidewalls with a desired angle.

[3]Silicon is partly transparent to IR light, while any metallic thin film will effectively block IR, thus providing contrast. For a 30 μm thick sample alignment accuracy can be as good as 1 μm using this technique, but this quickly degrades for thicker substrates.
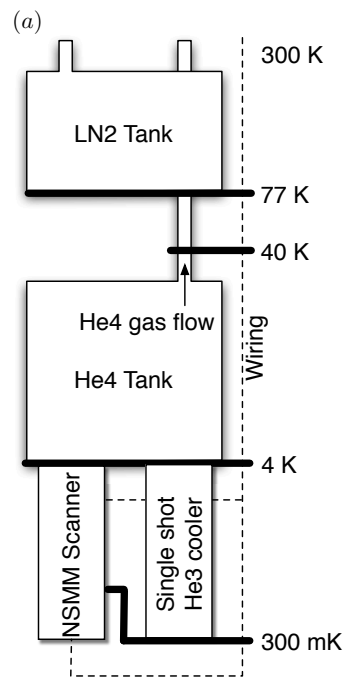
Figure 4.5: a) Sketch of the NSMM cryostat.

4.4.4 Scanner design

The AFM/NSMM scanner unit is shown in Fig. 4.6, and in this section we consider some important aspects of its design.

First of all, it must be mechanically stable, and the mass should be kept small not to overload the piezo elements. All piezo tubes have some characteristic resonance frequencies, typically $10^3 - 10^5$ Hz in a pristine state. When loaded with a mass this frequency will be reduced. If it becomes too low it may start to interfere with low frequency mechanical vibrations and the AFM distance control feedback loop. Futhermore, the response time of the piezo column becomes slower. In a cryogenic environment one also has to consider thermal conductivity and thermal expansion of the mechanical anchoring. To achieve good mechanical stability the tube should be tightly anchored on both sides, but thermal expansion in the wrong direction may cause the brittle piezo tube to crack. On the contrary, thermal expansion could also compromise the anchoring strength and stability. In our design we have glued a ring of macor ($\alpha \sim 9.2$ μm/m K), outside the piezotube ($\alpha \sim 8$ μm/m K) making use of their very similar thermal expansion coefficients. The macor provides a solid base for the tubes, and will not crack under the pressure of the base aluminium plate ($\alpha \sim 22$ μm/m K) at which it is attached. Using this approach the piezo tubes are reinforced by the contracting aluminium base plate to which they are mounted.

Our xy-scanner consists of four tubes in total and an inertial piezo slider (Attocube ANZ100) for z-coarse approach (see Fig. 4.6) mounted on top of the xy-scanner. Finally we have the z-scanner tube just below the sample platform to ensure fast feedback of the z-motion. The second part of the scanner holding the tuning-fork and microwave circuitry is mounted on two other inertial sliders used for coarse xy-motion. Since all piezo drive requires low ohmic wiring we anchor these to 4 K only. The sample and tuning-fork is then
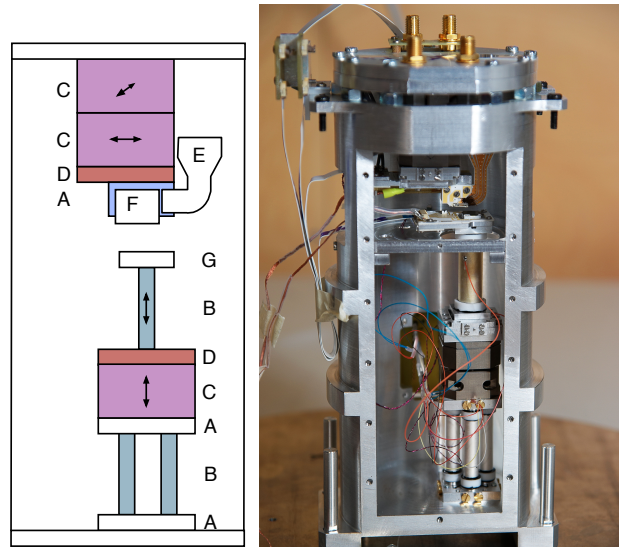
Figure 4.6: Sketch of the NSMM scanner parts and photo of the scanner mainframe. A: Supporting metallic plate. B: Piezo tube. C: Inertial piezo slider for rough positioning and coarse approach. D: Thermal isolation. E: Microwave launcher. F. Ceramic plate holding tuning-fork and microwave feedline. G: Sample platform.
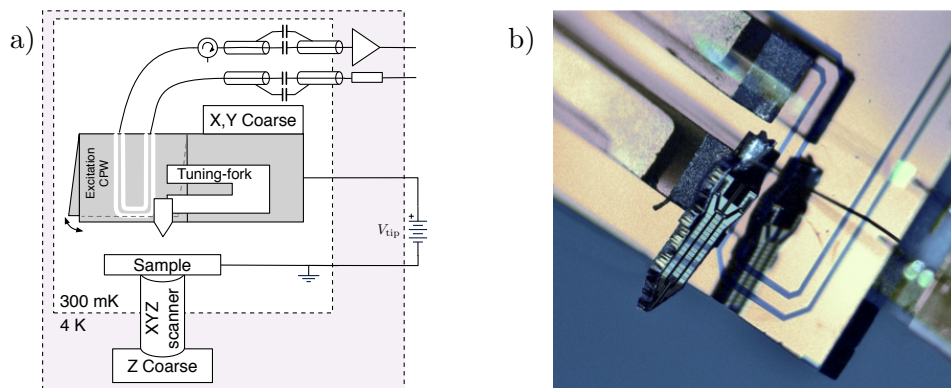
Figure 4.7: a) Sketch of the NSMM assembly. b) Optical image of the assembly.

thermally isolated from 4 K and thermally connected to 300 mK.

A more detailed sketch and image of the assembly containing the AFM tuning-fork and the mounted NSMM probe is shown in Fig. 4.7. The tuning-fork is removed from its original casing and glued to a ceramic plate. The NSMM resonator is then glued to one prong of the tuning-fork and the whole assembly is placed on top of a microwave transmission line. The distance between this transmission line and the coupling loop on the resonator can be easily tuned using a differential screw, to ensure a proper coupling.

4.4.5 NSMM operation

Apart from the PDH setup described in Chapter 3 the cryogenic microwave setup is shown in Fig. 4.8a. The input signal is attenuated at the various temperature stages to reduce
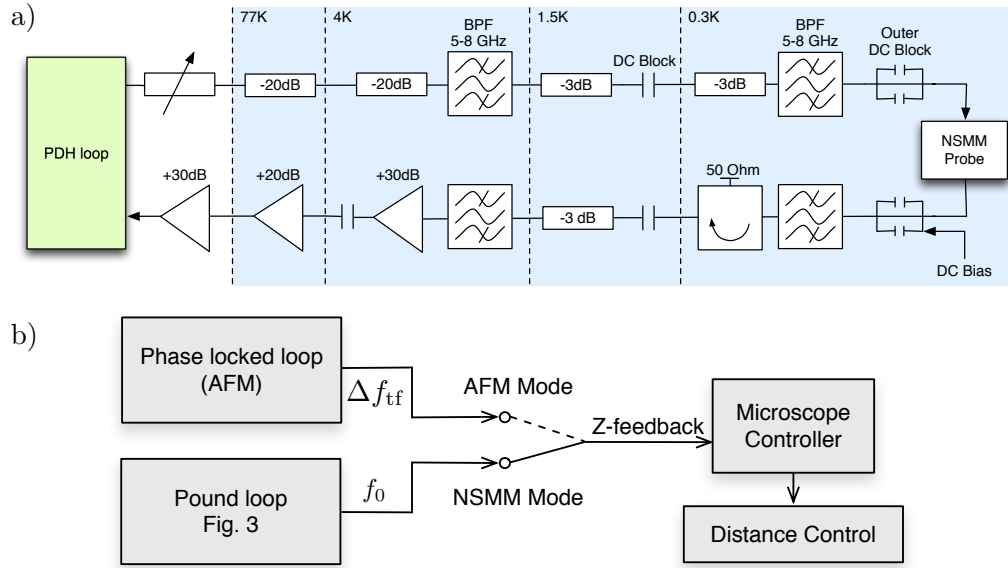
Figure 4.8: a) Cryogenic microwave setup. b) The two different scanning modes discussed in the text.

noise and incoming thermal radiation. At the 300 mK stage the ground is separated by outer DC blocks from the rest of the cryostat ground, and instead connected to a separate potential (Fig. 4.7a). Thus, the DC potential of the NSMM probe can be shifted with respect to the sample potential. The PDH loop produces a signal that is proportional to the frequency shift of the cavity and it can be used as the feedback signal for scanning. We call this "NSMM mode" in contrast to AFM mode where the distance control is based upon the response of the AFM force sensor. However, in AFM mode we can still monitor the frequency of the microwave resonator (see Fig. 4.8b).

4.5 Results: calibration, sensitivity and resolution

4.5.1 Stray fields

We shall now consider what happens when we approach our NSMM probe towards a metallic surface. By looking at the frequency shift as a function of distance to the surface we can learn about the stray capacitance of the probe as well as the geometry of the tip apex. The frequency shift when approaching a metallic surface is shown in Fig. 4.9a for large distances and near contact (inset). The fitted curve is the calculated frequency shift

$$\Delta f = \frac{1}{2\pi}(\omega_0 - \omega) = \frac{1}{2\pi\sqrt{LC}} - \frac{1}{2\pi\sqrt{L(C + \Delta C)}}, \tag{4.13}$$

where ΔC is evaluated from eq. (D.3). For small distances (inset) the frequency shift agrees well with the observed tip radius (Fig. 4.9b) which is ∼200 nm. However, to accurately fit the data for longer distances a tip radius of 3.4 μm gives the best fit. It should be pointed out that this is an effective estimation of the dipole field of the whole unshielded tip, and a large contribution comes from stray capacitances from parts of the tip other
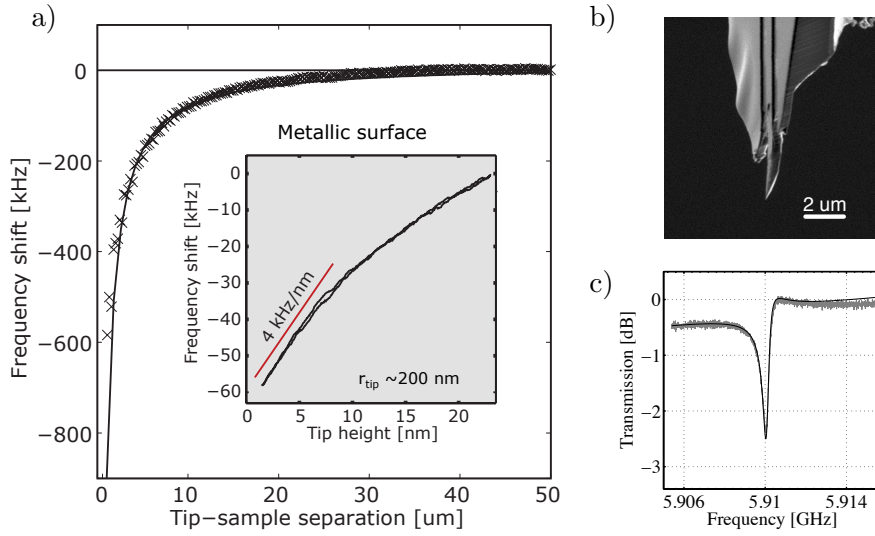
Figure 4.9: a) Frequency shift of the microwave resonator as the tip is approached a metallic surface. The solid line is a fit to the data using eq. (4.13) and the parameters $r_{\text{tip}} = 3.5$ μm. Inset: Same frequency shift in close proximity of the sample surface (approach and retract). b) Scanning electron micrograph of the tip used in the experiment. c) Microwave trasmission (S_{21}) of the same probe. Fit to eq. (2.12) gives $Q = 14600$.

than its spherical apex. The used model is not an accurate description of the large scale fields of the tip geometry shown in Fig. 4.9b, but it gives an estimation of the scale of field localization. At close distances the stray fields play a minor role, and the main contribution to the capacitance comes from the apex of the tip. Indeed, the approach curve in the inset of Fig. 4.9a agrees well with the expected response from a spherical tip of $r \approx 200$ nm.

4.5.2 Performance benchmark measurements

In this section we focus on two different samples that were used in order to determine the microscope's sensitivity to capacitance at low powers. The measurements were carried out at 300 mK with the probe described in Fig. 4.9c, with $Q \approx 15000$. The first sample consisted of a superconducting surface with artificially made topographic structures of the same material. Representative scans are shown in Fig. 4.10 and Fig. 4.12. By measuring the stability of the microscope over an infinite conducting surface we can gain information about how mechanical noise contributes to the microwave readout, which accounts for a major part of the measured noise. This is discussed in more detail in the next section. Furthermore, by comparing the topographic images obtained in AFM mode and in NSMM mode we can get an estimate of the localization of the microwave near-fields around the tip. As can be seen in Fig. 4.10b the obtained NSMM topography is more smeared out as compared to the AFM topography. For this measurement the tip height setpoint is calibrated by moving to a flat part of the sample, and the NSMM frequency shift setpoint is chosen to be the frequency that is measured in AFM mode, in order to maintain the same tip-sample separation in the two cases. This is important since a different NSMM setpoint will result in a different tip-sample separation and thus a different scaling of the NSMM topography. Now the measured height (and the profile) of the artificial protrusion will give an estimate of the localization of the near-fields around the tip. In agreement with
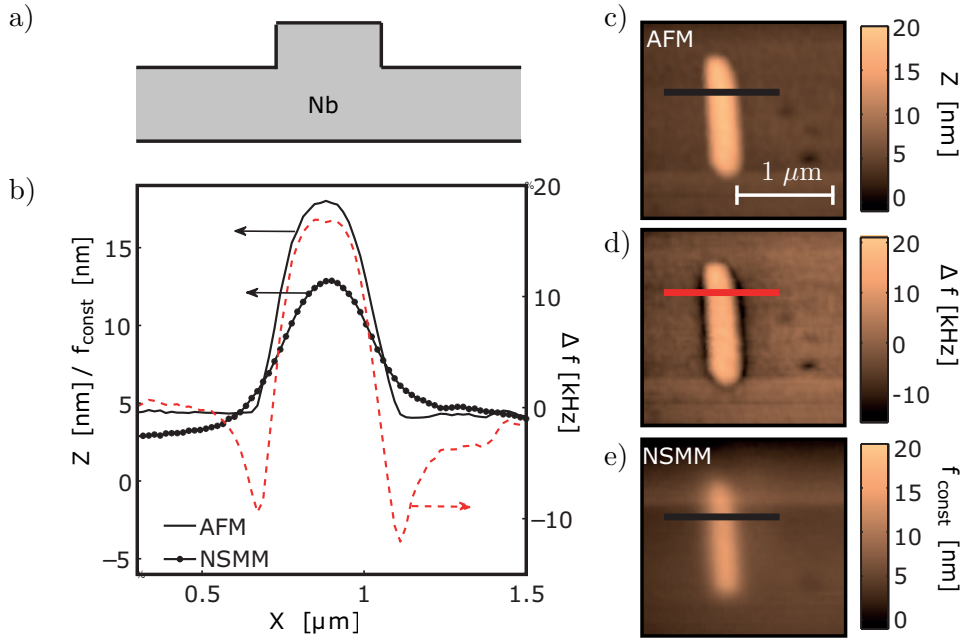
Figure 4.10: Scans over a superconducting (Nb) surface with artificial topography as illustrated in a). b) comparison of line-cuts from scans c-e. c) AFM topography. b) Simultaneously acquired resonator frequency shift. d) topography resulting from a surface of constant capacitance in pure NSMM mode.

the inset of Fig. 4.9a we find that for the same probe the measured shift of 4 kHz/nm can be used to reproduce the NSMM scan from the AFM topography and the simultaneously acquired microwave frequency shift, see Fig. 4.11. In this figure the AFM trace and the frequency shift (from Fig. 4.10b) is combined with the scaling factor $\beta = -4\text{kHz/nm}$ to exactly reproduce the NSMM trace (i.e. $Z_{\text{NSMM}} = Z_{\text{AFM}} + \beta^{-1} \times \Delta f_{\text{AFM}}^{\text{PDH}}$), indicating that the near-field probe at the choosen setpoint can be very well described by the same geometry as the AFM probe.

Fig. 4.12 shows the same scanned area as in Fig. 4.10 for two low microwave excitation powers of the probe measured in NSMM mode. This shows the stability and accuracy of the PDH technique. The scan speed is 2 μm/s, same as what is typically used for AFM. The frequency shifts that are compensated for by the PDH feedback amounts to roughly 3% of the resonance linewidth and we are still able to acquire the image when the resonator is only populated with 1000 photons. However, going to even lower powers makes the feedback highly unstable, mainly due to the high noise temperature ($\sim 75\,\text{K}$) of the cryogenic amplifier used.

Already from the measurements outlined above [combined with Power Spectral Density (PSD) noise measurements, see next section] we may extract the capacitive sensitivity of the microscope. However, as an alternative approach we also made a sample without any topography but with dielectric contrast as sketched in Fig. 4.13a. This way we have two alternative ways of extracting the stability of the microscope, and both methods agree very well with each other. The fabrication steps for this dielectric sample is outlined in Appendix A. It consists of a silicon wafer with precision etched trenches with near-vertical sidewalls. The trench depth was verified by profilometry to be 25 ± 1 nm. A silicon oxide layer was
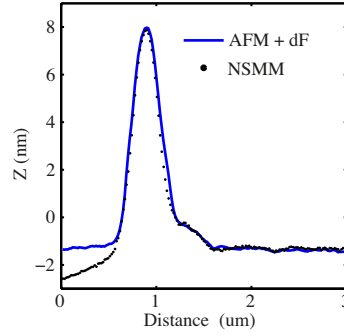
Figure 4.11: The NSMM trace (dots) and its reconstruction from the AFM topography and the simultaneously measured microwave frequency shift using a frequency-to-topography scaling factor of -4 kHz/nm.
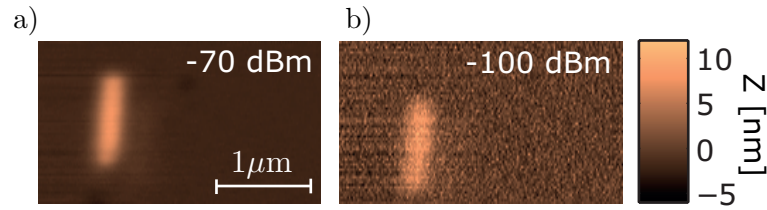
Figure 4.12: NSMM scan of the same sample as in Fig. 4.10 for when the cavity is populated with a) $\sim 10^6$ photons and b) $\sim 10^3$ photons.

sputtered on top, and polished to become flat with the desired thickness of 100 nm. Using angle-resolved elipsometry both thickness and dielectric constant of the SiO_2 can be deduced to within a few %.

The microwave response on top of this flat sample can then be used to estimate the capacitive sensitivity. Fig. 4.13d-f shows the obtained scans (with the same probe as in the previous experiment). This experiment also shows the power of NSMM not only for surface analysis but also sampling material properties beneath the surface [111].

4.5.3 Capacitive stability of the microscope

As discussed in [Paper II] we use two different methods to determine the noise level from the two samples discussed above. Both approaches give almost exactly the same value for the sensitivity. The first approach directly looks at the SNR obtained in the NSMM scans, and converts that to effective capacitance noise through the known properties of the dielectric sample. The second approach instead converts measured noise power spectral densities to capacitance noise, obtaining very similar numbers. The obtained sensitivity for three different photon numbers (or excitation powers) are shown in Fig. 4.14a. More points were not possible to obtain during the same cooldown due to other issues with the cryostat.

We achieve a total capacitive sensitivity of $6.4 \cdot 10^{-20}$ F/$\sqrt{\text{Hz}}$ (at -70 dBm excitation or $\sim 10^5$ photons in the resonator). At -100 dBm excitation the sensitivity is $3.7 \cdot 10^{-19}$ F/$\sqrt{\text{Hz}}$. At high excitation powers the mechanical contribution to frequency noise is around 200 Hz/$\sqrt{\text{Hz}}$, which dominates over electrical noise by two orders of magnitude. The increased
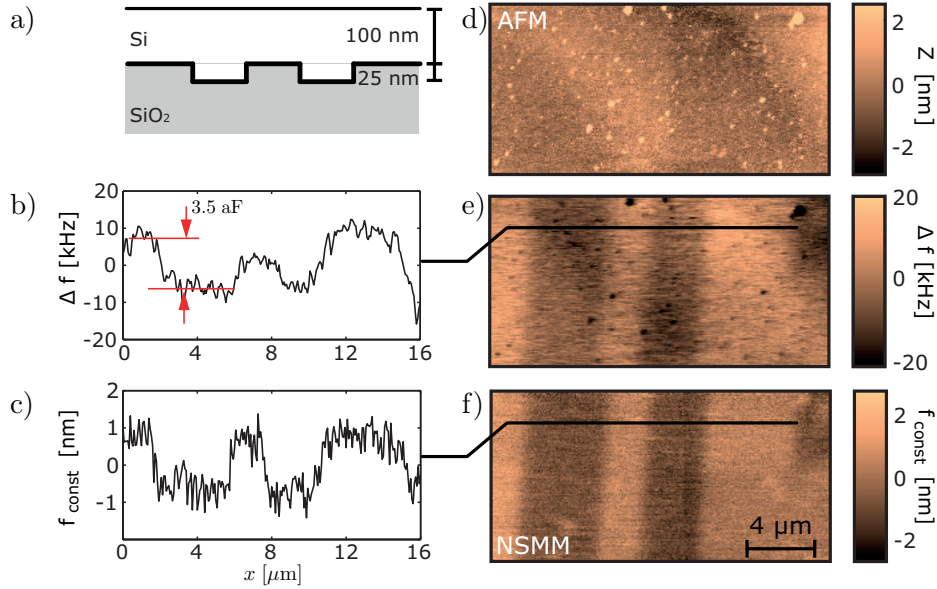
Figure 4.13: a) Sketch of the sample. 25 nm deep trenches are made in silicon using isotropic plasma etching to produce straight side-walls. SiO_2 is sputtered on top and then polished down to 100 nm to remove topographic effects. b) and c) are line traces from scans in e) and f) respectively. d) AFM topography of the sample. e) Microwave frequency shift in the same region, acquired simultaneously as d). f) A surface of constant capacitance obtained when using the microscope in pure NSMM mode, using the microwave resonance frequency as feedback. Obtained at 300 mK with roughly 10^5 photons in the resonator.

noise at low powers we attribute to the cold amplifier used in the experiment, which had a noise temperature $T_N \sim 75$ K. Thus, the performance of the microscope could be greatly improved by reducing mechanical noise further and to achieve lower photon numbers we need to use a microwave amplifier with lower noise temperature. However, as will be demonstrated in the next chapter, the already achieved sensitivity and photon number could in principle be used for qubit characterization.

When calculating the sensitivity we assume the worst possible situation: the noise figures are taken as the maximas in both spectra, close to the DC limit. Unfortunately this is also the frequency range in which we measure when scanning, the effective sampling rate ranging from a few tens of Hz up to around 100 Hz. Another way to improve sensitivity would be to use a heterodyne technique at higher frequencies. For example, to weakly modulate the z-coordinate (~ 1Å) at kHz frequencies (that can be tracked by the PDH loop), and demodulate the frequency response.

Interestingly, the measured noise level from the PDH loop is very low, in fact it is lower than the typical intrinsic noise of superconducting resonators [36, 37, 112]. This is not a result of lower noise in our resonators, instead some of this slow noise is compensated for by the feedback loop, making it appear as mechanical instabilities. [4]

---

[4]This shows that controlled tuning of the cavity frequency can be used to stabilize the microwave cavity using the PDH technique, smilar to the commonly used PDH-mediated stabilization of optical cavities and lasers [74]. This can for example be used to improve spectral purity of cavity based photon sources in c-QED.
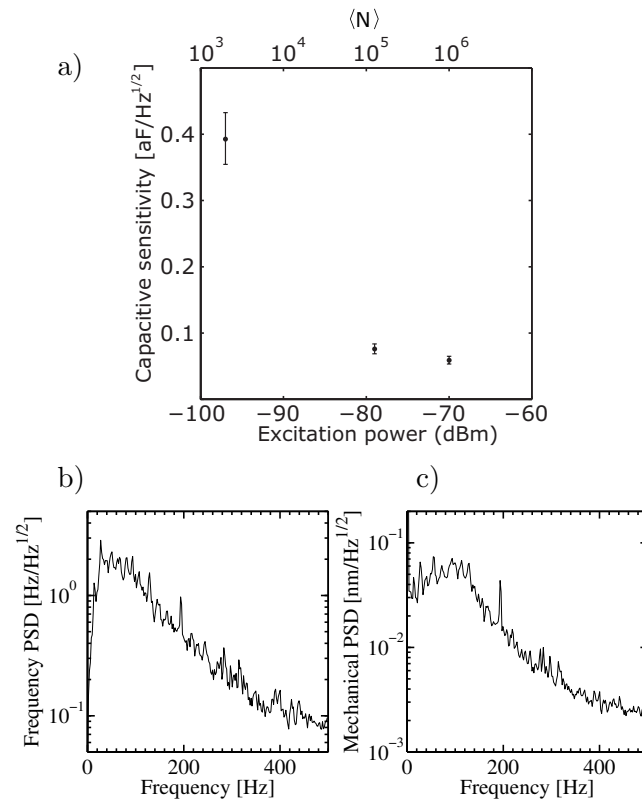
Figure 4.14: a) Total capacitive sensitivity of the NSMM microscope as a function of excitation power. b) Residual frequency noise spectral density (bandwidth-limited to 150 Hz) at -70 dBm excitation. Measured at the VCO input of the PDH loop. c) Mechanical noise spectral density (limited by the time constant of the AFM feedback loop to 150 Hz) at -70 dBm excitation. Data in b) and c) was acquired using the built in spectrum analyzer of our SPM controller (SPECS Nanosis controller).

5

MEASURING A TWO-LEVEL SYSTEM IN THE NSMM CONFIGURATION

In this chapter we will consider the interaction between a microwave resonator and a two-level system. Several different regimes will be discussed, and evaluated in terms of their application to NSMM. Ultimately, NSMM puts several restrictions on how we can interact with the two-level system which sometimes calls for a different theoretical interpretation of the results. In order to, in a controlled way, mimic the conditions of near-field scanning over a two-level system a test sample was fabricated. From the measurements on this test sample we can evaluate the feasibility of using NSMM to study two-level systems. In this sample we also reached an interesting new regime where photon-assisted pair-breaking in the system shows some unexpected results, and it opens up for another direction: Integration of a robust charge sensor onto the NSMM tip. This will be discussed in the next chapter.

5.1 Two-level systems

5.1.1 A generalized two-level system

We start by considering a generalized two-level system (TLS) described by the uncoupled energy levels $E_\pm(\xi)$ and their difference $E_+(\xi) - E_-(\xi) = \delta E(\xi)$ that could be tuned by an external parameter ξ. The levels are coupled with strength Δ_{TLS} such that the Hamiltonian describing the two-level system can be written

$$H_{\mathrm{TLS}} = \frac{\delta E(\xi)}{2}\sigma_z - \frac{\Delta_{\mathrm{TLS}}}{2}\sigma_x, \tag{5.1}$$

where $\sigma_z = |0\rangle\langle 0| - |1\rangle\langle 1|$, $\sigma_x = |0\rangle\langle 1| + |1\rangle\langle 0|$ are the Pauli matrices. Note that this Hamiltonian is equivalent to a spin $1/2$ particle in a magnetic field (see Chapter 7). In general δE is tuneable by some external control field, and in our case we assume that this is an electric field (RF or DC). The energy of the coupled levels become $E_\pm = \pm\frac{1}{2}\sqrt{(\delta E(\xi))^2 + \Delta_{\mathrm{TLS}}^2}$, and, given the right energy scales, microwave photons can induce transitions between these levels.

5.1.2 The single electron box

Qubits are another important realization of a TLS. In particular, we are here interested in a charge qubit which can be realized by making a single electron box (SEB) out of a superconducting material. The single electron box is a metallic island connected to a gate electrode via a capacitor C_g and to the ground via a tunneling barrier (with a capacitance

C_J), as shown in Fig. 5.1a. In the limit where the thermal energy ($k_B T$) is smaller than the charging energy of the island $E_C = e^2/2(C_g + C_J)$ and when the tunnel junction resistance is greater than the resistance quantum ($R_K = \hbar/e^2$), control over single charge tunneling events can be achieved in the box. The electronic energy levels when having n additional electrons on the island are given by

$$E_n = E_C \left(n - n_g\right)^2, \tag{5.2}$$

where $n_g = C_g V_g/e$. For $V_g = 0$ it is clear that the lowest energy of the system is achieved for $n = 0$. As we gradually increase V_g we will have to add electrons to the island one by one in order to keep the energy as low as possible. At zero temperature the single electron tunneling occurs when we pass the degeneracy point where $E_n = E_{n+1}$. The energy levels of the SEB are shown in Fig. 5.2.

5.1.3 The single Cooper-pair box (CPB)

The single Cooper-pair box (CPB) is similar to a single electron box, with the important difference that the island and the leads are made out of a superconducting material. In this case a gap opens up at the charge degeneracy points due to the Josephson effect in the SIS junction (tunnel barrier). This becomes a possible implementation of a charge qubit if we somehow can manipulate and read out the charge state of the superconducting island. The circuit in Fig. 5.1a can be represented by the Hamiltonian $H = E_C(n - n_g)^2 + E_J \cos \phi$, where $n_g = C_g V_g/e$ is the gate charge, E_J the Josephson energy and ϕ is the phase difference across the junction (originating from the DC Josephson relation). Because the phase and the charge are conjugate variables ($[n, \phi] = -i/2$) it is possible to rewrite the Josephson term in the Hamiltonian into the charge basis [113].

$$H_{\text{CPB}} = E_C(\hat{n} - n_g)^2 - \frac{E_J}{2} \sum_n (|n+2\rangle\langle n| + |n\rangle\langle n+2|), \tag{5.3}$$

where $\hat{n} = \sum_n n|n\rangle\langle n|$. H_{CPB} spans the full Hilbert space of all integer values of n, however, Cooper-pair tunneling only couples states which differ by two units of charge. We can therefore define two different subspaces: the even ($\hat{n} = ..., -2, 0, 2, ...$) or the odd ($n = ..., -3, -1, 1, 3, ...$) subspace that so far are decoupled and define wether we have an unpaired electron on the island or not.
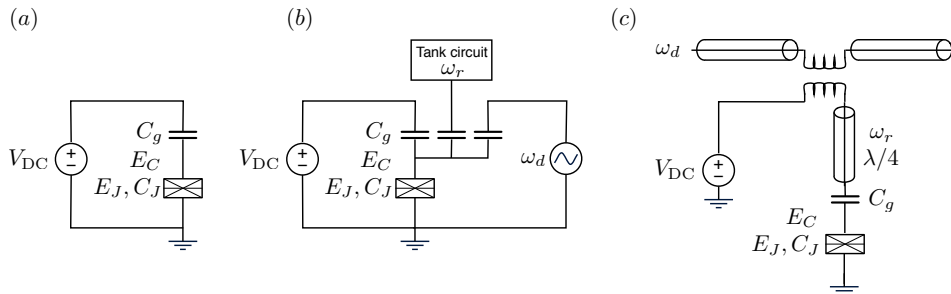
Figure 5.1: a) Circuit schematic of a Cooper-pair box coupled to a voltage source. b) Typical setup used for quantum capacitance measurements in the microoawave driven CPB. c) Setup used in our experiment as required by the NSMM geometry.
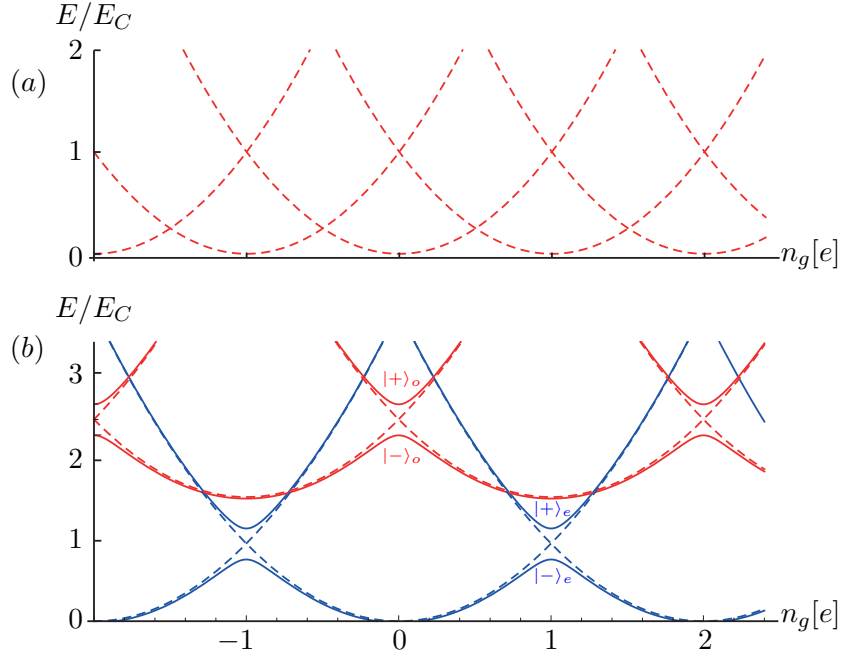
Figure 5.2: (a) Energy levels of the SEB and (b) the CPB as a function of gate charge. Even (blue) and odd parity (red) shifted by Δ in energy.

To simplify, we may consider only one charge degeneracy point, neglecting all other charge states. The resulting Hamiltonian of the two subspaces in the two-state approximation [114] can be written in analogy with eq. (5.1)

$$H_{\mathrm{CPB}}^{\mathrm{e}} \approx 2E_C(n_g - 1)\sigma_z - \frac{E_J}{2}\sigma_x = \frac{\delta E_C^{\mathrm{e}}}{2}\sigma_z - \frac{E_J}{2}\sigma_x, \tag{5.4}$$

$$H_{\mathrm{CPB}}^{\mathrm{o}} \approx 2E_C n_g \sigma_z - \frac{E_J}{2}\sigma_x = \frac{\delta E_C^{\mathrm{o}}}{2}\sigma_z - \frac{E_J}{2}\sigma_x. \tag{5.5}$$

Diagonalizing (5.4) we get the energy levels of the system for the even parity

$$E_{\pm}^e = \pm\frac{1}{2}\sqrt{(\delta E_C^{\mathrm{e}})^2 + E_J^2}. \tag{5.6}$$

Thus a gap of magnitude E_J will open up at the degeneracy point. The (even) energy bands for the CPB are shown in Fig. 5.2, calculated using the full Hamiltonian eq. (5.3). We can write the eigenstates of the reduced two-level CPB by means of the mixing angle $\theta = \arctan[E_J/\delta E_C^{\mathrm{e/o}}]/2$ such that

$$\begin{aligned} |-\rangle_e &= \cos\theta|0\rangle - \sin\theta|2\rangle \\ |+\rangle_e &= \sin\theta|0\rangle + \cos\theta|2\rangle. \end{aligned} \tag{5.7}$$

and similarly for the odd parity

$$E_{\pm}^o = \pm\frac{1}{2}\sqrt{(\delta E_C^{\mathrm{o}})^2 + E_J^2} \quad \text{and} \quad \begin{aligned} |-\rangle_o &= \cos\theta|-1\rangle - \sin\theta|1\rangle \\ |+\rangle_o &= \sin\theta|-1\rangle + \cos\theta|1\rangle \end{aligned}. \tag{5.8}$$

Having an unpaired electron (quasiparticle) on the island is associated with the additional energy Δ. This shifts the odd energy levels by the corresponding amount, as shown in Fig. 5.2b.

5.2   Different regimes of low power NSMM

The NSMM interacting with a two-level system can be devided into different regimes based on the energy stored inside the probe

- Weak driving: below or near single photon population of the resonator. Here we can model the resonator response using dispersive readout or quantum capacitance models (described in the next section), depending on the parameters of the experiment.

- Strong driving: where the probing resonator is populated with a large number of photons such that we may use the Landau-Zener-Stuckelberg or the dressed states formalism to describe the behavior of the coupled system. The contrast in this regime scales with photon number as $N^{-1/2}$, and fades out for very high photon numbers.

- "Classical" NSMM, i.e. the limit $N \to \infty$.

The measurement of a two-level system in the NSMM configuration differs from what is typically used for readout in the strong driving regime. A typical circuit-QED sample design uses two separate microwave electrodes [115–117]; one for strong excitation and another weak probe for reading out the state of the TLS (see Fig. 5.1b) using either the concepts of the quantum capacitance or dispersive readout presented in the next section. This approach minimizes back-action and allows for a more intuitive interpretation of the measurement data. However, such a configuration becomes unfeasible in a scanning probe setup. Instead we have to consider the situation when excitation and readout (and biasing) is done using the same probe (see Fig. 5.1c).

5.2.1   Weak driving: quantum capacitance

To read out the state of the CPB we can couple it to the electric field of a microwave resonator. In a quasi-classical picture the instantaneous gate voltage can be written

$$n_g(t) = n_{g0} + A_{ng} \sin \omega_0 t, \qquad (5.9)$$

where n_{g0} is the static gate charge from before, ω_0 the resonance frequency and the microwave amplitude A_{ng} relates to the number of photons in the resonator as

$$A_{ng} = \frac{C_g V_g^{\mathrm{rf}}}{e} = \hbar \omega_0 C_g \sqrt{N} \sqrt{\frac{Z_0}{2\hbar e^2}} = \frac{\hbar \omega_0 C_g}{E_C C_\Sigma} \sqrt{N} \sqrt{\frac{\pi Z_0}{R_Q}}. \qquad (5.10)$$

The latter equality defines the amplitude in terms of the resonators wave impedance Z_0 and the resistance quantum $R_Q = h/4e^2$, and is the definition we use in [Paper IV]. We now make the assumption that $A_{ng} \ll 1$ and $\hbar \omega_0 \ll E_J$ such that the photon field slowly wiggles the gate charge of the box around its average value. Then the photon field does not introduce any transitions in the CPB, but merely probes the state of the qubit. In this limit the resonator experiences the box as a state dependent non-linear capacitance C_{eff}. Such a capacitance is defined by $C_{\mathrm{eff}} = \partial \langle Q_g \rangle / \partial V_g = C_{\mathrm{geom}} + 2C_g^2 (\partial \langle n \rangle / \partial n_g)/C_\Sigma$ [118], where the first term is a constant geometric capacitance and the second term is the quantum capacitance that depends on the expectation value of the charge

$$\langle n \rangle = \langle \pm | n | \pm \rangle = \mp \sin^2 \theta = \mp \left(\frac{1}{2} - \frac{\delta E_C^{e/o}}{2\sqrt{(E_C^{e/o})^2 + E_J^2}} \right), \qquad (5.11)$$

such that

$$C_Q = 2\frac{C_g^2}{C_\Sigma}\frac{\partial\langle n\rangle}{\partial n_g} = \frac{4C_g^2 E_J^2 \delta E_C^{e/o}}{C_\Sigma((\delta E_C^{e/o})^2 + E_J^2)^{3/2}}\sigma_z \equiv -\frac{C_g^2}{e^2}\frac{\partial^2 E_\pm^{e/o}}{\partial n_g^2}. \tag{5.12}$$

The quantum capacitance is directly related to the curvature of the energy bands of the CPB, and it is at maximum at the degeneracy point of the CPB. The resonator responds to this additional capacitance just like any other additional capacitance, c.f. eq. (4.13).

5.2.2 Strong driving: Landau-Zener-Stückelberg interferometry

We now consider the more general situation with no assumptions made about the driving field in eq. (5.9). The picture is given in Fig. 5.3a: The CPB is driven by a gate voltage that evolves the system around the degeneracy point according to $n_g(t)$.
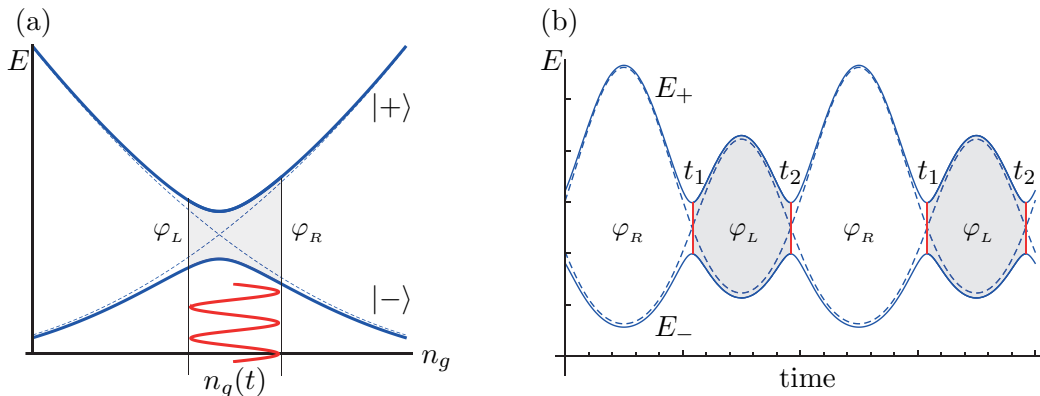
Figure 5.3: (a) A two-level system subject to a continous driving field $n_g(t)$ with amplitude A_{ng}, centered around an arbitrary position $n_g = n_{g0}$. The accumulated Stückelberg phase φ is proportional to the area between the energy levels in the drive region. (b) Time-evolution of the energy difference, LZ-tunneling may occur at times t_1 and t_2.

At strong enough drive the adiabatic approximation fails and the possibility appears that the CPB can tunnel between its ground and excited states as a result of the drive. As shown by Landau and Zener in 1932 [119, 120] the probability to tunnel depends on the rate at which the system is swept across the point of minimum energy separation. This applies to a wide range of different two-level systems found in nature [121]. For the specific case of the CPB we get the Landau-Zener tunneling probability

$$P_{LZ} = \exp\left(-2\pi\frac{E_J^2}{4\hbar\nu_0}\right), \tag{5.13}$$

where the slew rate at the degeneracy point ν_0 is obtained from the energy difference of the non-interacting levels $E_n = 4E_C(n_g - n)^2$. Restricting the problem to a single TLS we have

$$\nu(t) = \frac{\partial(E_2 - E_0)}{\partial t} = 2E_C A_{ng}\omega\cos\omega t. \tag{5.14}$$

The point in time where the gate signal crosses the degeneracy point $(n_g(t) = 1)$ is obtained from eq. (5.9), $\omega t = \arcsin\left[(n_{g0} - 1)/A_{ng}\right]$, and the slew rate when passing the degeneracy point can be written

$$\nu_0 = 2E_C\omega\sqrt{A_{ng}^2 - (n_{g0} - 1)^2} \tag{5.15}$$

Note that this equation is only valid when we are actually crossing the degeneracy point with the RF drive.

If the system is continously driven (faster than the dephasing time T_2) across the degeneracy point the final state of the system will be the result of many consecutive tunneling events. For example, starting in the ground state, for one period of the driving signal the system may evolve through two different paths and end up in the excited state: Either tunneling happens during the up sweep, or during the down sweep. Similarly, we may find the system in the ground state if no tunnelling occured or if two consecutive tunneling events occured after one full period of the drive. These tunneling events may interfere constructively or destructively depending on the accumulated phase between tunneling events. This is the essence of the Landau-Zener-Stückelberg interferometry - quantum phase interference due to an energy dispersion. In general it is possible to define the phase shift when moving across the energy landscape as

$$\varphi \;=\; -\frac{1}{\hbar}\int_{t_1}^{t_2}(E_+ - E_-)dt. \tag{5.16}$$

The accumulated phase on the left and right sides of the crossing point is given by this integral evaluated between consecutive times crossing the degeneracy point. The Stückelberg phase can thus be devided into two parts for a full drive cycle, φ_L and φ_R, as shown in Fig. 5.3b. When the accumulated phase difference ($\varphi_L - \varphi_R$) is a multiple of 2π tunneling events will interfere constructively and we find the system in the excited state with enhanced probability.

It is possible to derive the time averaged (over many drive cycles) probability to find the system in the excited state in the presence of decoherence. This derivation is given in detail in Ref. [121] and the result for a driven CPB reads

$$P_+(A_{ng}, n_{g0}) = \frac{1}{2}\sum_m \Delta_m^2 \left(\frac{1}{T_1 T_2} + \frac{T_2}{T_1}(m\omega_0 - 4E_C n_{g0}/\hbar)^2 + \Delta_m^2\right)^{-1} \tag{5.17}$$

where $\Delta_m = (E_J/\hbar) \times J_m(4E_C A_{ng}/\hbar\omega_0)$ and J_m are Bessel functions. The relaxation T_1 and dephasing T_2 rates are phenomenologically introduced through the Bloch equations. Notably, eq. (5.17) describes a set of Lorentians separated in the space spanned by A_{ng} and n_{g0} whose width is determined by the relaxation in the system. An example of the generated interference pattern is shown in Fig. 5.4. LZS interference has recently been studied in a wide range of systems, ranging from flux qubits [122], charge qubits [117] to nanomechanical circuits [123], NV centers in diamond [124] and quantum dots [125, 126] and provides for a convenient way of characterizing the two-level system.

A typical setup when measuring this type of LZS interference is depicted in Fig. 5.1b [115–117, 127]. Two separate electrodes are used, one to excite the system with a strong signal and another one to monitor the state of the CPB using a weak resonant probe that extracts the quantum capacitance of the CPB. In a scanning probe setup this becomes less convenient and we must use the same electrode to both read out and excite the system. We shall therefore proceed with deriving an equivalent model using a full Hamiltonian description. Allthough similar to the LZS model this provides us with a different interpretation of the results, a convenient way to include a strong oscillator both as readout and excitation, and a way of introducing relaxation in the system from first principles.

5.2.3 Full Hamiltonian approach: dispersive regime

First we again consider the weak driving regime, where a general TLS is coupled to a microwave resonator, and the resonator is populated with a small number of photons. We assume that the resonator is detuned from the TLS with splitting $\delta\omega = |\omega_0 - \Delta_{\text{TLS}}/\hbar| \gg g$, but the resonance frequency is on the same order as the TLS frequency ($\omega \simeq \Delta_{\text{TLS}}/\hbar$) such that the system is no longer probed adiabatically. This regime is called the dispersive regime. We can here model the complete NSMM setup and the TLS using a generalized Jaynes-Cummings Hamiltonian $H = H_{\text{osc}} + H_{\text{TLS}} + H_{\text{coupling}}$:

$$H = \hbar\omega_0 a^\dagger a + \frac{\delta E(\xi)}{2}\sigma_z - \frac{\Delta_{\text{TLS}}}{2}\sigma_x + g(a^\dagger + a)\sigma_z. \tag{5.18}$$

Due to the coupling g ($= \hbar\omega_0 C_g\sqrt{Z_0/2\hbar e^2 C_\Sigma^2}$ in the case of the CPB), both the states of the TLS and the states of the cavity will be shifted as compared to the uncoupled case. We can directly evaluate the frequency shift using the rotating wave approximation and a unitary transformation that eliminates the coupling-term [113]:

$$H_{\text{eff}} \approx \hbar\left(\omega_0 - \frac{g^2}{\delta\omega}\sigma_z\right)a^\dagger a - \frac{1}{2}\left(\Delta_{\text{TLS}} + \frac{\hbar g^2}{\delta\omega}\right)\sigma_z. \tag{5.19}$$

The resonator aquires a frequency shift $\pm g^2/\delta\omega$ due to the interaction with the TLS. The above expression is an approximation in which the dependence upon the number of photons in the cavity is removed. The validity of this regime holds only for a photon population N in the cavity such that $N < N_{\text{critical}} = \Delta_{\text{TLS}}^2/4g^2$. [128, 129] For a larger number of photons we can derive the frequency response of the cavity by using a dressed states formalism. In the adiabatic limit when $\hbar\omega_0 \ll \Delta_{\text{TLS}}$ we recover the frequency shift that is obtained from the quantum capacitance [113].

5.2.4 Dressed states

A different way of treating the LZS problem is the so called dressed states formalism. This was originally developed in the field of QED to study the interaction of single atoms and
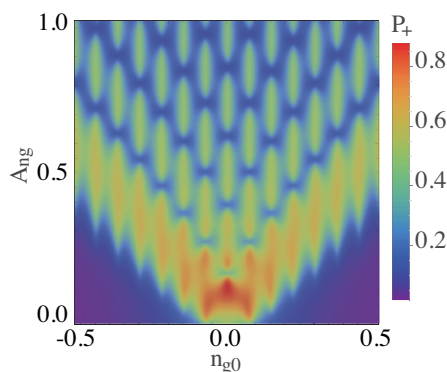
Figure 5.4: Example of a LZS interference pattern obtained through eq. (5.17) in the regime $\omega_0 T_1 = 3\omega_0 T_2 = 15$.

light [130]. We start with the same Hamiltonian as before albeit this time specific for the CPB. We assume the two-state approximation of the CPB.[1]

$$H = \hbar\omega_0 a^\dagger a + \frac{1}{2}\delta E_C^{e/o}\sigma_z - \frac{1}{2}E_J\sigma_x + g\sigma_z(a + a^\dagger). \quad (5.20)$$

The first term describes the oscillator, the second and the third are the qubit Hamiltonian eq. (5.2), and the last term describes the coupling between the resonator and the qubit. We may write down the eigenstates of the oscillator and the CPB (eq. (5.6)) separately. However, in the presence of the coupling term the energies will be shifted. The full system is therefore described by a new set of energies and eigenfunctions. The CPB energies become "dressed" by the photon states of the resonator. To evaluate the eigenstates of this Hamiltonian we first consider the case for $E_J = 0$, and then introduce non-zero off-diagonal matrix elements by perturbation theory to also include the case when $E_J \neq 0$. For $E_J = 0$ we first note that H commutes with σ_z, such that we may write two separate Hamiltonians depending on the projection onto the qubit state

$$H_\pm = \hbar\omega_0 a^\dagger a \pm \frac{1}{2}\delta E_C^{e/o} \pm g(a + a^\dagger) = \hbar\omega_0\left(a^\dagger \pm \beta\right)(a \pm \beta) - \beta^2\hbar\omega_0 \pm \frac{1}{2}\delta E_C^{e/o}, \quad (5.21)$$

with $\beta = -g/\hbar\omega_0$. Introducing the displacement operator for coherent states [130] $D(\pm\beta) = \exp\left(\beta a^\dagger - \beta^* a\right)$ which has the property $D(\pm\beta)a^{(\dagger)}D^\dagger(\pm\beta) = a^{(\dagger)} \mp \beta^{(*)}$ [131] we see that if we apply it to the above Hamiltonian we recover the harmonic oscillator

$$D(\pm\beta)H_\pm D^\dagger(\pm\beta) = \hbar\omega_0 a^\dagger a - \beta^2\hbar\omega_0 \pm \frac{1}{2}\delta E_C^{e/o}. \quad (5.22)$$

This means that the eigenstates of the "dressed" system is given by

$$|\pm, N\rangle = D(\pm\beta)|\pm\rangle|N\rangle, \quad (5.23)$$

and the eigen energies are

$$E_N^\pm = N\hbar\omega_0 + \beta^2\hbar\omega_0 \pm \frac{1}{2}\delta E_C^{e/o}. \quad (5.24)$$

These energies form a Wannier-Stark ladder structure as shown in Fig. 5.5. Now, including the Josephson term introduces off-diagonal elements in the above diagonalized Hamiltonian, coupling the qubit states with photon states differing by m photons. These matrix elements are given by

$$M_\pm(m) = \langle\pm, N - m|\left(-\frac{1}{2}E_J\sigma_x\right)|\mp, N\rangle. \quad (5.25)$$

Since σ_x only couples orthogonal states in the charge basis ($\langle\pm|\sigma_x|\mp\rangle = 1$), and by using the symmetry of the displacement operator, $D^\dagger(\mp\beta)D(\pm\beta) = D(\pm 2\beta)$, the matrix elements can be simplified to [131]

$$M_\pm(m) = -\frac{1}{2}E_J\langle N - m|D(\pm 2\beta)|N\rangle \approx -\frac{1}{2}E_J J_{\pm m}(4\beta\sqrt{N}). \quad (5.26)$$

The m-photon transitions of the dressed system is thus governed by Bessel functions. The argument of the Bessel functions depend on the number of photons in the cavity, N, and

---

[1]It can easily be extended to the many-charge states basis, which is what we need for later analysis. See [Paper IV] for details.
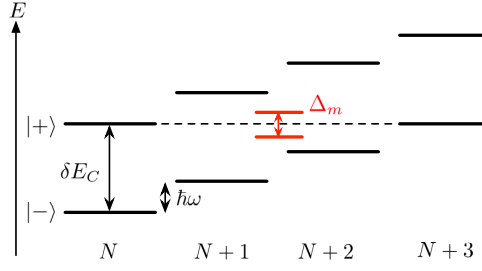
Figure 5.5: Dressed states energy level ladder. When δE_C is tuned such that the excited qubit state is on resonance with the ground state with m added photons in the cavity the two levels hybridize with gap Δ_m (here $m = 3$).

we may relate it to a drive amplitude A_{ng} through eq. (5.10). The energy of the two state system can thus be described by

$$E_{\pm,N} = N\hbar\omega_0 \pm \frac{1}{2}\sqrt{[\delta E_C - m\hbar\omega_0]^2 + [E_J J_m(4\beta\sqrt{N})]^2}. \tag{5.27}$$

We see that the resulting energy bands can be locally described by a single TLS, eq. 5.1, around each m-photon resonance with the splitting $\Delta_m = E_J J_m(4\beta\sqrt{N})$. Each dressed two level system can thus be described in accordance with eq. (5.7) on the form

$$|-, N\rangle_{e/o} = \cos\phi|n, N\rangle + \sin\phi|n+2, N-m\rangle \tag{5.28}$$

$$|+, N\rangle_{e/o} = \sin\phi|n, N\rangle - \cos\phi|n+2, N-m\rangle, \tag{5.29}$$

With increasing microwave amplitude the matrix element and the m-photon transition probabilities will oscillate, going from large to small transition probabilities and so on. This an analog of the LZS problem, and we can see the similarity to eq. (5.17).

To calculate the response of the NSMM probe we note that the measured quantity is the frequency of the photons leaking out from the cavity. Thus, the frequency shift can be defined as $\delta\omega = E_{\pm,N}/\hbar - E_{\pm,N-1}/\hbar - \omega_0$. We can linearize eq. (5.27) in the limit $N \gg 1$ and determine the response of the cavity (NSMM probe)

$$\delta\omega(N, n_g) = \sum_m \frac{\beta}{\hbar\sqrt{N}} \frac{E_J \Delta_m J'_m(4\beta\sqrt{N})}{\sqrt{[\delta E(n_g) - m\hbar\omega_0]^2 + \Delta_m^2}}, \tag{5.30}$$

where $2J'_m(x) = 2\partial J_m(x)/\partial x = J_{m-1}(x) - J_{m+1}(x)$. Note that if the energy in the resonator is too high (N large) it will saturate the dressed system and $\delta\omega \to 0$.

Eq. 5.30 describes the frequency of the NSMM probe in the absence of decoherence. In any practical situation the TLS is coupled to some extent to its environment and this leads to dissipation and loss of coherence. By applying the proper model for relaxation we can learn about many critical parameters of the TLS, not only the properties within eq. 5.30 but also relaxation, dephasing and quasiparticle rates, all of which significantly influence the performance of a superconducting qubit.

Quantity	Symbol	Value	Unit
Resonator frequency	$\omega_0/2\pi$	0.32/6.94	K/GHz
Resonator Internal Q	Q_i	76 000	-
Resonator External Q	Q_c	57 000	-
Charging energy	E_C	1.1/24.4	K/GHz
Josephson energy	E_J	0.22/4.82	K/GHz
Junction capacitance	C_J	741	aF
Gate capacitance	C_G	50	aF

Table 5.1: Parameters extracted from the CPB.

5.3 Test sample: LZS interference in the NSMM configuration

In order to better understand how our NSMM probe would respond to a TLS we fabricated a sample consisting of a CPB (weakly) capacitively coupled to a "first generation" fractal resonator. This resonator has many characteristics similar to the ones described in Chapter 2, except for a well defined symmetry point to introduce DC bias (this eventually lead to the evolution of the final fractal design). The sample consisted of said Nb cavity on sapphire and the CPB made out of aluminium (see Appendix A for details) and the layout is shown in Fig. 5.6. The cryogenic setup was similar to that used in the NSMM, but the measurement was performed in a dilution fridge at 20 mK. For every resonator excitation power the gate voltage is slowly ramped (2.7 Hz) and the PDH loop is used to track the resonance frequency of the cavity as a function of the applied gate voltage. Several such ramps are collected and averaged (8 averages) to produce the data in Fig. 5.7. The frequency shift pattern of the cavity resembles that of LZS interference, as described in the previous section. Some of the extracted values of the cavity and CPB are given in Table 5.1. In the context of NSMM we make a few observations regarding the data in Fig. 5.7. The new physics discovered in this sample will be discussed in the next chapter.

- The extracted gate capacitance C_G is in the range of what we could expect for NSMM. For example, it is equivalent to the capacitance of a sphere with radius 110 nm separated from a metallic surface by 2 nm.
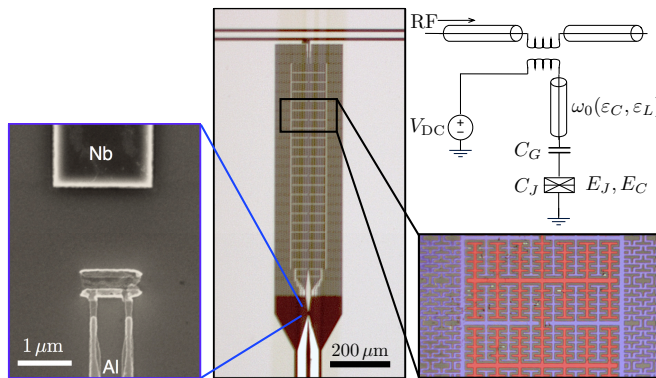
Figure 5.6: Image of the test sample and its circuit representation.
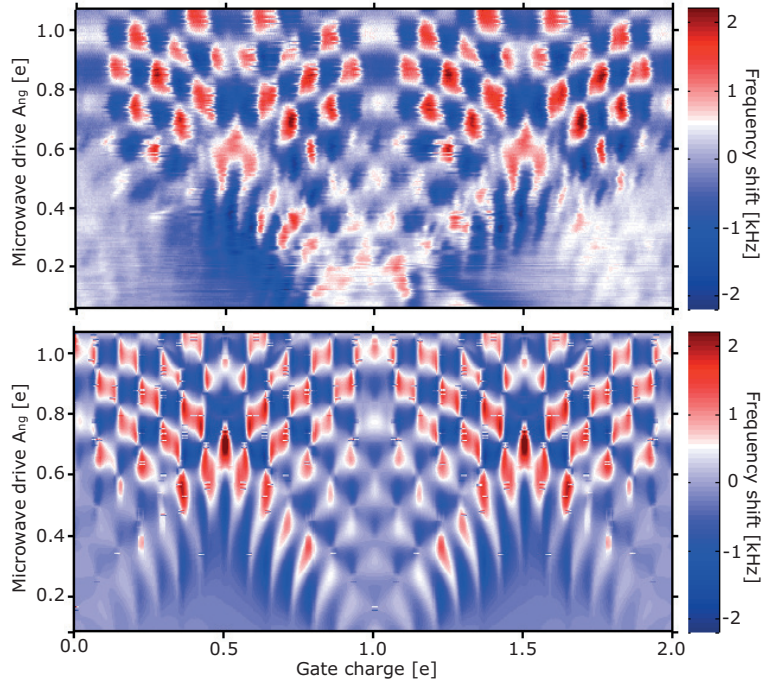
Figure 5.7: Measured (top) and calculated (bottom) LZS interference pattern of a CPB coupled to a high-Q cavity in the NSMM configuration.

- The measured frequency shift is relatively small, and if converted to capacitance (as seen by the cavity) the color scale in Fig. 5.7 ranges between $\pm$ 0.8 aF. We also note that the drive amplitude that goes from 0.1 to 1e corresponds to a photon population in the cavity ranging from $\sim 10^2$ to $\sim 10^5$ photons. This should be put in context of the noise levels measured in our NSMM. For ~ 1000 photons in the cavity we have a stability better than 0.4 aF/$\sqrt{\text{Hz}}$. A similar interference structure should therefore be detectable using our NSMM.

- As pointed out also in [Paper IV] the theoretical frequency shift at low drive strengths (quantum capacitance) should be on the order of 100 kHz, rather than the measured ~ 1 kHz. The descipancy is due to strong quasiparticle poisoning (see next chapter). However, the absence of such quasiparticle poisoning would improve the signal-to-noise ratio in the NSMM considerably when detecting a qubit in the scanned sample.

5.4   Outlook: Prospects for low power resonant NSMM

While the NSMM developed during this thesis still has several shortcomings, future improvements certainly would make this type of tool very useful. Here we look at some of the most important applications and modifications that can be implemented, on top of an overall improved performance and stability.

5.4.1 Qubit characterization

Current circuit-QED architectures have been limited to only a couple of qubits to study fundamental properties in these systems. Large scale integration will face many new obstacles before it becomes a useful tool that can solve advanced problems by quantum computation. There have been many proposals on how to implement large scale superconducting quantum circuits with integrated error correction, specifically topological computation using surface codes appears promising for this purpose [4, 5]. In such circuits individual addressing of a single qubit becomes difficult, but knowledge of individual qubit properties is still important for programming and debugging of the circuit. For this purpose a NSMM as the one demonstrated in this thesis could become particularly useful. The results demonstrated here show that resonant NSMM can be brought to the quantum limit. Thus in the strong driving regime the NSMM probe can be placed on top of individual qubits and characterization done in the strong driving regime. As mentioned earlier in this chapter, LZS (or dressed states) spectroscopy can reveal many properties about the qubit itself and its environment [121], and especially in the fourier domain [132, 133] analysis becomes more straightforward.

This technique can be used to find defective qubits as well as to learn about how the qubit interacts with the large scale qubit environment. It thus has the potential to become as important for the development of large scale quantum device circuits, as scanning capacitance microscopy and "classical" NSMM have been in the development of todays CMOS circuits.

5.4.2 Spectroscopy of two-level fluctuators

In this section we will consider a special class of samples whos study is of particular interest in the development of better quantum circuits. The electric field in a coplanar resonator is widely distributed which results in both the (weak) coupling to many TLFs (electric field at any given location is never very large) and cavity-mediated energy exchange between spatially separated resonant TLFs. Due to this individual TLFs cannot be resolved in standard resonators.

A single TLF

Two-level fluctuators (TLFs) have already been discussed in the context of dielectrics (see Chapter 2) and here we are instead interested in a single TLF, that we can couple strongly to. Such a TLF can be described by eq. (5.1), and they can be found in for example aluminium tunnel junctions [134, 134–138]. Interestingly, if the probing power is low enough, such TLF defects can be used for quantum computation since they can have relatively long relaxation times [134, 135]. However, in general such defects pose a problem for engineered quantum systems since they provide for alternate channels of energy decay. These TLFs are very easily saturated: a single photon will saturate the system until the same photon goes back to its source (resonator) or is dissipated to the environment. This means that we need an extremely low probing power if we want to study these systems, typically an average photon population $\langle N \rangle \lesssim 1$ [137].

TLF spectroscopy have been demonstrated in Josephson junctions where a single TLF can couple strongly to the electric field over the junction[135, 136]. The response is detected by qubit resonant interaction, where the qubit energy is tuned into resonance with the TLF splitting, strongly coupling the two systems and resulting in a qubit frequency shift. The
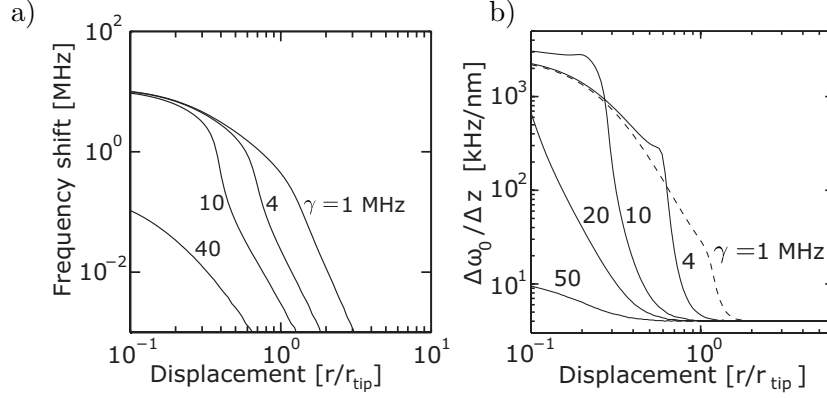
Figure 5.8: a) Calculated frequency shift of the NSMM probe as a function of its displacement from atop the TLF for several values of the TLF linewidth γ in the dispersive regime. The calculation assumes a TLF detuning $\omega_0 - \omega_{\mathrm{TLF}} = 2\pi \cdot 100$ kHz, $\omega_0/2\pi = 5$ GHz, $Q = 50000$, and typical TLF parameters from literature. The geometry is given in Fig. 5.9a and we use $h_0 = 2$ nm, $h_\varepsilon = 1$ nm. b) Change in cavity frequency due to a vertical displacement Δz for the same conditions as in a).

coupling between the TLF and the qubit/resonator is given by

$$g = \frac{ed}{x\pi\hbar}\sqrt{\frac{\hbar\omega_0}{2C_0}}\sin(\eta), \tag{5.31}$$

where ed/x is the effective dipole moment induced by the tip on the TLF situated at a distance x from the tip, C_0 the cavity capacitance and η the angle of the dipole relative the electric field (from the tip). The square root signifies the voltage due to a single photon in the cavity.

The situation when interacting with a single TLFs using NSMM is similar. The electrostatic energy is maximized at the near-field tip and the magnitude can be made essentially the same as in a junction. However, in the case of NSMM the coupling will be reduced since the probe is separated from the dielectric layer containing TLFs. In the case of aluminium which has an oxide thickness of 2-3 nm a NSMM working distance of 3 nm will thus reduce the coupling by ~50%. A typical value for the TLF dipole moment in aluminium junctions is $d = 0.13$ nm [136], and assuming a reduction of 50% in the NSMM case we get $g_{max} \approx 30$ MHz ($\eta = \pi/2$). This is still a strong coupling and should be readily detectable using NSMM.

The spatial resolution in mapping of the frequency shift due to TLFs can be higher than the size of the tip. The quadratic dependence of the cavity frequency shift on the coupling results in a signal strongly localized on top of the TLF.

In Fig. 5.8a we have evaluated the frequency shift of the NSMM probe caused by a single, ideally coupled TLF. The corresponding geometry is shown in Fig. 5.9. The coupling to the TLF as a function of the tip displacement from the TLFs origin is evaluated from eq. (5.31), considering the electric field projection onto the axis perpendicular to the sample surface obtained from a perturbative approach using image charges [139]. Given the coupling, the cavity shift in the dispersive regime, c.f. eq. (5.19), can be evaluated using a Master equation and a Lindblad formalism (see appendix D) to also include dissipation to the environment. The parameters used in the calculation in Fig. 5.8a are typical for our NSMM and the various linewidths shown correspond to a typical range observed in aluminium oxide [135].
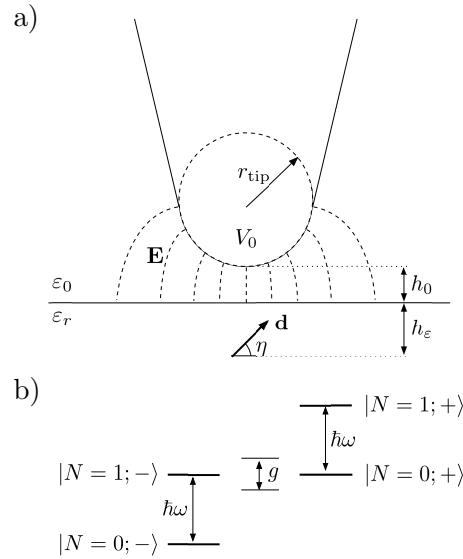
Figure 5.9: a) Geometry considered for the coupling of a TLF to the NSMM probe. The TLF is located a distance $h = h_0 + h_\varepsilon \ll r_{\text{tip}}$ from the apex of the tip. The TLF couples through the electric field from the tip projected onto the direction of its dipole moment oriented with an angle η with respect to the z-axis. b) For strong enough coupling g the degenerate states $|1;-\rangle$ and $|0;+\rangle$ hybridize, resulting in a shift of the frequency of the NSMM probe.

The sudden drop in response around $r = r_{\text{tip}}$ in Fig. 5.8a comes from the transition from the strong to the weak coupling regime. However, even in the weak coupling regime it may be possible to detect a TLF by the resulting small frequency shift. Mechanical noise will directly influence the coupling to the TLF and will add low frequency noise to the frequency read-out channel. This can however be used as an advantage. In Fig. 5.8b we have evaluated the change in microwave frequency as the tip is vertically displaced by ± 1 nm. This could represent either noise or the deflection due to the oscillatory motion of a cantilever as the readout is done in parallel with AFM distance control. The microwave readout can easily be made fast enough to track the changes due to mechanical oscillations of the cantilever and measurement of the quantity $(\partial f_0/\partial z)_{\text{TLF}} \sim$ MHz/nm gives a very high contrast in the regime shown in Fig. 5.8b compared to the capacitive contribution from a metallic surface, which is on the order of $(\partial f_0/\partial z)_{\text{cap}} \sim$ kHz/nm [Paper II]. At typical cantilever frequencies (10s of kHz) mechanical noise also plays a much smaller role.

The advantage of operating in the dispersive regime is that the frequency span is not limited by the cavity linewidth. The cavity shift can be detected (in the case of strong coupling) even when the detuning of the TLF frequency is much bigger than the cavity linewidth. We are thus not limited by the bandwidth of the NSMM resonant probe (~ 300 kHz for $Q \sim 15000$) which would result in very sparsely located detectable TLFs, which density is in the order of $0.1 - 1\mu m^{-2}\text{GHz}^{-1}$ in Al_2O_3 for example [136].

Dielectrics with dense TLF distributions

If we instead have a large amount of TLFs that have overlapping spectra [9] the situation becomes very different. If the NSMM tip is static the TLFs in the probed sample volume are indistinguishable from TLFs coupled directly to the NSMM resonator, intrinsic to its

substrate and interfaces. However, if the NSMM tip is oscillating, so does the coupling to the TLFs. In such an experiment the contribution from the TLFs in the sample could be extracted, see Fig. 5.8b.

One advantage in a scanning probe setup is that the electric field can be made much stronger than inside a superconducting coplanar resonator. The TLF ensemble under the tip will thus couple each individual TLF up to $\sim 10^4$ times stronger. However, the coupled volume is less than one millionth of the resonator volume, such that dissipative effects from the tip constitutes only around $\leq 1\%$ of the total dissipation in the resonator. The q-PDH technique can successfully measure the quality factor of the cavity with an accuracy down to $\sim 0.1\%$.

5.4.3 Broadband resonant NSMM

The drawback of using a resonant NSMM probe is that its bandwidth is limited. Especially in the case of a high Q probe. For many applications it would therefore be desireable to be able to tune the frequency of the probe. Tuneable superconducting resonators are frequently used in circuit-QED in order to shift a resonator in and out of resonance with various qubits[140, 141]. This is typically realised by using the non-linear inductance of a superconducting quantum interference device (SQUID), and can shift a 6 GHz resonance by more than 1 GHz while keeping the quality factor in excess of 10^4 [141]. Integration of a SQUID into a resonator made of Nb on Si has been realized by many groups, and our superconducting NSMM probe fabrication would seamlessly integrate with SQUID fabrication (see appendix A). The SQUID inductance is tuned by an external flux, typically due to a current in an on-chip conductor, and it could easily be integrated into the mechanically separated microwave excitation of the resonator in our NSMM setup. Such a frequency-tuneable sensor would also be very useful in the classical NSMM regime, for wideband high-Q materials characterization.

5.4.4 Summary NSMM

In the previous chapter and in [Paper II] the performance of a cryogenic NSMM was demonstrated and we made the first steps towards a new regime of NSMM where the probing cavity is only populated with a small number of photons. We showed that it is possible to reach similar sensitivity and resolution with our microscope compared to other NSMMs reported in literature [79] that operate at much higher probing powers. This becomes possible due to the successful integration of a high Q superconducting cavity onto the tip. However, in order to reach our most ambitious goal of single photon population in the resonator and TLF interaction there are many things that must be further improved. For example,

- Mechanical stability shall be significantly improved.

- The cryogenic microwave amplifier used had a high noise temperature.

- The cryostat itself was not properly shielded, poisoning sensitive qubits, and other devices we tried to measure, with thermal photons.

- Integration into a dilution cryostat.

- Probe quality factors could be improved by further optimizing the design.

6

PHOTON ASSISTED QUASIPARTICLE TUNNELING IN THE CPB

The pattern shown in Fig. 5.7 has typical characteristics of LZS interference at low drive strengths. However, for stronger drive strength ($A_{ng} > 0.5e$) it behaves in a different way. This pattern shows an increased contrast and a strong bimodal behavior at each photon resonance condition. Due to the large amount of quasiparticle poisoning a naive assumption would be that the pattern at strong drives is the sum of the interference patterns from each subspace (odd or even number of charges on the island). This however does not explain the bimodal pattern observed. Going to the literature we find that bimodality in LZS interference patterns may be the result of population inversion and "relaxation" mechanisms that effectively bring the CPB into an excited state [115, 116]. It may therefore be plausible that the pattern that we observe is the result of a similar relaxation channel that in our case involves quasiparticles. This process is well described in [Papers III and IV], and this chapter instead aims to give a complementary view of the quasiparticle dynamics in this system and to highlight the applications of the observed regime.

Quasiparticle processes in CPBs and Single Cooper-Pair Transistors have been studied extensively during the last decade [142–148], and several methods have been found to reduce their presence in these devices [142, 147, 148]. However, eliminating quasiparticles completely at finite temperatures becomes very difficult and having a low probability of quasiparticle poisoning is not always advantageous over having more frequent quasiparticle tunneling on and off the island, since once poisoned the device will remain in this state for a significant amount of time. Here we instead try to make use of the presence of quasiparticles by operating the device in a regime where their contribution does not matter. This happens in the regime of ultrastrong driving of the CPB where the two-level approximation is no longer valid and multiple charge states have to be considered. The results presented in [Papers III and IV] consider these implications of multiple charge states and also the effect of quasiparticle tunneling in the strongly driven multileveled CPB.

6.1 Quasiparticle processes in the dressed CPB

While the Hamiltonian in eq. (5.3) only couples charge states differing by 2e, we defined in the previous chapter two scenarios for which we get two uncoupled Hamiltonians. We called these two subspaces the even and the odd subspace, depending on wether $\hat{n}$ is an even or odd number of electrons on the island. We now introduce the operator $\hat{C}_{\pm} = \sum |n \pm 1\rangle\langle n|$ that constitutes tunneling of a single electron and introduces transitions between the even and the odd subspace in the CPB. In analogy with eq. (5.26) this gives matrix elements on the
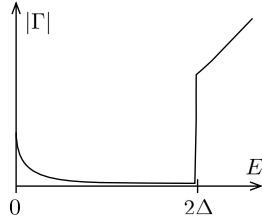
Figure 6.1: Quasiparticle tunneling rate between two superconductors with the same gap Δ.

form $J_m(\pm 2\beta\sqrt{N})$, with half the period compared to Cooper-pair tunneling. This operator is introduced together with a corresponding rate in the Bloch-Redfield master equation that describes the dynamics of the system. The rate that describes the quasiparticle tunneling is obtained from the general rate that describes tunneling between two superconductors [42]

$$\Gamma(\delta E) = \frac{2E_J}{h\Delta} \int d\omega \int d\omega' f(\omega)[1-f(\omega')]\rho(\omega, \Delta_{\text{island}})\rho(\omega', \Delta_{\text{lead}})\delta(\omega - \omega' + \delta E) \quad (6.1)$$

Here $f(\omega) = [1 - \exp(\omega/k_B T)]^{-1}$ is the Fermi distribution and

$$\rho(\omega, \Delta) = \frac{\Theta(\omega^2 - \Delta^2)|\omega|}{\sqrt{\omega^2 - \Delta^2}} \quad (6.2)$$

is the BCS density of states of the superconductor with gap Δ, and δE is the energy difference between initial and final state for this tunneling event. In general the island and the lead of the CPB can have different superconducting gaps, depending on fabrication conditions. If we make the simplification $\Delta_{\text{lead}} = \Delta_{\text{island}} \equiv \Delta$ it reduces to

$$\Gamma(\delta E) = \frac{2E_J}{h\Delta} \int d\omega f(\omega)[1 - f(\omega + \delta E)]\rho(\omega, \Delta)\rho(\omega + \delta E, \Delta). \quad (6.3)$$

The general form of this tunneling rate is shown in Fig. 6.1 at finite temperatures. Already here we can see that quasiparticle tunneling can be triggered by two different mechanisms. First, near $\delta E = 0$ there is an increased tunneling rate due to the overlap of the DOS tails at the gap edges. This leads to non equilibrium quasiparticle tunneling, and in general a lower temperature will suppress this rate. However, depending on the small differences that may arise in the island and lead gaps, the CPB can be pinned to the odd parity state if $\Delta_{\text{island}} < \Delta_{\text{lead}}$ [142]. Thermal activation will then bring the system back to the even parity. This is the reason why we see a strongly reduced frequency response in Fig. 5.7 at low drive strength and temperature: the CPB is pinned to the odd parity most of the time.

Secondly, when $\delta E \gtrsim 2\Delta$ energy from the cavity can be used to overcome the superconducting gap, resulting in a pair breaking event. In the dressed states picture this happens when the number of photons involved in the process, m, exceeds the gap $m\hbar\omega_0 > 2\Delta$. The difference between these two processes is that they couple different states in the dressed basis. Nonequilibrium quasiparticle tunneling induce transitions $|n, N\rangle \to |n \pm 1, N\rangle$ without changing the photon number, while the photon-asssisted tunneling takes the system from a state $|n, N\rangle$ to a state $|n + 1, N - m\rangle$.

Finally, we must also consider the asymmetry in the quasiparticle rate. This arises from the small dimensions and charging energy of the island. Due to the limited DOS of
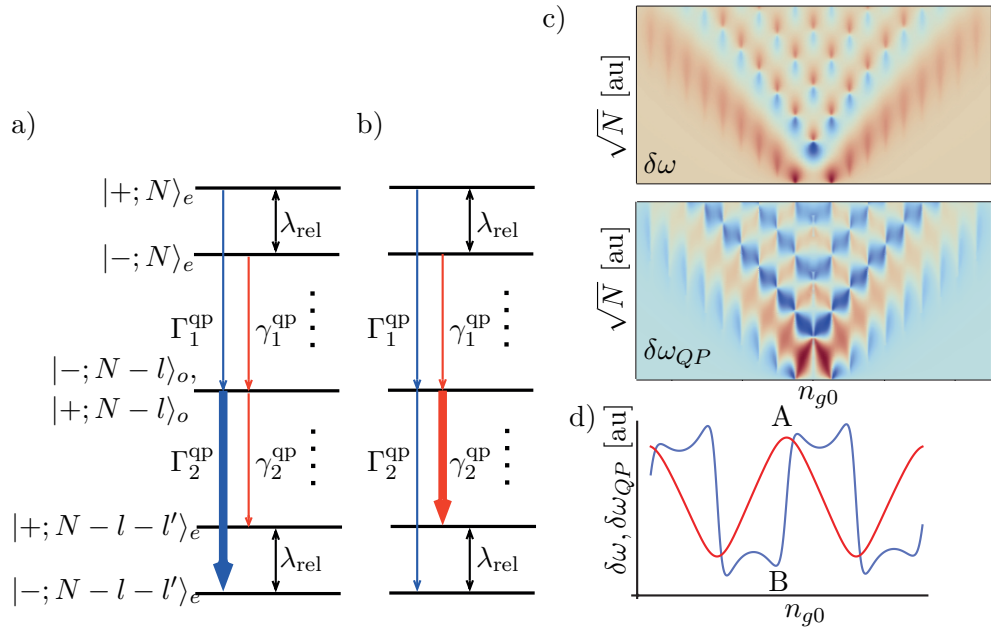
Figure 6.2: Quasiparticle relaxation process in the dressed state basis. The system evolves via the odd subspace back to the even parity. Depending on bias point around the dressed degeneracy the dominating relaxation rate will be that which brings the system to the nearest allowed charge state. a) and b) correspond to the points A and B in panel d) respectively. c) Frequency shift pattern obtained using eq. (5.30) (top) and eq. (6.4) (bottom). d) Comparison of the frequency response of the cavity for quasiparticle region (blue, eq. (6.4)) and the conventional LZS interference (red, eq. (5.30)).

the island, having an unpaired electron will result in an increased tunneling rate out from the island since tunneling another quasiparticle onto the island in this situation will cost a significant amount of charging energy. This we model by adding an assymmetry to the rate of the simplest form $\Gamma_{\text{odd}}(\delta E) = \Gamma^0_{\text{odd}} \Theta(\delta E)$. [149, 150]

The introduction of quasiparticle processes in the dressed state model reproduces the data very well at higher drive strengths (Fig. 5.7), and also for a wide range of tempertaures [Paper IV].

6.2 Population inversion and parity recovery

A very interesting outcome of the new regime of photon assisted tunneling is that it results in population inversion in the qubit basis. Such population inversion can for example be used to effectively prepare the qubit in a desired state before performing operations (at much lower drive strengths). This population inversion in the dressed state basis is illustrated in Fig. 6.2a-b. The population inversion arises as a result of an enforced parity change when the system is driven above 2Δ. This parity change is associated with a given transition in the charge basis. For example, if initially in the state $|-1e\rangle$ a pair breaking event can only bring the CPB to the state $|0e\rangle$, since a transition to $|2e\rangle$ would imply simultaneous Cooper-pair tunneling. Thus, at the (dressed) degeneracy points photon assisted pair-breaking results in a sharp transition in the qubit population; on one side of the dressed gap relaxation is to

the qubit state $|-\rangle$ (Fig. 6.2a) and on the other side to the state $|+\rangle$ (Fig. 6.2b), resulting in a cavity frequency shift as a function of the gate voltage as sketched in Fig. 6.2d.

The frequency response in the presence of quasiparticle tunneling has the following form

$$\delta\omega_{QP}(N, n_{g0}) = \sum_m \frac{4\beta|\delta E_C|}{\hbar\delta E_C\sqrt{N}}[\delta E_C - m\hbar\omega_0]\frac{E_J\Delta_m J'_m(4\beta\sqrt{N})}{2[\delta E_C - m\hbar\omega_0]^2 + \Delta_m^2}. \qquad (6.4)$$

This should be compared to eq. (5.30), and the population inversion appears naturally in the form of the additional factor $\delta E_C - m\hbar\omega_0$. This cavity frequency shift as a function of gate charge and drive strength is compared in Fig. 6.2c against the traditional frequency shift pattern given by eq. (5.30).

The dynamics in the discussed regime can be used to reset the qubit to a given parity. Thus, if the device is operated as a qubit at low drive strengths, and suddenly an unwanted quasiparticle changes its parity, instead of waiting for the parity to be recovered by itself a strong driving pulse can be used to reset the qubit to an operational state. Similarly, it can be used to study effects of quasiparticles on the island, or possibly as a single quasiparticle source.

6.3   Outlook: charge sensing with RF-readout

The results from the CPB experiments show a new interesting regime. The best charge sensitivity extracted from the data in Fig. 5.7a was 2.9 $\mu e/\sqrt{Hz}$, comparable to the sensitivity in SETs [151]. Not only does the measured data give a high charge sensitivity in the region where the dissipation channel from photon-assisted pair-breaking dominates, but this region also has several other advantages compared to other devices when it comes to charge sensing. One obvious side effect is that the interference pattern has perfect 1e-periodicity, i.e. it is unaffected by non-equilibrium quasiparticle tunneling. In Fig. 6.3 another advantage is illustrated. We see that the charge noise environment leads to typical relaxation and dephasing which determines the width of the interference features. Such relaxation have been studied in detail and it is well known that the charge noise environment limits the coherence times of CPBs [115, 136, 152]. In the case when only quasipartcle processes are included in the calculation (Fig. 6.3b) the result is a population inversion everywhere inside the region of LZS interference. In the actual device both these environments are combined, and they dominate in different regions of the interference pattern. At low drive strengths the ohmic environment dominates and the characteristic "droplet-shaped" interference features are observed, with the width defined by the relaxation rate (see eq. (5.17)). However, at stronger drives the photon-assisted pair-breaking process takes over and dominates. The "reset" mechanism via the odd subspace becomes faster than the decoherence rate, and a charge sensor operating in this region would therefore not be limited by decoherence in the same way as a conventional CPB, which increases the sensitivity. Theoretically, in the limit where the reset-rate is much faster than the decoherence rate, the sensitivity is now limited only by coupling (see derivation in [Paper IV]) and low frequency charge fluctuators.

$$\left.\frac{\partial\omega_{QP}}{\partial n_g}\right|_{\delta E_C = m\hbar\omega_0} = \frac{4\beta^2}{\hbar}\frac{J'_m(2\beta\sqrt{N})}{J_m(2\beta\sqrt{N})}. \qquad (6.5)$$

This expression assumes that there are no slow charge fluctuations present in the environment. During the relatively slow measurement timescale we do observe smearing on top of
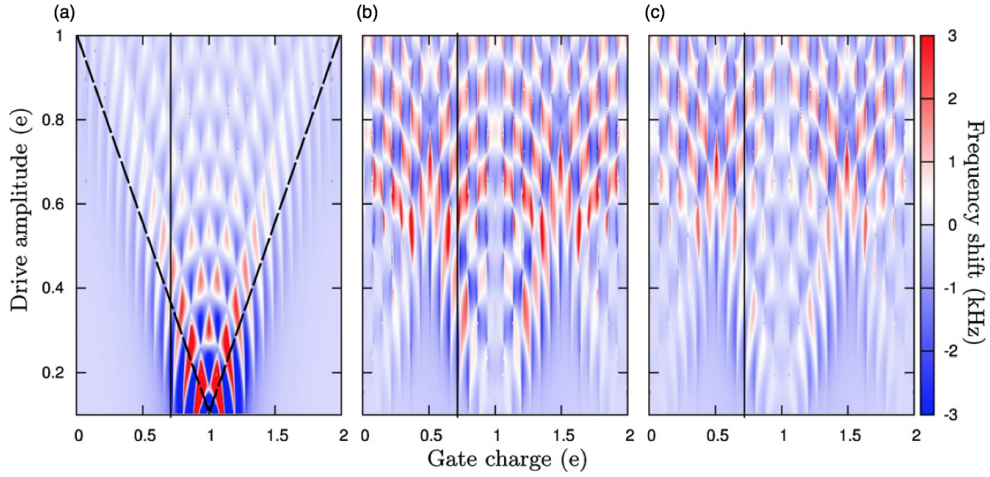
Figure 6.3: Numerical calculations using (a) only a charge noise environment and (b) only intra-parity transitions mediated by pair-breaking and (c) both combined as in the measured data.

eq. (6.4) which limits the sensitivity. However, the noise associated with the uncertainty of the photon number in the resonator, $\langle N \rangle^2 - \langle N^2 \rangle = \sqrt{N}$ becomes greatly suppressed in the quasiparticle-dominated regime since the frequency shift pattern is robust against fluctuations in N at the point of maximum charge sensitivity.

The scanning RF-qubit

We have seen that interrogation of qubits using NSMM in the strong driving regime can be very useful for qubit characterization. We may also consider placing the same CPB on the tip itself and operate it as a charge sensor. While the demonstrated regime may be more difficult to reproduce than a single electron transistor (SET) with a given sensitivity, it does have the advantage that it becomes much more robust. For example, a big problem with SETs on cantilevers [153] is that it is very easy to burn the device, both by electrostatic discharge and sending a too large source-drain current. This can for example happen if the tip comes in contact with the sample. As a single tunneling barrier device the CPB is galvanically isolated and more robust.

Single electron charge sensing can be performed using many different techniques, such as Kelvin probe microscopy (KPFM) [13], electrostatic force microscopy (EFM) [14], scanning-SET [12, 153, 154] and NV-centers in diamond [155]. They all reach beyond single electron sensitivity, however, they are greatly outperformed by the radio-frequency-SET (RF-SET) [156] since it operates above the limit of $1/f$ charge noise. In this sense, the NSMM probes developed during this thesis would allow for convenient integration of both RF-SET or a CPB with RF-readout directly on the cantilever. Additionally, a qubit near the tip could be used to measure decoherence induced by the sample under study much more accurately than by just monitoring the properties of the resonator. For this purpose other qubit types (such as Transmons [7]) with longer coherence times compared to the CPB are desired since the sensitivity to decoherence in the sample would be limited by the relaxation rate of the qubit on the tip.

In parallell with developing NSMM probes we have also developed a fabrication process
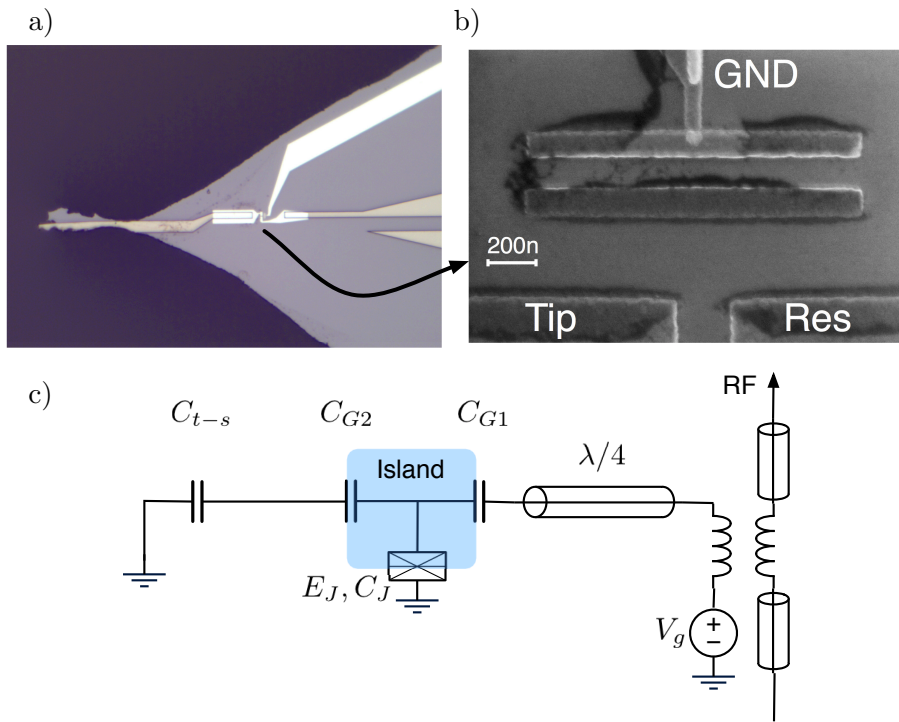
Figure 6.4: a) Optical image showing a NSMM probe with integrated CPB for charge sensing. b) SEM image of the CPB near the tip. c) Schematic of the setup.

that integrates Josephson junction technology into the probe fabrication. The details of this process are given in Appendix A and the process involves an additional lithography step that is made in parallel with the lithography used to define the shape of the probe (see Fig. 4.4). Not only could this be used for integration of charge sensors on the probe, but also to make a broadband resonant NSMM as discussed in Sec. 5.4.3. At the moment of writing this thesis there has not been an opportunity to mesure the final devices yet, but Fig. 6.4 shows one such a device. This design is made to mimic the device measured in [Papers III and IV], but with the additional probe connecting the tip and the CPB. Such design will suffer from reduced charge sensitivity due to the capacitive division between tip-sample and tip-CPB, but, if optimized, this reduction only constitutes a factor two.

7

INTERACTION WITH SPIN ENSEMBLES

In this chapter we explore the posibilities of coupling spin degrees of freedom to our super-conducting resonators. Apart from being able to study the physical properties of a very small (femto-mole) spin ensemble in an electron spin resonance (ESR) experiment. The possibility to manipulate spins in a small $(10^2 - 10^3)$ ensemble is especially attractive in the field of cirquit quantum electrodynamics. The exceptionally long coherence times of spin systems (the current record is a relaxation time T_2 of 39 minutes of Phosphorous donors in isotropically pure silicon [18]) makes them ideal to store quantum information. Another promising application utilize the wide range of available energy level spacings found in these systems to interface microwave and optical domains [157, 158]. New functionalities that can be found in many exotic chemically tailored molecular spin systems are also of great interest. This includes quantum computing using single molecule magnets (SMM) [19], and access to long spin coherence times using electric field manipulation [19, 67, 159] in ensembles of molecules. Two such molecular systems are discussed further at the end of this chapter. Before that we go through the basics behind the interaction between microwaves and spins and we specifically address the fractal design and the behavior of the PDH measurement which can be used as an efficient tool to quickly record an ESR spectrum of a very small sample. The results in this chapter are scattered in [Papers I and VI] and here some preliminary unpublished results are also discussed.

7.1 Spin ensembles coupled to microwave resonators

7.1.1 Zeeman effect

The concept of electron spin resonance relies on the magnetic moment of an unpaired electron in an applied magnetic field. The spin Hamiltonian is

$$H_{spin} = g\mu_B B_z \cdot \sigma_z, \tag{7.1}$$

where the constant g is the gyromagnetic ratio, or g-factor, and is a measure of the magnetic moment relative to the angular momentum vector of the particle. For a free electron this value is close to 2. $\mu_B = e\hbar/2m_e$ is the Bohr magneton and B_z the applied magnetic field. At zero field the two energy eigenvalues are degenerate but as soon as B_z is non-zero the spin-up and spin-down states will be separated in energy by the amount $g\mu_B B_z$ and this is called the Zeeman effect. A microwave photon of energy $\hbar\omega = g\mu_B B_z$ can be used to excite the spin, as shown in Fig. 7.1.
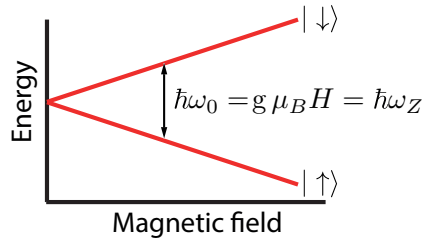
Figure 7.1: Energy level spectrum of a single spin 1/2 particle in applied magnetic field.

7.1.2 Collective coupling

The main advantage of coupling spin degrees of freedom to a superconducting resonator is the long coherence times of spin systems. However, the coupling of a single spin to the magnetic field in a cavity is much weaker than the electric dipole coupling of, for example, a charge qubit. For example, the coupling of a single spin in a typical ESR spectrometer is on the order of 0.1 Hz. Careful design in a one dimensional superconducting cavity can boost the coupling up to four orders of magnitude, however, this is typically still not enough to enter the strong coupling regime of a single spin. To achieve stronger coupling a large number of spins can instead be collectively coupled to the cavity. The Hamiltonian of an ensemble of spins reads

$$H = \hbar\omega a^\dagger a + \frac{\hbar}{2}\sum_n^N \omega_z \sigma_n^z + \sum_n^N \hbar\Gamma_n(\sigma_n^+ a + \sigma_n^- a^\dagger), \tag{7.2}$$

where the first term describes the cavity, the second the ensemble of N individual spins with $\hbar\omega_z = g\mu_B B_z$ and the last term the coupling with strength Γ_n. The photon field in the cavity couples to the raising and the lowering operators of each individual spin. The effective coupling of the ensemble can be written

$$\Gamma_{\text{tot}} = \sqrt{\sum_n^N |\Gamma_n|^2}. \tag{7.3}$$

For the simplified case when all spins are equally coupled it reduces to

$$\Gamma_{\text{tot}} = \Gamma_0\sqrt{N}. \tag{7.4}$$

Thus, if we have a sufficiently large number of spins it is possible to reach a strong coupling regime, a requirement for quantum computation. This collective coherent coupling of a large spin ensemble to a superonducting resonator was at the same time demonstrated in 2010 by two groups in nitrogen vacancies in diamond [160] and in ruby [161]. And the experiment was shortly after repeated in several other systems [157, 162, 163]. Coherent exchange of information between a qubit and a spin ensemble was also demonstrated shortly after [140, 164].

7.1.3 Broadening

The linewidth of the interacting spin system is intrinsically defined by the relaxation time of the spins, however several factors can contribute to a wider linewidth. If the resonator itself
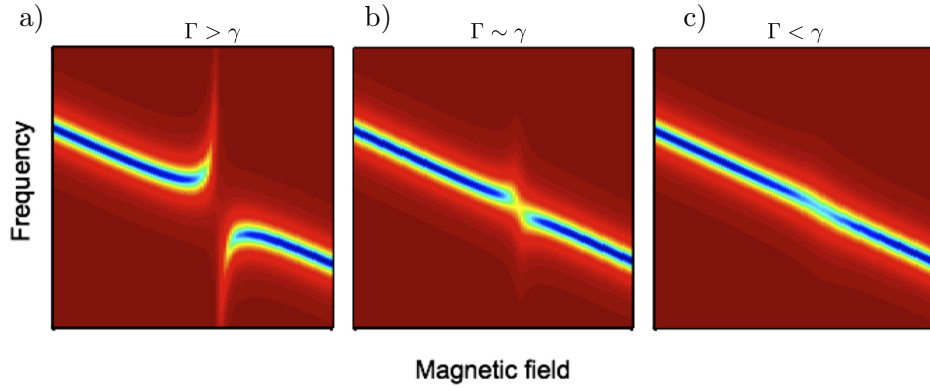
Figure 7.2: Expected response in transmission amplitude (color scale) of a quarter wave cavity in a magnetic field where the Zeeman splitting for a spin ensemble, of linewidth γ, crosses the frequency of the resonator. Panels show the response as the coupling goes from the strong coupling regime to the weak coupling regime. In all cases $Q < \gamma$.

disrupts the applied magnetic field (Meissner effect) too much magnetic field inhomogeneities will result in different parts of the spin ensemble experiencing different magnetic fields. This effectively reduces the number of spins contributing to the ESR signal at a given magnetic field. From preliminary measurements on crystals of Y_2SiO_5 doped with Nd^{3+} ions (Nd^{3+}:Y_2SiO_5) we have observed linewidths down to 3 MHz (0.1 mT), this is a very low number suggesting that the static magnetic fields are in fact very homogeneous in the fractal geometry, which is also expected from the low flux focusing factor.

Another reason for broadening can be significant dipole-dipole interaction or strong exchange interaction, i.e. the spins are situated too close to each other, resulting in energy incoherently leaking to other parts of the ensemble. The effect of these types of broadening is considered in detail in Refs. [163, 165].

In experiments we measure the response of the resonator, and in order to have a detectable response the coupling has to be strong enough. We can define three different regimes as shown in Fig. 7.2. In panel a) the coupling g is larger than the linewidth of the spin ensemble γ and near the resonance condition the system can be described by two strongly coupled oscillators, and a splitting of the resonance modes is obtained. For larger γ the splitting eventually dissapears but a frequency shift and increased dissipation in the cavity can still be detected, and finally, in Fig. 7.2c, the frequency shift becomes negligible but an increased dissipation is still observed. In general the linewidth of the resonator is also contributing to the broadening of the coupled system; however, in most experiments presented here the resonance linewidth is much smaller than the linewidth of the spin ensemble and can therefore be neglected. The following expression for a cavity coupled to an ensemble of spins can be derived [161]

$$S(\omega) = 1 + \frac{\omega_0/Q_c}{i(\omega - \omega_0) - \omega_0/Q + \frac{|\Gamma|^2}{i(\omega-\omega_z)-\gamma/2}}, \qquad (7.5)$$

where $\hbar\omega_z = g\mu_B B$. This assumes that we are far away from saturating the spin system, i.e. $N_{\text{photon}} \ll N_{\text{spin}} \times (2\pi T_1/\omega_0)$ where T_1 is the energy relaxation time of the spins.
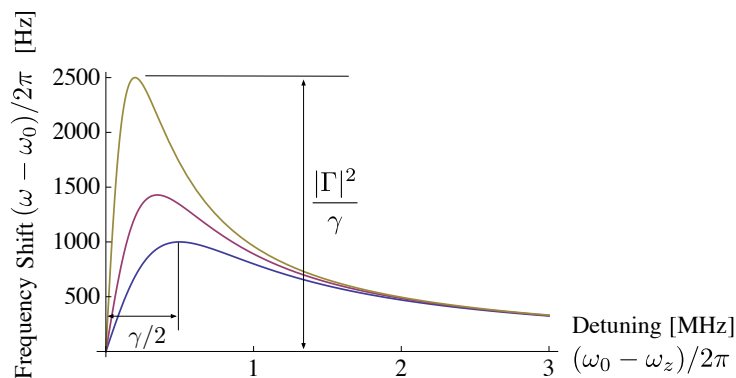
Figure 7.3: Frequency deviation detected by the PDH loop as the system is adiabatically swept through an avoided crossing in the limit of weak coupling. The three curves are for different values for the linewidth of the spin, $\gamma = 10^6, 7 \cdot 10^5$ and $4 \cdot 10^5$. $|\Gamma|^2 = 10^9$ in all three cases and $Q_c = 2Q = 10^5$.

7.1.4 PDH readout

In a PDH measurement of a resonator swept across the resonance with a spin ensemble the PDH loop will track the initial resonance branch across the splitting, until at some point it becomes unfavorable to stay on this branch of the split resonance (the error signal acquires a saddle point at the point where it is locked). The PDH loop will then remain unstable for some time until it becomes favorable to switch to the second branch in the avoided crossing (see Fig. 7.2a) and the q-PDH signal will in this region drop to zero. Eventually the PDH loop will switch to the second resonance branch at a speed which is determined by the bandwidth of the loop.

In the weakly coupled limit we instead expect to see a symmetric and smooth response of the resonance frequency around the exact crossing frequency. In the weak coupling regime ($\Gamma \ll \gamma$) the maximum frequency shift scales as

$$\delta\omega_{\max} = \frac{|\Gamma|^2}{\gamma}, \tag{7.6}$$

and will be observed at a distance $\gamma/2$ away from the exact point of crossing. This is the regime we observed in the measurements presented in the following sections.

7.2 Estimating the single spin magnetic coupling in the fractal geometry

We now aim to derive a value for g_n in eq. (7.2). In practical situations this becomes difficult to evaluate for a large ensemble experiencing a large variation in spatial coupling. In the fractal geometry the dimension of the conducting lines in the resonator become comparable in size to the spin systems that we want to couple to and in this case each individual spin would experience a very different microwave magnetic field, and thus different coupling. We therefore resort to modeling the spin system using a spin density distribution $\rho_N(V_{\text{spin}})$ and a magnetic field distribution $H(V_{\text{spin}})$ which we evaluate over the whole volume of interest.
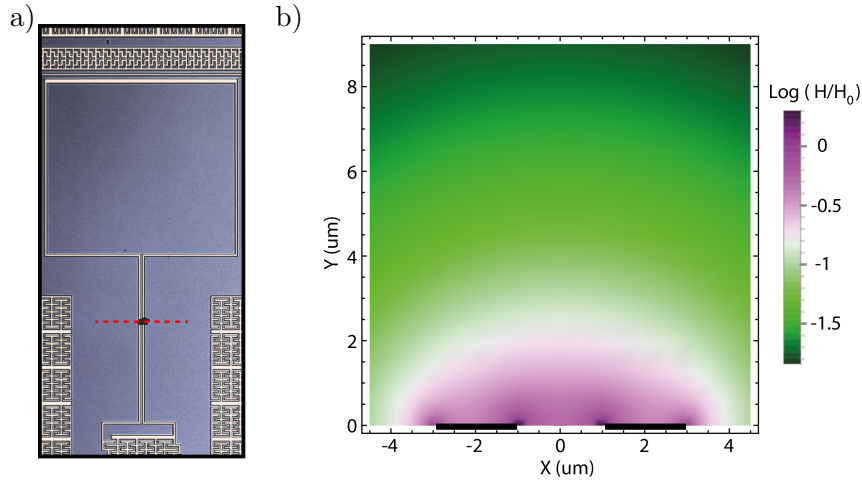
Figure 7.4: a) Photo of a Fractal resonator near its current maximum. Red dashed line shows location of the cross section in b). b) Numerical evaluation of $H(\xi)/H_0$, showing the localized volume of the coupling. The field strength drops an order of magnitude on the length scale of the strip (black solid line) width.

First we consider the magnetic field density in the two parallel strips carrying a current I_0 in opposite $(+z, -z)$ directions. Using a somewhat simplified expression [48] as compared to the NBI model [46], we have

$$H(\xi) = -H_0 \frac{W^2}{\sqrt{\xi^2 - b^2}\sqrt{\xi^2 - W^2}}, \tag{7.7}$$

where we have used the parametrization $H(x,y) = H(x+iy) = H(\xi)$. $W = b+a$ and a is the strip width and $2b$ the spacing between the strips. We assume that there is no z-component of the magnetic field and the quantity that will be used to evaluate the coupling is the total contribution from the fields perpendicular to the current flow: $H_g(x,y) = \sqrt{H_x^2 + H_y^2} = |H(\xi)|$. We have now to determine the constant H_0, which is the magnetic field intensity at $\xi = 0$ when the resonator is populated by a single photon. We start by evaluating the current density resulting from this magnetic field profile

$$J_z(x) = -H_0 \frac{2x}{d|x|} \frac{W^2}{\sqrt{W^2 - x^2}\sqrt{x^2 - b^2}}, \tag{7.8}$$

where d is the film thickness, and we have assumed that the current density is uniform along the y-coordinate (the thickness of the film). To find the total current I_0 we then integrate the current density along the strip, which gives the relation for H_0 in terms of I_0:

$$H_0 = \frac{\mu_0 I_0}{2WK(\sqrt{1 - b^2/W^2})}, \tag{7.9}$$

where $I_0 = \sqrt{\hbar\omega/2L}$ is the current due to a single photon. We can now evaluate the average contribution to coupling from an ensemble of N spins as related to the coupling that we can evaluate at one specific point. For simplicity we choose the point $x = 0$, $y = 0$.

$$\Gamma_{\text{tot}} = \Gamma_0 \sqrt{\int_{V_{\text{spin}}} \rho_N(V_{\text{spin}}) \left(\frac{|H(\xi)|}{|H_0|}\right)^2 dV}, \tag{7.10}$$
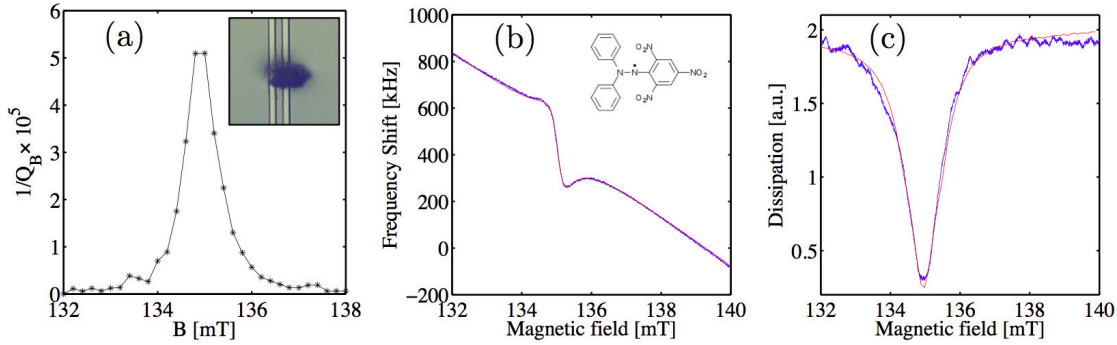
Figure 7.5: a) Spin induced cavity loss rate measured using VNA of a small flake of DPPH (sample A) on top of the main current carrying conductors of the resonator (inset). Lines are 2 μm wide. b) and c) PDH measurement on the same sample. Numerical calculations (red) is fitted to experimental data (blue). Including a parabolic frequency shift and the asymmetry in lineshape of the cavity (measured with VNA) the numerical calculations fit the data remarkably well. $T = 1.7$ K. Extracted parameters are $\gamma/2\pi = 15$ MHz, $\Gamma/2\pi = 1.5$ MHz.

and g_0 becomes

$$\Gamma_0 = \frac{\mu_B}{2\pi\hbar}|H_0| = \frac{\mu_B \mu_0}{2\pi\hbar} \frac{\sqrt{\hbar\omega/2L}}{WK(\sqrt{1 - b^2/W^2})} \approx 2\pi \cdot 75 \text{ Hz}. \qquad (7.11)$$

At finite temperatures not all spins will contribute to the total coupling since a fraction of them will be thermally excited. This fraction depends both on temperature and the Zeeman splitting and can be derived from the Fermi distribution

$$\Gamma_{\text{tot}}(T) = \Gamma_{\text{tot}}(T = 0)\sqrt{\tanh \frac{g\mu_B H}{2k_B T}}. \qquad (7.12)$$

For $T = 1.7$ K, $g = 2$ and $H = 0.2$ T this gives $\Gamma_{\text{tot}}(T)/\Gamma_{\text{tot}} = 20\%$ while at 300 mK the polarization is increased to 50%.

7.3   ESR measurements on femto-mole DPPH ensembles

Fig. 7.5 shows the response of a microwave resonator on which we placed a micron sized flake of DPPH. Panel (a) is measured using VNA. PDH measurements on the same sample (panels b and c) agrees perfectly with the theoretical model, eq. (7.5) with added assymmetry to the resonance lineshape (extracted from VNA measurement) and the expected response from the q-PDH loop. We extract the parameters $\gamma/2\pi = 15$ MHz, $\Gamma/2\pi = 1.5$ MHz, resulting in $N = (\Gamma/\Gamma_0)^2 \sim 3.9 \cdot 10^8$ spins if we asume a single spin coupling $\Gamma_0/2\pi = 75$ Hz. At $T = 1.7$ K only 15% of the spins are polarized, such that the total number of molecules in the flake is on the order of $3 \cdot 10^9$. This is in good agreement with the density and size of the flake also considering the participation ratio of $\sim 25\%$ per spin that is obtained by integrating the coupling over the observed volume of the flake (eq. (7.10)). The SNR in Fig. 7.5 is evaluated from the rms noise and using the time constant of the lockin used in the
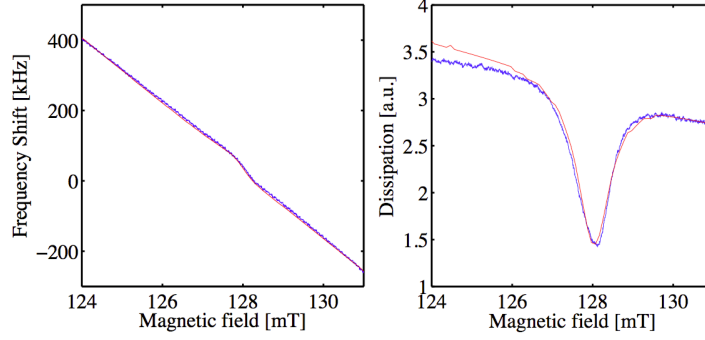
Figure 7.6: PDH measurement on DPPH sample B. Numerical calculations (red) and experimental data (blue). $T = 1.7$ K. Extracted parameters are $\gamma/2\pi = 22$ MHz, $\Gamma/2\pi = 0.6$ MHz.

experiment we arrive at a spin sensitivity of $5 \cdot 10^5$ spins/$\sqrt{\text{Hz}}$. Measurements on a second sample with a weaker collective coupling is shown in Fig. 7.6. The obtained sensitivity is very consistent with the previous sample despite the large difference in coupling strength.

The main outcome from these measurements is that we are able to measure the spin from a femto-mole of molecules by using the q-PDH technique. The strong coupling regime needed for quantum computing could be reached at lower temperatures and with a slight increase of the size of the DPPH flake.

7.4 Outlook

7.4.1 Single spin ESR

Standard X-Band ESR spectrometers typically have a spin sensitivity of $\sim 10^9$ spins/$\sqrt{\text{Hz}}$ [64]. State of the art experiments reach down to $\sim 10^6$ spins/$\sqrt{\text{Hz}}$ [166, 167] and using qubit readout down to $\sim 10^5$ spins/$\sqrt{\text{Hz}}$ [168]. In [Paper VI] we demonstrate a sensitivity, based on the dissipation measurement, of $\sim 5 \cdot 10^5$ spins/$\sqrt{\text{Hz}}$ using a Nb fractal resonator and q-PDH readout at 1.7 K. This low number is partly thanks to the readout technique but also due to the high quality factor (~ 50000) and strong coupling of spins in a planar resonator. This could be improved further, mainly by locally reducing the with of the current carrying lines in the fractal resonator. Measurements show that nanowires with dimensions of $W = 200 + 100$ nm can be implemented while maintaining quality factors above 10^5, thus boosing the single spin coupling ~ 10 times. In terms of the cavity frequency shift $\propto \Gamma_0^2/\gamma$ this could reduce the minimum number of detectable spins up to two orders of magnitude. The higher Q in our NbN resonators at 300 mK amounts for another order of magnitude improvement, and a spin system with a linewidth of 3 MHz, as we have seen in measurements on Nd^{3+}:Y_2SiO_5, compared to the linewidth in DPPH of $\gamma/2\pi = 15$ MHz could improve this ESR technique down to $\sim 10^1$ spins/$\sqrt{\text{Hz}}$. This is however, not completely true since we at this point would be limited by the amplifier used to detect the microwave response (to read out such a small number of spins we also need to have a smal number of photons in the cavity to avoid saturation). Thus, while the demonstrated technique is promising for single spin ESR it must somehow also be integrated with a quantum limited parametric amplifier to reach the limit of single spin detection per unit of bandwidth.
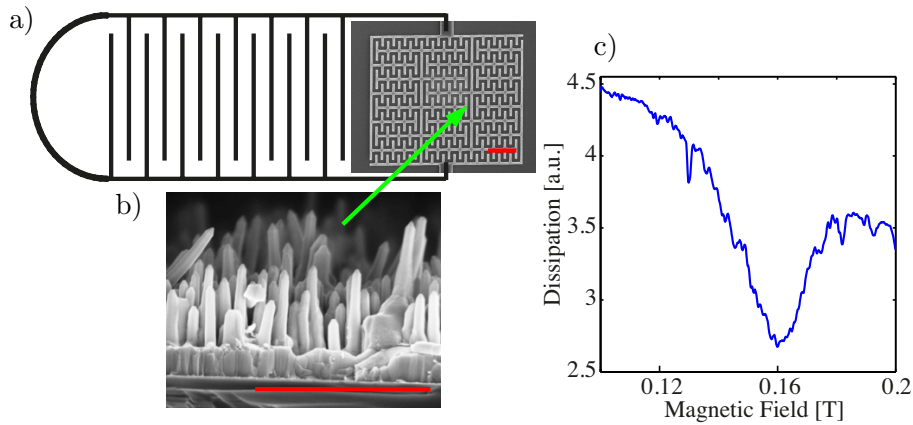
Figure 7.7: a) Layout of the resonator loaded with a dense capacitor to enhance electric field strength. b) SEM image of the Mn:ZnO sample placed on top. Image courtesy of V. Khranovskyy, Linköping University. Scale bars are 2μm. b) Measured ESR signal.

7.4.2 Electrically tuned spin ensembles

A special class of new spin-active materials show promising properties for both large scale quantum memories as well as novel functionalities in quantum circuits. These have in common that the spin degree of freedom couples to electric fields as well as magnetic fields. Physically this could be the result of many different mechanisms, such as strong spin-orbit coupling in semiconductor nanowires [68], piezoelectric coupling [67], or various mechanisms in molecular metal complexes [66, 169]. For static electric tuning in some of these systems it calls for strong electric fields, close to atomic scale fields [169], i.e. 0.1-1 V/nm, which we can develope in the split fractal resonators demonstrated in [Paper V], and is one of the reasons we developed these resonators. Here we will discuss two different electrically tuneable spin systems that we have started to explore.

The coupling to electric field in all these systems also brings us back to the NSMM microscope, which could be used to locally study these materials. For example, one problem we often encountered is that the samples delivered has an unknown crystalline direction and sometimes an amorphous structure within larger flakes or pieces. Due to the anisotropy of the Hamiltonian in these materials this makes experiments unpredictable, but using an NSMM to study these small samples we could map out their crystal axis by the electric field ESR response.

Doped piezoceramics (ZnO nanowires)

The first compound we have started to explore is ZnO nanowires with Mn^{2+} substituted for some Zn^{2+} ions in the ZnO lattice (ZnO:Mn). The electric field response was recently characterized in bulk [67], demonstrating electrically induced spin transitions and very long coherence times. The origin of this electric field dependence comes from the piezoelectricity of ZnO, which can be used to modify the crystalline field experienced by the Mn defects, and this crystalline field directly influences the zero-field splitting (ZFS) of the spins. The Hamiltonian of the ZnO:Mn system is [67]

$$H = \mu_B \mathbf{g} \cdot \mathbf{S} \cdot \mathbf{B} + g_N \mu_N \mathbf{I} \cdot \mathbf{B} + \mathbf{S} \cdot \mathbf{A} \cdot \mathbf{I} - DS_z^2 \qquad (7.13)$$
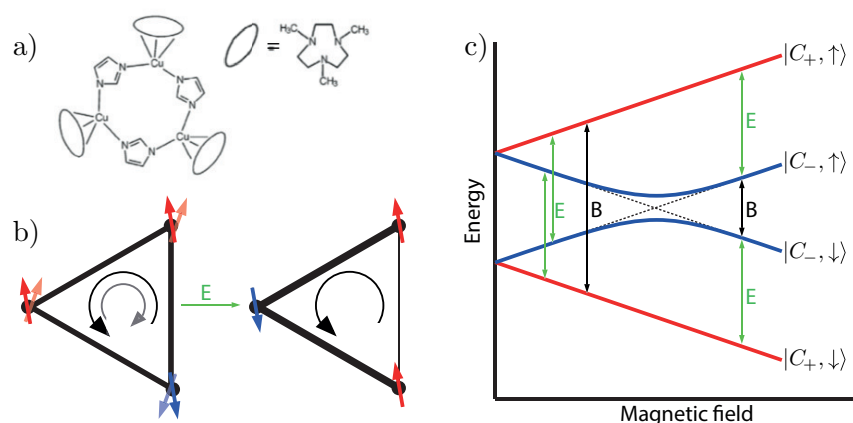
Figure 7.8: a) Chemical structure of the spin triangle. b) Sketch showing the effect of applying an in-plane electric field. The degeneracy of the chirality is lifted as a result of a reduced exchange interaction between two Cu pairs. Spin degeneracy is lifted by the conventional Zeeman term in the Hamiltonian. c) Energy level spectrum for an applied magnetic field. Arrows show allowed transitions for electric field (green) and magnetic field (black).

where $D = D_0 + \kappa E$ is the zero field splitting that also contains a term proportional to applied electric field E, which could be either DC or microwave. The other terms are in order from left to right, the Zeeman term, nuclear Zeeman term, and the hyperfine interaction.

Our first attempts were made on a fractal resonator with a very dense capacitor at the voltage maximum (see Fig. 7.7a) used to increase electric fields and further reduce currents and magnetic coupling. The ZnO:Mn nanowires grown on Si (Fig. 7.7b) were placed directly on top in a flip-chip geometry and the response measured at 1.7 K is shown in Fig. 7.7c. We see a very strong dissipation signal, even though only a small number ($10^8 - 10^9$) of polarized spins are present. However, the response is very broad and no individual resonances in the otherwise rich ESR spectrum [67] is seen, a result of angular anisotropy and coupling to a large number of nanowires of different orientation. Future experiments involve only a single nanowire coupled to the resonator, as well as interrogation using static electric fields.

Frustrated spin triangles

Single molecule magnets (SMMs) are another promising class of materials for quantum computation and specifically chemically engineered frustrated spin SMMs [66]. Here we consider the simplest of such systems, "spin triangles", consisting of three spin sites antiferromagnetic exchange coupling and spin-orbit coupling in a triangluar fashion (see Fig. 7.8a and b). There exists no trivial way of aligning the spins in such a system; the first two spins may pair together, one spin being "up" and the other "down", however, the third spin couples equally to the other two spins and an excess energy is associated with it. The spin triangle is said to be frustrated, and the spins attain an off-axial orientation in zero magnetic field to relax the frustration. This results in eigenstates described by two quantum numbers $|C; \uparrow \downarrow \rangle$, where $\uparrow \downarrow$ signifies wether the total spin is up or down ($\pm 1/2$) and $C = \pm 1$ is the chirality of the three frustrated spins, i.e. wether the frustrated spins relax in a clockwise or counterclockwise orientation. In the absence of zero-field splitting all these four states are

degenerate and they are all lifted by the Zeeman splitting, producing two degenerate pairs $|\pm 1;\uparrow\rangle$ and $|\pm 1;\downarrow\rangle$. However, in the prescece of zero-field coupling the degeneracy of the chirality is lifted and this results in four different energy bands as shown in Fig. 7.8b. As a result of strong spin-orbit coupling and selection rules, microwave magnetic field can induce transitions between spin states, conserving chirality, while microwave electric fields can be used to induce transitions within the same spin state with different chirality. For a single molecule coupled to a cavity the following Hamiltonian was derived in the case of purely electric coupling [66]

$$H = \hbar\omega a^\dagger a + DC_z S_z + g \cdot \mathbf{B} \cdot \mathbf{S} + \kappa E_0 [e^{i\varphi} C_- + e^{-i\varphi} C_+](a + a^\dagger) + \kappa \mathbf{E}_{DC} \cdot \mathbf{C}. \qquad (7.14)$$

The terms are: Cavity Hamiltonian, ZFS, Zeeman interaction, coupling between cavity and chirality and the coupling to static electric fields. E_0 is the electric field due to a single photon and κ the dipole coupling of the molecule. $C_{+(-)}$ is the raising (lowering) chirality operator and φ depends on the projection of the applied electric field onto the crystal axis. For magnetic coupling we instead have the standard form of the Hamiltonian in eq. (7.2).

Initial measurements on the molecules shown in Fig. 7.8a did not reveal any coupling to either static or microwave electric fields, we only observed a magnetic resonance consistent with a free spin system ($g = 2$). Measurements in static electric fields using the split fractal resonators did not reveal any shift in ESR resonance either, within experimental resolution of 0.01 mT. Recent theoretical analysis of the exact molecule shown in Fig. 7.8a suggests that the Jahn-Teller effect exceeds the spin-spin coupling which relaxes the frustration [170]. Further chemical engineering is therefore needed to reduce this Jahn-Teller distortion.

7.4.3 Technologies for spins coupled to superconducting resonators

The first approaches to coupling spins to microwave cavities all have in common that a large crystal, on the order of several mm, are placed directly on top of the cavity [160–162]. While it is possible to achieve very good control over dopants and uniformity in these crystals, their size pose a problem for large scale integration. The results demonstrated in this thesis shows that it in principle is possible to achieve good coupling to a much smaller spin ensemble, which also could have added functionality by chemical design. However, larger crystals can still be very useful, not only in fundamental studies of various spin systems, but they may also become important towards the integration of quantum optics on chip, and to achieve interfaces between superconducting circuits used for computation, and the optical domain used for communication [171].

However, other directions could be promising for several other applications. The chemically engineered spin ensembles presented in the previous section could be used for quantum information storage but the added functionality also provides for possible computation [65] in similar systems. Such chemically derived systems are also compatible with a wide range of different fabrication technologies. In our attempts on small ensembles we have so far been restricted to micromanipulation to place the ensembles in the right place, however, more advanced techniques such as self-assembly or ink-jet printing could be used to make large-scale circuits out of these materials.

Another interesting direction that instead integrates well with modern semiconductor processing techniques is local ion implantation. This technique retains the properties found in the large doped crystals but instead spins can be locally implanted into the substrates on which the superconducting resonators are built. This could yield a large number of

individual ensembles with long coherence times coupled to the same cavity, a technique suitable for dense quantum information storage.

How useful all of these different proposed technologies will be in future devices remains to be seen and significant experimental effort is needed to explore all these materials in superconducting circuits. Many of the techniques presented in this thesis can hopefully be of use in this endeavour.

8
ACKNOWLEDGEMENTS

A

DEVICE FABRICATION

Standard Nb/NbN deposition and patterning on Si or Sapphire

- Clean wafers in hot 1165 for 5 minutes, Rinse in IPA and water.

- Si sibstrates: Dip in 2% HF buffer bath to remove native oxide for 30 seconds. Rinse in water and blow dry.

- Immediately load in Nb sputtering system.

- Si substrates: Anneal at 700°C for 20 min.

- Nb deposition: deposit desired thickness using substrate cooling.

- NbN deposition: deposit desired thickness without substrate cooling.

- Lithography of Nb/NbN

  - Spin UV5 0.8 at 3000-5000 rpm depending on Nb/NbN film thickness.
  - Bake at 130°C on hotplate for 120 seconds.
  - Expose using 35nA, 23 μC/cm^2.
  - Post bake for 90 seconds, 130°C.
  - Develope in MF-24A for 40 seconds, rinse in water.

- Etch Nb in plasma (404) using NF$_3$ gas. Use laser interferometer and end-point detection and over etch 10 seconds. Total etching time should be around 1:30 for 200 nm Nb/NbN.

- Run str02m_b in batchtop.

- Clean resist by putting the wafer in Remover (1165) for at least 12 hours. Rinse in IPA.

- Run recepie Ash7 in batchtop. Inspect for resist residuals and repeat if necessary.

Micromachined NSMM resonators

- Perform the standard Nb deposition and patterning on a Si wafer.

- Evaporate 150 nm Aluminium on all of the wafer.

- Dicing

- – Spin S1813 at 3000 rpm

- – Bake at 130°C for 2 min

- – Dice

- – Put in 1165 remover heated to 60°C for 5 minutes. Rinse in IPA.

- Thin down chips to around 50μm.

  - – Make sure the chips are clean on the backside. If not 'ash' for 5 minutes on the backside of the chips to remove any resist residuals on the edges.

  - – Mount with backside facing up on carrier wafer for silicon etching using 120°C thermal release tape.

  - – Run process SI_sfast (in degraaf folder) for 260-290 cycles. The more the better but after 290 cycles the chips are very thin and difficult to handle. Carefully note how many cycles have been etched on each chip.

  - – Carefully release the chips by putting the carrier on a hotplate set to 125°C.

  - – Remove the aluminium in MF 319. Let the chips stay a few minutes more after all Al is gone visually. Rinse in water and then IPA. Inspect cleanliness in microscope. If there are particles left from dicing, gently sonicate the chips for 1-2min (max 30% power) in IPA.

- Back side photolithography through IR alignment

  - – Spin S1813 at 2500 rpm on the backside of the wafer. Carefully scratch away resist buildup in the corners before baking. Any extra thickness of resist on corners will worsen the alignment of the etch mask. Make sure front side is still clean.

  - – Bake at 110°C on hotplate for 2 minutes.

  - – Expose with photolithography for 10 seconds using IR alignment.

  - – Develop in MF-319 for 40 seconds, rinse in water.

- Lithography to define Charge devices (optional, skip these steps for regular NSMM probes)

  - – Spin Copolymer EL10 at 4000 rpm.

  - – Bake at 170°C on hotplate for 5 minutes.

  - – Spin Zep520A 1:1 in anisole at 3000 rpm.

  - – Bake at 170°C on hotplate for 5 minutes.

  - – Expose.

  - – Develop top layer in o-xylene for 30 seconds, rinse in IPA.

  - – Develop bottom layer in IPA:H_2O (93% :7%) for 6 minutes 30 seconds, rinse in IPA.

- Etch through the Si wafer

  - – Carefully mount on carrier for silicon etching (upside down).

– Run process SI_sfast for another 60-30 cycles such that the total number of cycles from the previous etching becomes 320. Then continue stepwise with 5 cycles each time until completely through the wafer. Larger areas will come through first. Pay attention to the gaps on the sides of the resonator probes.

– Carefully release the wafer at 125°C on a hotplate.

- Evaoprate Charge devices (optional, skip these steps for regular NSMM probes)

    – Ash 10 seconds.

    – Evaporate Al by two-angle deposition in Plassys: 35/50 nm ±20°. Oxidation: 30 min 0.2 mbar.

- Resist removal/Lift-off: Put wafer in acetone for 12 hours using vertical holder.

CPB on sapphire fabrication

- Perform the standard Nb deposition and patterning on a Si wafer.

- Spin Copolymer EL10 at 4000 rpm.

- Bake at 170°C on hotplate for 5 minutes.

- Spin Zep520A 1:1 in anisole at 3000 rpm.

- Bake at 170°C on hotplate for 5 minutes.

- Evaoprate 25 nm Al in Plassys as a conducting layer.

- Expose.

- Remove Al in MF319 for 2 minutes.

- Develop top layer in o-xylene for 30 seconds, rinse in IPA.

- Develop bottom layer in IPA:H_2O (93% :7%) for 6 minutes 30 seconds, rinse in IPA.

- Evaporate Al by two-angle deposition in Plassys: 35/50 nm. Oxidation: 30 min 0.2 mbar.

- Lift-off in acetone for 12 hours.

Dielectric contrast sample

- Spin UV5 0.8 at 5000 rpm on an unoxidized Si wafer.

- Bake at 130°C for 90 seconds.

- Expose trench pattern using electron beam lithography.

- Develop in MF24A for 40 seconds.

- Etch 25 nm deep trenches using Cl plasma in tool 404. Etch rate is roughly 45 nm/min. Verify depth using profilometry.

- Remove the resist in Acetone.

- Sputter 500 nm SiO$_2$.

- Polish the SiO$_2$ down to 100 nm and verify the thickness using ellipsometry.

B
DERIVATION OF Q-PDH RESPONSE

Here the full derivation of the q-PDH error signal and Q signal discussed in Chapter 3 is derived. Starting from the doubly-modulated spectrum

$$E = E_0 e^{i\omega t + \beta i \sin \Omega_1 t + \alpha i \sin \Omega_2 t}, \tag{B.1}$$

we sexpand the two modulation-parts individually

$$E = E_0 e^{i\omega t} \sum_{n=-\infty}^{\infty} J_n(\beta) e^{in\Omega_1 t} \sum_{n=-\infty}^{\infty} J_n(\alpha) e^{in\Omega_2 t}. \tag{B.2}$$

And to first order we have

$$E \approx E_0 e^{i\omega t} \left[J_0(\beta) + J_1(\beta) e^{i\Omega_1 t} - J_1(\beta) e^{-i\Omega_1 t} \right] \left[J_0(\alpha) + J_1(\alpha) e^{i\Omega_2 t} - J_1(\alpha) e^{-i\Omega_2 t} \right]$$

$$E \approx E_0 e^{i\omega t} \left[J_0(\beta) J_0(\alpha) + J_1(\beta) J_0(\alpha) \left(e^{i\Omega_1 t} - e^{-i\Omega_1 t} \right) + J_0(\beta) J_1(\alpha) \left(e^{i\Omega_2 t} - e^{-i\Omega_2 t} \right) \right.$$
$$\left. + J_1(\alpha) J_1(\beta) \left(e^{i(\Omega_1+\Omega_2)t} - e^{i(\Omega_1-\Omega_2)t} - e^{-i(\Omega_1-\Omega_2)t} + e^{-i(\Omega_1+\Omega_2)t} \right) \right], \tag{B.3}$$

such that the output from the diode detector will be

$$P/P_0 \approx \left[J_0(\beta) J_0(\alpha) S_\omega + J_1(\beta) J_0(\alpha) \left(S_{\omega+\Omega_1} e^{i\Omega_1 t} - S_{\omega-\Omega_1} e^{-i\Omega_1 t} \right) \right.$$
$$+ J_0(\beta) J_1(\alpha) \left(S_{\omega+\Omega_2} e^{i\Omega_2 t} - S_{\omega-\Omega_2} e^{-i\Omega_2 t} \right)$$
$$+ J_1(\alpha) J_1(\beta) \left(S_{\omega+\Omega_1+\Omega_2} e^{i(\Omega_1+\Omega_2)t} - S_{\omega+\Omega_1-\Omega_2} e^{i(\Omega_1-\Omega_2)t} \right.$$
$$\left. \left. - S_{\omega-\Omega_1+\Omega_2} e^{-i(\Omega_1-\Omega_2)t} + S_{\omega-\Omega_1-\Omega_2} e^{-i(\Omega_1+\Omega_2)t} \right) \right]$$
$$\times \left[J_0(\beta) J_0(\alpha) S_\omega^* + J_1(\beta) J_0(\alpha) \left(S_{\omega+\Omega_1}^* e^{-i\Omega_1 t} - S_{\omega-\Omega_1}^* e^{i\Omega_1 t} \right) \right. \tag{B.4}$$
$$+ J_0(\beta) J_1(\alpha) \left(S_{\omega+\Omega_2}^* e^{-i\Omega_2 t} - S_{\omega-\Omega_2}^* e^{i\Omega_2 t} \right)$$
$$+ J_1(\alpha) J_1(\beta) \left(S_{\omega+\Omega_1+\Omega_2}^* e^{-i(\Omega_1+\Omega_2)t} - S_{\omega+\Omega_1-\Omega_2}^* e^{-i(\Omega_1-\Omega_2)t} \right.$$
$$\left. \left. - S_{\omega-\Omega_1+\Omega_2}^* e^{i(\Omega_1-\Omega_2)t} + S_{\omega-\Omega_1-\Omega_2}^* e^{i(\Omega_1+\Omega_2)t} \right) \right] + F[\omega \pm \Omega_1 \pm \Omega_2].$$

Here we use the notation $S_\omega = S_{21}(\omega)$. The terms resulting in a Ω_1-component (the MHz PM spectrum) results in the new error signal

$$
\begin{aligned}
\varepsilon \quad \approx \quad & J_0(\beta)J_1(\beta)J_0(\alpha)^2 \mathrm{Im}\left[\mathrm{S}(\omega)\mathrm{S}^*(\omega+\Omega) - \mathrm{S}^*(\omega)\mathrm{S}(\omega-\Omega)\right]\cos(\Delta\phi) \\
& + G[\omega \pm \Omega_1] + F[\omega \pm \Omega_1 \pm \Omega_2]
\end{aligned}
\tag{B.5}
$$

$$
\varepsilon \quad \approx \quad J_0(\alpha)^2\varepsilon_0 + G[\omega \pm \Omega_1] + F[\omega \pm \Omega_1 \pm \Omega_2].
\tag{B.6}
$$

Q signal

Lets now consider the terms in eq. (B.4) that has the exponents $e^{\pm i\Omega_1 t \pm i\Omega_2 t}$. After the first demodulation of Ω_1 this term will contain the FM frequency used to measure the dissipation.

$$
\begin{aligned}
P \quad \approx \quad & J_0(\beta)J_0(\alpha)S_\omega J_1(\alpha)J_1(\beta)\left(S^*_{\omega+\Omega_1+\Omega_2}e^{-i(\Omega_1+\Omega_2)t} - S^*_{\omega+\Omega_1-\Omega_2}e^{-i(\Omega_1-\Omega_2)t}\right. \\
& \left. -S^*_{\omega-\Omega_1+\Omega_2}e^{i(\Omega_1-\Omega_2)t} + S^*_{\omega-\Omega_1-\Omega_2}e^{i(\Omega_1+\Omega_2)t}\right) \\
+ \quad & J_0(\beta)J_0(\alpha)S^*_\omega J_1(\alpha)J_1(\beta)\left(S_{\omega+\Omega_1+\Omega_2}e^{i(\Omega_1+\Omega_2)t} - S_{\omega+\Omega_1-\Omega_2}e^{i(\Omega_1-\Omega_2)t}\right. \\
& \left. -S_{\omega-\Omega_1+\Omega_2}e^{-i(\Omega_1-\Omega_2)t} + S_{\omega-\Omega_1-\Omega_2}e^{-i(\Omega_1+\Omega_2)t}\right) \\
+ \quad & J_1(\beta)J_0(\alpha)\left(S_{\omega+\Omega_1}e^{i\Omega_1 t} - S_{\omega-\Omega_1}e^{-i\Omega_1 t}\right)J_0(\beta)J_1(\alpha)\left(S^*_{\omega+\Omega_2}e^{-i\Omega_2 t} - S^*_{\omega-\Omega_2}e^{i\Omega_2 t}\right) \\
+ \quad & J_0(\beta)J_1(\alpha)\left(S_{\omega+\Omega_2}e^{i\Omega_2 t} - S_{\omega-\Omega_2}e^{-i\Omega_2 t}\right)J_1(\beta)J_0(\alpha)\left(S^*_{\omega+\Omega_1}e^{-i\Omega_1 t} - S^*_{\omega-\Omega_1}e^{i\Omega_1 t}\right).
\end{aligned}
\tag{B.7}
$$

Since the phase of te lockin measurement of Ω_1 is already determined such that $\cos\Omega_1 t$ is maximized we can multiply the above expression with $e^{+i\Omega_1 t}$ the result is (neglecting all $2\Omega_1$ components)

$$
\begin{aligned}
P_{\Omega_1} \quad \approx \quad & J_0(\beta)J_0(\alpha)S_\omega J_1(\alpha)J_1(\beta)\left(S^*_{\omega+\Omega_1+\Omega_2}e^{-i\Omega_2 t} - S^*_{\omega+\Omega_1-\Omega_2}e^{i\Omega_2 t}\right) \\
+ \quad & J_0(\beta)J_0(\alpha)S^*_\omega J_1(\alpha)J_1(\beta)\left(-S_{\omega-\Omega_1+\Omega_2}e^{i\Omega_2 t} + S_{\omega-\Omega_1-\Omega_2}e^{-i\Omega_2 t}\right) \\
+ \quad & J_1(\beta)J_0(\alpha)\left(-S_{\omega-\Omega_1}\right)J_0(\beta)J_1(\alpha)\left(S^*_{\omega+\Omega_2}e^{-i\Omega_2 t} - S^*_{\omega-\Omega_2}e^{i\Omega_2 t}\right) \\
+ \quad & J_0(\beta)J_1(\alpha)\left(S_{\omega+\Omega_2}e^{i\Omega_2 t} - S_{\omega-\Omega_2}e^{-i\Omega_2 t}\right)J_1(\beta)J_0(\alpha)\left(S^*_{\omega+\Omega_1}\right).
\end{aligned}
\tag{B.8}
$$

Setting $\chi = J_0(\alpha)J_0(\beta)J_1(\alpha)J_1(\beta)$ and approximating all transmission functions containing $\pm\Omega_1$ with 1:

$$
\begin{aligned}
\frac{P_{\Omega_1}}{\chi} \quad \approx \quad & -2iS_\omega \sin\Omega_2 t - 2iS^*_\omega \sin\Omega_2 t \\
& - S^*_{\omega+\Omega_2}e^{-i\Omega_2 t} + S^*_{\omega-\Omega_2}e^{i\Omega_2 t} + S_{\omega+\Omega_2}e^{i\Omega_2 t} - S_{\omega-\Omega_2}e^{-i\Omega_2 t},
\end{aligned}
\tag{B.9}
$$

$$
\frac{P_{\Omega_1}}{\chi} \quad \approx \quad -4iS_{min}\sin\Omega_2 t - (S_{\omega-\Omega_2} + S^*_{\omega+\Omega_2})e^{-i\Omega_2 t} + (S^*_{\omega-\Omega_2} + S_{\omega+\Omega_2})e^{i\Omega_2 t},
\tag{B.10}
$$

$$
S^*_{\omega-\Omega_2} + S_{\omega+\Omega_2} \quad = \quad \frac{S_{min} - 2iQ\frac{\omega_0-\omega+\Omega_2}{\omega_0}}{1 - 2iQ\frac{\omega_0-\omega+\Omega_2}{\omega_0}} + \frac{S_{min} + 2iQ\frac{\omega_0-\omega-\Omega_2}{\omega_0}}{1 + 2iQ\frac{\omega_0-\omega-\Omega_2}{\omega_0}}.
\tag{B.11}
$$

Assuming that the PDH loop locks to the resonance frequency properly we can take the limit $\omega \to \omega_0$:

$$S^*_{\omega-\Omega_2} + S_{\omega+\Omega_2} = 2\frac{S_{min} - 2iQ\frac{\Omega_2}{\omega_0}}{1 - 2iQ\frac{\Omega_2}{\omega_0}} = 2 - 2\frac{1 + S_{min}}{1 + 4Q^2\frac{\Omega_2^2}{\omega_0^2}} + 4iQ\frac{\Omega_2}{\omega_0}\frac{1 - S_{min}}{1 + 4Q^2\frac{\Omega_2^2}{\omega_0^2}}. \quad \text{(B.12)}$$

further simplification is possible if we recall that $Q = \omega_0/\Delta\omega$. Also note that $S_{\omega-\Omega_2} + S^*_{\omega+\Omega_2} = (S^*_{\omega-\Omega_2} + S_{\omega+\Omega_2})^*$. In the limit $\Omega_2 \ll \Delta\omega$ it follows that

$$
\begin{aligned}
\frac{P_{\Omega_1}}{\chi} &\approx -4iS_{min}\sin\Omega_2 t \\
&- (2S_{min} - 4iQ\frac{\Omega_2}{\omega_0}(1 - S_{min}))e^{-i\Omega_2 t} + (2S_{min} - 4iQ\frac{\Omega_2}{\omega_0}(1 - S_{min}))e^{i\Omega_2 t} \\
&= -4iS_{min}\sin\Omega_2 t + 4iS_{min}\sin\Omega_2 t + 8Q\frac{\Omega_2}{\omega_0}(1 - S_{min})\sin\Omega_2 t \\
&= 8Q\frac{\Omega_2}{\omega_0}(1 - S_{min})\sin\Omega_2 t. \quad \text{(B.13)}
\end{aligned}
$$

After a lockin measurement we thus end up with

$$P_{\Omega_1} \approx G_{tot}J_0(\alpha)J_0(\beta)J_1(\alpha)J_1(\beta)Q\frac{\Omega_2}{\omega_0}(1 - S_{min}). \quad \text{(B.14)}$$

C

DERIVATION OF AN INDUCTIVELY COUPLED RESONANCE

Here we consider what happens when we couple the resonator inductively to a transmission line. The resonator itself could still be treated as a transmission line as in the derivation in Chapter 2, however, to provide an alternate method we now instead start from a series LRC circuit and derive the same equations. Starting from the circuit in Fig. 2.2a, the first step is to calculate the impedance of the unloaded resonator. The impedance of a series RLC-circuit is

$$Z_r = \left(R + \frac{1}{j\omega C} + j\omega L \right). \tag{C.1}$$

Around the resonance frequency we can write $\omega = \omega_0 + \Delta\omega$ where ω_0 is the unloaded resonance frequency, and the impedance can be expressed as

$$Z_r = \left(R + \frac{1}{jC} \frac{1/\omega_0}{(1 + \Delta\omega/\omega_0)} + j(\omega_0 + \Delta\omega)L \right). \tag{C.2}$$

Close to the resonance frequency, $\Delta\omega/\omega_0$, is small, and we can use the approximation $1/(1+x) = 1 - x + O(x^2)$

$$Z_r \approx \left(R + \frac{1 - \Delta\omega/\omega_0}{jC\omega_0} + j(\omega_0 + \Delta\omega)L \right). \tag{C.3}$$

Since $\omega_0^2 = 1/LC$ and we know that the complex part of the impedance vanishes at resonance, we can simplify further

$$Z_r \approx \left(R + j\frac{\Delta\omega}{C\omega_0^2} + j\Delta\omega L \right) = (R + 2j\Delta\omega L) = \frac{\sqrt{L/C}}{Q_i} \left(1 + 2jQ_i\Delta\omega/\omega_0 \right), \tag{C.4}$$

where we also have used $Q_i = \sqrt{L/C}/R$. Now we can consider the complete circuit, and we will derive an expression for the parallel loaded transmission-line. For this we introduce two new variables, M which is the mutual inductance between the transmission line and the coupling segment of the resonator, and L_1, the inductance of the transmission-line over the distributed load of the resonator. The input impedance of the circuit in Fig. 2.2a is [26]

$$Z_{in} = j\omega L_1 + \frac{\omega^2 M^2}{Z_r}. \tag{C.5}$$

Here we introduce another complex term which means that the resonance frequency of the loaded circuit will be shifted. We can calculate the shift by solving $Im(Z_{in}) = 0$ for $\Delta\omega$.

$$\frac{\Delta\omega}{\omega_0} \approx -\frac{M^2}{4LL_1} + \sqrt{\frac{M^4}{16L^2L_1^2} + \frac{1}{4Q_i^2}}. \tag{C.6}$$

This frequency shift is very small. Only if the internal Q of the resonator is low and the coupling is weak (M small) it can have a noticeable effect on the resonance frequency, however in such undercoupled situations the resonance will be hardly detectable. In the following analysis we therefore assume that the frequency shift is zero, neglecting the first term in eq. (C.5) near $\omega = \omega_0$.

$$Z_{in} \approx \frac{\omega_0^2 M^2}{Z_r} = \frac{\omega_0 M^2 Q_i}{L} \frac{1}{1 + 2jQ_i\Delta\omega/\omega_0}. \tag{C.7}$$

To calculate the transmission it is important to consider the topology. This case is different from the capacitively coupled resonator, here the impedance we have calculated is in series with the transmission line. The S-parameter for such a topology is

$$S_{21} = \frac{2Z_0}{2Z_0 + Z_{in}^*}, \tag{C.8}$$

and in our case we can derive the following expression

$$S_{21} = \frac{S_{21,\mathrm{min}} + 2jQ_t\frac{\Delta\omega}{\omega_0}}{1 + 2jQ_t\frac{\Delta\omega}{\omega_0}}. \tag{C.9}$$

The transmitted signal for a inductively loaded quarter-wave resonator is identical to that of a capacitively loaded resonator (see eq. (2.12)). This means we can treat this kind of resonators using exactly the same framework that has been developed for capacitively coupled resonators. It is possible to deduce the respective quality factors from

$$S_{21,\mathrm{min}} = \frac{1}{1 + \frac{\omega_0 M^2 Q_i}{2Z_0 L}} \qquad Q_t = \frac{Q_i}{1 + \frac{\omega_0 M^2 Q_i}{2Z_0 L}}, \tag{C.10}$$

resulting in the coupling quality factor

$$Q_c = \frac{2Z_0 L}{\omega_0 M^2} = \frac{2Z_0 Z_r}{\omega_0^2 M^2} = \frac{2L_1 L}{M^2}. \tag{C.11}$$

D
MASTER EQUATION FOR NSMM-TLF INTERACTION

Here we look at the details behind the calculation in Fig. 5.8.

Geometrically dependent coupling

The coupling g to a TLF in the Hamiltonian (5.18) depends on the placement and electric field of the tip. We rewrite eq. (5.31) into its most general form

$$g(r) = \frac{e}{\hbar\pi}\vec{E}(\vec{r}, h) \cdot \vec{d},$$ (D.1)

where

$$\vec{E}(\vec{r}, h) = \frac{2r_{\text{tip}}V_0(\varepsilon_r - 1)}{(\varepsilon_r + 1)^2}\sum_{n=1}^{\infty} t_n \frac{r\hat{e}_r + (h_\varepsilon + a_n r_{\text{tip}})\hat{e}_z}{[r^2 + (h_\varepsilon + a_n r_{\text{tip}})^2]^{3/2}},$$ (D.2)

with recursive coeficcients $a_1 = (r_{\text{tip}} + h_0)/r_{\text{tip}}$, $a_n = a_1 - 1/(a_1 + a_{n-1})$, $t_1 = 1$, and $t_n = t_{n-1}/(a_1 + a_{n-1})$ [139]. The voltage on the tip is given by the voltage due to a single photon, $V_0 = \sqrt{\hbar\omega_0/2C}$. In our calculations we assume that the TLF dipole is pointing in the z-direction. In a similar way we also have the tip-sample capacitance

$$C = 4\pi\varepsilon_0 r_{\text{tip}}\sum_{n=1}^{\infty} t_n.$$ (D.3)

Master equation for TLF - tip interaction

We model the evolution of the response of the NSMM probe in a dissipative environment using the master equation

$$\frac{\partial\rho}{\partial t} = -\frac{i}{\hbar}[\rho, H] + \mathcal{L}(\rho),$$ (D.4)

with the Lindblad operator on the form

$$\mathcal{L}(\rho) = \sum_k C_k\rho C_k^\dagger - \frac{1}{2}(C_k^\dagger C_k\rho + \rho C_k^\dagger C_k),$$ (D.5)

with the coupling operators $C_k = [\sqrt{\gamma}\sigma^-, \sqrt{\omega_0/Q}a, \sqrt{\gamma_\phi/2}\sigma_z]$ that accounts for intrinsic TLS energy relaxation, cavity loss rate, and environmental dephasing of the TLS respectively. The frequency shift of the NSMM probe

$$\delta\omega = \omega_0(g = 0) - \omega_0(g(r)), \tag{D.6}$$

is evaluated using the Hamiltonian (5.18) with tha additional driving field $H_d = \mathcal{E}(e^{-i\omega_d t}a^\dagger + e^{i\omega_d t}a)$ (under the rotating wave approximation) and a coupling that depends on the electric field $g = g(|E_z|) = g(r)$. From the ω that maximizes the spectral output

$$P(\omega) = \frac{1}{2\pi}\int_{-\infty}^{\infty} e^{-i\omega t}\text{Tr}\{a^\dagger e^{\mathcal{L}t}a\rho\}dt, \tag{D.7}$$

we find $\omega_0(g(r))$. We nummerically evaluate the spectral output using the Quantum optics toolbox [172].

BIBLIOGRAPHY

[1] R. P. Feynman. Simulating physics with computers. *Int. J. Theor. Phys.*, 21:467, 1982.

[2] P. Kok, W. J. Munro, K. Nemoto, T. C. Ralph, J. P. Dowling, and G. J. Milburn. Linear optical quantum computing with photonic qubits. *Rev. Mod. Phys.*, 79:135, 2007.

[3] F. A. Zwanenburg, A. S. Dzurak, A. Morello, M. Y. Simmons, L. C. L. Hollenberg, G. Klimeck, S. Rogge, S. N. Coppersmith, and M. A. Eriksson. Silicon quantum electronics. *Rev. Mod. Phys.*, 85:961, 2013.

[4] M. H. Devoret and R. J. Schoelkopf. Suerconducting circuits for quantum information: An outlook. *Science*, 339:1169, 2013.

[5] A. G. Fowler, M. Mariantoni, J. M. Martinis, and A. N. Cleland. Surface codes: Towards practical large-scale quantum computation. *Phys. Rev. A*, 86:032324, 2012.

[6] J. N. Eckstein and J. Levy. Materials issues for quantum computation. *MRS Bulletin*, 38:783, 2013.

[7] J. A. Schreier, A. A. Houck, J. Koch, D. I. Schuster, B. R. Johnson, J. M. Chow, J. M. Gambetta, J. Majer, L. Frunzio, M. H. Devoret, S. M. Girvin, and R. J. Schoelkopf. Suppressing charge noise decoherence in superconducting charge qubits. *Phys. Rev. B*, 77:180502, 2008.

[8] H. Paik, D. I. Schuster, L. S. Bishop, G. Kirchmair, G. Catelani, A. P. Sears, B. R. Johnson, M. J. Reagor, L. Frunzio, L. I. Glazman, S. M. Girvin, M. H. Devoret, and R. J. Schoelkopf. Observation of high coherence in josephson junction qubits measured in a three-dimensional circuit qed architecture. *Phys. Rev. Lett.*, 107:240501, 2011.

[9] L. Faoro and L. B. Ioffe. Internal loss of superconducting resonators induced by interacting two-level systems. *Phys. Rev. Lett.*, 109:157005, 2012.

[10] D. A. Bonnell, D. N. Basov, M. Bode, U. Diebold, S. V. Kalinin, V. Madhavan, L. Novotny, M. Salmeron, U. D. Schwarz, and P. S. Weiss. Imaging physical phenomena with local probes: From electrons to photons. *Rev. Mod. Phys.*, 84:1343, 2012.

[11] G. Binning, C. F. Quate, and C. Gerber. Atomic force microscope. *Phys. Rev. Lett.*, 56:930, 1986.

[12] M. J. Yoo, T. A. Fulton, H. F. Hess, R. L. Willett, L. N. Dunkleberger, R. J. Chichester, L. N. Pfeiffer, and K. W. West. Scanning single-electron transistor microscopy: Imaging individual charges. *Science*, 276:579, 1997.

[13] F. Mohn, L. Gross, N. Moll, and G. Meyer. Imaging the charge distribution within a single molecule. *Nature Nanotech.*, 7:227, 2012.

[14] C. Schönenberger and S. F. Alvarado. Observation of single charge carriers by force microscopy. *Phys. Rev. Lett.*, 65:3162, 1990.

[15] J. Gao. *The physics of superconducting microwave resonators*. PhD thesis, California Insitute of Technology, 2008.

[16] B. A. Mazin. *Microwave kinetic inductance detectors.* PhD thesis, California Insitute of Technology, 2004.

[17] E. A. Tholén, A. Ergül, E. M. Doherty, F. M. Weber, F. Grégis, and D. B. Haviland. Nonlinearities and parametric amplification in superconducting coplanar waveguide resonators. *Appl. Phys. Lett.*, 90:253509, 2007.

[18] K. Saeedi, S. Simmons, J. Z. Salvail, P. Dluhy, H. Riemann, N. V. Abrosimov, P. Becker, H.-J. Pohl, J. J. L. Morton, and M. L. W. Thewalt. Room-temperature quantum bit storage exceeding 39 minutes using ionized donors in silicon-28. *Science*, 342:830, 2013.

[19] F. Troiani and M. Affronte. Molecular spins for quantum information technologies. *Chem. Soc. Rev.*, 40:3119, 2011.

[20] M. S. Khalil, F. C.Wellstood, and K. D. Osborn. Loss dependence on geometry and applied power in superconducting coplanar resonators. *IEEE Trans. Appl. Supercond.*, 21:879, 2011.

[21] A. A. Houck, J. A. Schreier, B. R. Johnson, J. M. Chow, J. Koch, J. M. Gambetta, D. I. Schuster, L. Frunzio, M. H. Devoret, S. M. Girvin, , and R. J. Schoelkopf. Controlling the spontaneous emission of a superconducting transmon qubit. *Phys. Rev. Lett.*, 101:080502, 2008.

[22] Z. Kim, B. Suri, V. Zaretskey, S. Novikov, K. D. Osborn, A. Mizel, F. C. Wellstood, and B. S. Palmer. Decoupling a cooper-pair box to enhance the lifetime to 0.2 ms. *Phys. Rev. Lett.*, 106:120501, 2011.

[23] Z. K. Minev, I. M. Pop, and M. H. Devoret. Planar superconducting whispering gallery mode resonators. *Appl. Phys. Lett.*, 103:142604, 2013.

[24] D. M. Pozar. *Microwave Engineering.* John Wiley & Sons, second edition, 1998.

[25] R. Barends. *Photon-detecting superconducting resonators.* PhD thesis, Technische Universiteit Delft, 2009.

[26] D. Kajfez and P. Guillon. *Dielectric resonators.* SciTec, second edition, 1998.

[27] Y. Komatsu and Y. Murakami. Coupling coefficient between microstrip line and dielectric resonator. *IEEE Trans. Microwave Theory and Techniques*, 31:34, 1983.

[28] R. E. Collin. *Foundations for Microwave Engineering.* Wiley, second edition, 2001.

[29] J. Schlaerth, A. Vayonakis, P. Day, J. Glenn, J. Gao, S. Golwala, S. Kumar, H. LeDuc, B. Mazin, and J. Vaillancourt anf J. Zmuidzinas. A millimeter and submillimeter kinetic inductance detector camera. *J. Low Temp. Phys.*, 151:684, 2008.

[30] M. S. Khalil, M. J. A. Stoutimore, F. C.Wellstood, and K. D. Osborn. An analysis method for asymmetric resonator transmission applied to superconducting devices. *J. Appl. Phys.*, 111:054510, 2012.

[31] A. Megrant, C. Neill, R. Barends, B. Chiaro, Y. Chen, L. Feigl, J. Kelly, E. Lucero, M. Mariantoni, P. J. J. OÕMalley, D. Sank, A. Vainsencher, J. Wenner, T. C. White, Y. Yin, J. Zhao, C. J. Palmstrøm, J. M. Martinis, , and A. N. Cleland. Planar superconducting resonators with internal quality factors above one million. *Appl. Phys. Lett.*, 100:113510, 2012.

[32] J. C. Weber, J. B. Schlager, N. Sanford, A. Imtiaz, T. M. Wallis, L. M. Mansfield, K. J. Coakley, K. Bertness, P. Kabos, and V. M. Bright. A near-field scanning microwave microscope for characterization of inhomogeneous photovoltaics. *Rev. Sci. Instrum.*, 83:083702, 2012.

[33] B. T. Rosner and D. W. van der Weide. High-frequency near-field microscopy. *Rev. Sci. Instrum.*, 73:2505, 2002.

[34] J. Wenner, R. Barends, R. C. Bialczak, Y. Chen, J. Kelly, E. Lucero, P. J. J. O'Malley M. Mariantoni, A. Megrant, D. Sank, A. Vainsencher, H. Wang, T. C. White, Y. Yin, J. Zhao, A. N. Cleland, and J. M. Martinis. Surface loss simulations of superconducting coplanar waveguide resonators. *Appl. Phys. Lett.*, 99:113513, 2011.

[35] C. Neill, A. Megrant, R. Barends, Y. Chen, B. Chiaro, J. Kelly, J. Y. Mutus, P. J. J. O'Malley, D. Sank, J. Wenner, T. C. White, Y. Yin, A. N. Cleland, and J. M. Martinis. Fluctuations from edge defects in superconducting resonators. *Appl. Phys. Lett.*, 103:072601, 2013.

[36] J. Burnett, T. Lindström, M. Oxborrow, Y. Harada, Y. Sekine, P. Meeson, and A. Ya. Tzalenchuk. Slow noise processes in superconducting resonators. *Phys. Rev. B*, 87:140501(R), 2013.

[37] J. Burnett. *High precision readout of superconducting resonators for analysis of slow noise processes.* PhD thesis, Royal Holloway, University of London, 2013.

[38] H. Wang, M. Hofheinz, J. Wenner, M. Ansmann, R. C. Bialczak, M. Lenander, E. Lucero, M. Neeley, A. D. O'Connell, D. Sank, M. Weides, A. N. Cleland, and J. M. Martinis. Improving the coherence time of superconducting coplanar resonators. *Appl. Phys. Lett.*, 95:233508, 2009.

[39] P. Masha, S. H. W. van der Ploeg, G. Oelsner, E. Il'ichev, S. Wünsch H. G. Meyer, and M. Siegel. Losses in coplanar waveguide resonators at millikelvin temperatures. *Appl. Phys. Lett.*, 96:062503, 2010.

[40] D. I. Schuster. *Circuit Quantum Electrodynamics.* PhD thesis, Yale University, 2007.

[41] K. Yoshida, K. Watanabe, T. Kisu, and K. Enpuku. Evaluation of magnetic penetration depth and surface resistance of superconducting thin films using coplanar waveguides. *IEEE Trans. Appl. Supercond.*, 5:1979, 1995.

[42] M. Tinkham. *Introduction to Superconductivity.* McGraw-Hill, second edition, 1996.

[43] S. K. Yip and J. A. Sauls. Nonlinear meissner effect in cuo superconductors. *Phys. Rev. Lett*, 69:2264, 1992.

[44] D. C. Mattis and J. Bardeen. Theory of the anomalous skin effect in normal and superconducting metals. *Phys. Rev.*, 111:412, 1958.

[45] W. T. Norris. Calculation of hysteresis losses in hard superconductors carrying ac: isolated conductors and edges of thin sheets. *J. Phys. D: Appl. Phys.*, 3:489, 1970.

[46] E. H. Brandt and M. Indenbom. Type-ii-superconductor strip with current in a perpendicular magnetic field. *Phys. Rev. B*, 48:12893, 1993.

[47] P. Lahl and R. Wördenweber. Probing microwave properties of high-tc films via small dc magnetic fields. *Appl. Phys. Lett.*, 81:505, 2002.

[48] A. A. B. Brojeny, Y. Mawatari, M. Benkraouda, and J. R. Clem. Magnetic fields and currents for two current-carrying parallel coplanar superconducting strips in a perpendicular magnetic field. *Supercond. Sci. Technol.*, 15:1454, 2002.

[49] C. P. Bean. Magnetization of high-field superconductors. *Rev. Mod. Phys.*, 36:31, 1964.

[50] J. E. Healey, T. Lindström, M. S. Colclough, C. M. Muirhead, and A. Ya. Tzalenchuk. Magnetic field tuning of coplanar waveguide resonators. *Appl. Phys. Lett.*, 93:043513, 2008.

[51] D. Bothner, T. Gaber, M. Kemmler, D. Koelle, and R. Kleiner. Improving the performance of superconducting microwave resonators in magnetic fields. *Appl. Phys. Lett.*, 98:102504, 2011.

[52] D. Bothner, C. Clauss, E. Koroknay, M. Kemmler, T. Gaber, M. Jetter, M. Scheffler, P. Michler, M. Dressel, D. Koelle, and R. Kleiner. Reducing vortex losses in superconducting microwave resonators with microsphere patterned antidot arrays. *Appl. Phys. Lett.*, 100:012601, 2012.

[53] D. Bothner, T. Gaber, M. Kemmler, D. Koelle, and R. Kleiner. Magnetic hysteresis effects in superconducting coplanar microwave resonators. *Phys. Rev. B*, 86:014517, 2012.

[54] C. Song, M. P. DeFeo, K. Yu, and B. L. T. Plourde. Reducing microwave loss in superconducting resonators due to trapped vortices. *Appl. Phys. Lett*, 95:232501, 2009.

[55] G. Benz, T. A. Scherer, M. Neuhaus, and W. Jutzi. Quality factor and intermodulation product of superconducting coplanar wave guides with slots in a dc magnetic field. *IEEE Trans. Appl. Supercond.*, 9:3046, 1999.

[56] D. Yu. Vodolazov and I. L. Maksimov. Distribution of the magnetic field and current density in superconducting films of finite thickness. *Physica C*, 349:125, 2001.

[57] C. P. Bean and J. P. Livingston. Surface barrier in type-ii superconductors. *Phys. Rev. Lett.*, 12:14, 1964.

[58] G. Stejic, A. Gurevich, E. Kadyrov, D. Christen, R. Joynt, and D. C. Larbalestier. Effect of geometry on the critical currents of thin films. *Phys. Rev. B*, 49:1274, 1994.

[59] L. Yu, R. K. Singh, H. Liu, S. Y. Wu, R. Hu, D. Durand, J. Bulman, J. M. Rowell, and N. Newman. Fabrication of niobium titanium nitride thin films with high superconducting transition temperatures and short penetration lengths. *IEEE Trans. Appl. Supercond.*, 15:44, 2005.

[60] C. Kittel. *Introduction to solid state physics*. Wiley, eighth edition, 2005.

[61] M. Mondal, M. Chand, A. Kamlapure, J. Jesudasan, V. C. Bagwe, S. Kumar, G. Saraswat, V. Tripathi, and P. Raychaudhuri. Phase diagram and upper critical field of homogeneously disordered epitaxial 3-dimensional NbN films. *J. Supercond. Nov. Magn.*, 24:341, 2011.

[62] M. P. Mathur, D. W. Deis, and J. R. Gavaler. Lower critical field measurements in NbN bulk and thin films. *J. Appl. Phys.*, 43:3158, 1972.

[63] C. Song, T. W. Heitmann, M. P. DeFeo, K. Yu, R. McDemott, M. Neeley, J. M. Martinis, and B. L. T. Plourde. Microwave response of vortices in superconducting thin films of Re and Al. *Phys. Rev. B*, 79:174512, 2009.

[64] J. A. Weil and J. R. Bolton. *Electron Paramagnetic Resonance: Elementary theory and practical applications*. Wiley, second edition, 2007.

[65] J. Lehmann, A. Gaita-Ariño, E. Coronado, and D. Loss. Quantum computing with molecular spin systems. *J. Mater. Chem.*, 19:1672, 2009.

[66] M. Trif, F. Troiani, D. Stepanenko, and D. Loss. Spin-electric coupling in molecular magnets. *Phys. Rev. Lett.*, 101:217201, 2008.

[67] R. E. George, J. P. Edwards, and A. Ardavan. Coherent spin control by electrical manipulation of the magnetic anisotropy. *Phys. Rev. Lett.*, 110:027601, 2013.

[68] S. Nadj-Perge, V. S. Pribiag, J. W. G. van den Berg, K. Zuo, S. R. Plissard, E. P. A. M. Bakkers, S. M. Frolov, and L. P. Kouwenhoven. Spectroscopy of spin-orbit quantum bits in indium antimonide nanowires. *Phys. Rev. Lett.*, 108:166801, 2012.

[69] C. Bosch-Serrano, J. M. Clemente-Juan, E. Coronado, A. Gaita-Ariño andA. Palii, and B. Tsukerblat. Electric field control of the spin state in mixed-valence magnetic molecules. *ChemPhysChem*, 13:2662, 2012.

[70] F. Chen, A. J. Sirois, R. W. Simmonds, and A. J. Rimberg. Introduction of a dc bias into a high-q superconducting microwave cavity. *Appl. Phys. Lett.*, 98:132509, 2011.

[71] K. D. Petersson, L. W. McFaul, M. D. Schroer, M. Jung, J. M. Taylor, A. A. Houck, and J. R. Petta. Circuit quantum electrodynamics with a spin qubit. *Nature*, 490:380, 2012.

[72] S-X. Li and J. B. Kycia. Applying a direct current bias to superconducting microwave resonators by using superconducting quarter wavelength band stop filters. *Appl. Phys. Lett.*, 102:242601, 2013.

[73] R. V. Pound. Electronic frequency stabilization of microwave oscillators. *Rev. Sci. Instrum.*, 17:490, 1946.

[74] E. D. Black. An introduction to pound-drever-hall laser frequency stabilization. *Am. J. Phys.*, 69:79, 2001.

[75] T. Lindström, J. Burnett, M. Oxborrow, and A. Ya. Tzalenchuk. Pound-locking for characterization of superconducting microresonators. *Rev. Sci. Instrum.*, 82:104706, 2011.

[76] E. A. Synge. A suggested method for extending microscopic resolution into the ultra-microscopic region. *Phil. Mag.*, 6:356, 1928.

[77] Z. Frait, V. Kambersky, Z. Malek, and M. Ondris. Local variations of uniaxial anisotropy in thin films. *Czeck. J. Phys. B*, 10:616, 1960.

[78] G. Binning and H. Rohrer. Scanning tunneling microscopy. *Helvetica Physica Acta*, 55:726, 1982.

[79] S. M. Anlage, V. V. Talanov, and A. R. Schwartz. Principles of near-field microwave microscopy. In S. V. Kalinin and A. Gruverman, editors, *Scanning Probe Microscopy: Electrical and Electromechanical Phenomena at the Nanoscale, Volume 1*, pages 215–253. Springer-Verlag, New York, 2007.

[80] J. Lee, C. J. Long, H. Yang, X.-D. Xiang, and I. Takeuchi. Atomic resolution imaging at 2.5 ghz using near-field microwave microscopy. *Appl. Phys. Lett.*, 97:183111, 2010.

[81] A. Imtiaz, S. M. Anlage, J. D. Barry, and J. Melngailis. Nanometer-scale material contrast imaging with a near-field microwave microscope. *Appl. Phys. Lett.*, 90:143106, 2007.

[82] N. Chinone, K. Yamasue, Y. Hiranaga, K. Honda, and Y. Cho. Lateral resolution improvement in scanning nonlinear dielectric microscopy by measuring super-higher-order nonlinear dielectric constants. *Appl. Phys. Lett.*, 101:213112, 2012.

[83] K. Lai, M. B. Ji, N. Leindecker, M. A. Kelly, and Z. X. Shen. Atomic-force-microscope-compatible near-field scanning microwave microscope with separated excitation and sensing probes. *Rev. Sci. Instrum.*, 78:063702, 2007.

[84] H. P. Huber, M. Moertelmaier, T. M. Wallis, C. J. Chiang, M. Hochleitner, A. Imtiaz, Y. J. Oh, K. Schilcher, M. Dieudonne, J. Smoliner, P. Hinterdorfer, S. J. Rosner, H. Tanbakuchi, P. Kabos, and F. Kienberger. Calibrated nanoscale capacitance measurements using a scanning microwave microscope. *Rev. Sci. Instrum.*, 81:113701, 2010.

[85] K. Lee, H. Melikyan, A. Babajanyan, T. Sargsyan, J. Kim, S. Kim, and B. Friedman. Investigation of photoconductivity of silicon solar cells by a near-field scanning microwave microscope. *Ultramicroscopy*, 109:889, 2009.

[86] W. Kundhikanjana, K. Lai, M. A. Kelly, and Z-X. Shen. Cryogenic microwave imaging of metal-insulator transition in doped silicon. *Rev. Sci. Instrum.*, 82:033705, 2011.

[87] H. P. Huber, I. Humer, M. Hochleitner, M. Fenner, M. Moertelmaier, C. Rankl, A. Imtiaz, T. M. Wallis, H. Tanbakuchi, P. Hinterdorfer, P. Kabos, J. Smoliner, J. J. Kopanski, and F. Kienberger. Calibrated nanoscale dopant profiling using a scanning microwave microscope. *J. Appl. Phys.*, 111:014301, 2012.

[88] V. V. Talanov, C. Del Barga, L. Wickey, I. Kalichava, E. Gonzales, E. Shaner, A. V. Gin, and N. G. Kalugin. Few-layer graphene characterization by near-field scanning microwave microscopy. *ACS Nano*, 4:3831, 2010.

[89] A. F. Lann, M. Abu-Teir, M. Golosovsky, D. Davidov, A. Goldgirsch, and V. Beilin. Magnetic-field-modulated microwave reflectivity of high-t_c superconductors studied by near-field mm-wave microscopy. *Appl. Phys. Lett.*, 75:1766, 1999.

[90] S. Okazaki, N. Okazaki, X. Zhao, H. Sugaya, S. Yaginuma, R. Takahashi, M. Murakami, Y. Matsumoto, T. Chikyow, H. Koinuma, and T. Hasegawa. High-throughput characterization of local conductivity of $Nd_{0.9}Ca_{0.1}Ba_2Cu_3O_{7-\delta}$ thin film by the low-temperature scanning microwave microscope. *Applied Surface Science*, 252:2615, 2005.

[91] R. Lu, C. Christianson, J. Dizon, J. Wu, T. Haugan, P. Barnes, and F. Javier Baca. Investigation of dynamic behaviors of low-level dissipation at $YBa_2Cu_3O_7$ grain boundaries using low temperature near field scanning microwave microscopy. *IEEE Trans. Appl. Supercond.*, 21:3238, 2011.

[92] R. A. Kleismit, G. Kozlowski, R. Biggers, I. Maartense, M. K. Kazimierczuk, and D. B Mast. Characterization of local dielectric properties of superconductor $YBa_2Cu_3O_{7-\delta}$ using evanescent microwave microscopy. *IEEE Trans. Appl. Supercond.*, 15:2915, 2005.

[93] K. Lai, M. Nakamura, W. Kundhikanjana, M. Kawasaki, Y. Tokura, M. Kelly, and Z-X. Shen. Mesoscopic percolating resistance network in a strained manganite thin film. *Science*, 329:190, 2010.

[94] H. Melikyan, T. Sargsyan, A. Babajanyan, S. Kim, J. Kim, K. Lee, and B. Friedman. Hard disk magnetic domain nano-spatial resolution imaging by using a near-field scanning microwave microscope with an afm probe tip. *J. of Magnetism and Magnetic Materials*, 321:2483, 2009.

[95] M. Abu-Teir, F. Sakran, M. Golosovsky, D. Davidov, and A. Frenkel. Local contactless measurement of the ordinary and extraordinary hall effect using near-field microwave microscopy. *Appl. Phys. Lett.*, 80:1776, 2002.

[96] A. Babajanyan, H. Melikyan, J. Carnis, Y. Yoon, H. Lee, H. K. Yoo, K. Lee, and B. Friedman. Characterization of the field-effect conductivity distribution in pentacene thin-film transistors by a near-field scanning microwave microscope. *Synthetic metals*, 161:931, 2011.

[97] T. Lim, E.and Manaka, M. Iwamoto, B. Friedman, A. Babajanyan, S. Kim, Y. Yoon, S. Kim, and K. Lee. Investigation of space charge at pentacene/au interface with uv/ozone treatment by a near-field microwave microprobe. *Thin Solid Films*, 516:2573, 2008.

[98] M. Park, H. Yoo, H. Yoo, S. Na, S. Kim, K. Lee, B. Friedman, E. Lim, and M. Iwamoto. Phase transition of copper (ii) phthalocyanine thin films characterized by a near-field scanning microwave microscope. *Thin Solid Films*, 499:318, 2006.

[99] S. Kim, Y. Jang, S. Kim, T.-D. Kim, H. Melikyan, A. Babajanyan, K. Lee, and B. Friedman. Detection of dna-hybridization using a near-field scanning microwave microscope. *J. of Nanoscience and Nanotechnology*, 11:4222, 2011.

[100] L. Fumagalli, G. Ferrari, M. Sampietro, and G. Gomila. Quantitative nanoscale dielectric microscopy of single-layer supported biomembranes. *Nano Letters*, 9:1604, 2009.

[101] F. X. Li, M. Tabib-Azar, and J. A. Mann. Electron spin resonance imaging with afm using near field microwave techniques. *Proc. of the 7th IEEE Int. Conf. on Nanotechnology*, 1:422, 2007.

[102] F. X. Li, J. A. Mann, and M. Tabib-Azar. Near field microwave microscope and electron-spin-resonance detection: ruby crystal surface. *Applied Optics*, 45:2191, 2006.

[103] S. M. Anlage, B. J. Feenstra D. E. Steinhauer, C. P. Vlahacos, and F. C. Wellstood. Near-field microwave microscopy of materials properties. In H. Weinstock and M. Nisenoff, editors, *Microwave Superconductivity*, pages 239–269. Kluwer, Amsterdam, 2001.

[104] A. F. Lann, M. Abu-Teir, M. Golosovsky, D. Davidov, D. Djordjevic, N. Bontemps, and L. F. Cohen. A cryogenic microwave scanning near-field probe: Application to study of high-tc superconductors. *Rev. Sci. Instrum.*, 70:4348, 1999.

[105] K. Karrai and R. D. Grober. Piezoelectric tip-sample distance control for near field optical microscopes. *Appl. Phys. Lett.*, 66:1842, 1995.

[106] F. J. Geissibl. Atomic resolution on si(111)-(7x7) by noncontact atomic force microscopy with a force sensor based on a quartz tuning fork. *Appl. Phys. Lett.*, 76:1470, 2000.

[107] Y. Qin and R. Reifenberger. Calibrating a tuning fork for use as a scanning probe microscope force sensor. *Rev. Sci. Instrum.*, 78:063704, 2007.

[108] F. J. Geissibl, H. Bielefeldt, S. Hembacher, and J. Mannhart. Calculation of the optimal imaging parameters for frequency modulation atomic force microscopy. *Appl. Surf. Sci.*, 140:352, 1999.

[109] F. J. Giessibl and H. Bielefeldt. Physical interpretation of frequency-modulation atomic force microscopy. *Phys. Rev. B*, 61:9968, 1999.

[110] F. J. Geissibl. High-speed force sensor for force microscopy and profilometry utilizing a quartz tuning fork. *Appl. Phys. Lett.*, 73:3956, 1998.

[111] C. Plassard, E. Bourillot, J. Rossignol, Y. Lacroute, E. Lepleux, L. Pacheco, and E. Lesniewska. Detection of defects buried in metallic samples by scanning microwave microscopy. *Phys. Rev. B*, 83:121409, 2011.

[112] R. Barends, H. L. Hortensius, T. Zijlstra, J. J. A. Baselmans, S. J. C. Yates, J. R. Gao, and T. M. Klapwijk. Noise in NbTiN, Al, and Ta superconducting resonators on silicon and sapphire substrates. *IEEE Trans. Appl. Supercond.*, 19:936, 2009.

[113] F. Persson. *Fast dynamics and measurements of single-charge devices*. PhD thesis, Chalmers University of Technology, 2010.

[114] A. Shnirman, G. Schön, and Z. Hermon. Quantum manipulations of small josephson junctions. *Phys. Rev. Lett.*, 79:2371, 1997.

[115] C. M. Wilson, G. Johansson, T. Duty, F. Persson, M. Sandberg, and P. Delsing. Dressed relaxation and dephasing in a strongly driven two-level system. *Phys. Rev. B*, 81:024520, 2010.

[116] C. M. Wilson, T. Duty, F. Persson, M. Sandberg, G. Johansson, and P. Delsing. Coherence times of dressed states of a superconducting qubit under extreme driving. *Phys. Rev. Lett.*, 98:257003, 2007.

[117] M. Sillanpää, T. Lehtinen, A. Paila, Y. Makhlin, and P. Hakonen. Continuous-time monitoring of landau-zener interference in a cooper-pair box. *Phys. Rev. Lett.*, 96:087002, 2006.

[118] T. Duty, G. Johansson, K. Bladh, D. Gunnarsson, C. Wilson, and P. Delsing. Observation of quantum capacitance in the cooper-pair transistor. *Phys. Rev. Lett.*, 95:206807, 2005.

[119] L. D. Landau. On the theory of transfer of energy at collisions ii. *Phys. Z. Sowjetunion*, 2:46, 1932.

[120] C. Zener. Non-adiabatic crossing of energy levels. *Proc. R. Soc. Lond. A*, 137:696, 1932.

[121] S. N. Shevchenko, S. Ashab, and F. Nori. Landau-zener-stückelberg interferometry. *Phys. Rep.*, 492:1, 2010.

[122] W. D. Oliver and S. O. Valenzuela. Large-amplitude driving of a superconducting artificial atom. *Quantum Inf. Process.*, 8:261, 2009.

[123] M. D. LaHaye, J. Suh, P. M. Echternach, K. C. Schwab, and M. L. Roukes. Nanomechanical measurements of a superconducting qubit. *Nature*, 459:960, 2009.

[124] P. Huang, J. Zhou, F. Fang, X. Kong, X. Xu, C. Ju, and J. Du. Landau-zener-stückelberg interferometry of a single electronic spin in a noisy environment. *Phys. Rev. X*, 1:011003, 2011.

[125] J. R. Petta, H. Lu, and A. C. Gossard. A coherent beam splitter for electronic spin states. *Science*, 327:669, 2010.

[126] H. Ribeiro and G. Burkard. Nuclear state preparation via landau-zener-stückelberg transitions in double quantum dots. *Phys. Rev. Lett.*, 102:216802, 2009.

[127] A. Izmalkov, S. H. W. van der Ploeg, S. N. Shevchenko, M. Grajcar, E. Il'ichev, U. Hübner, A. N. Omelyanchouk, and H.-G. Meyer. Consistency of ground state and spectroscopic measurements on flux qubits. *Phys. Rev. Lett.*, 101:017003, 2009.

[128] A. Blais, R-S. Huang, A. Wallraff, S. M. Girvin, and R. J. Schoelkopf. Cavity quantum electrodynamics for superconducting electrical circuits: An architecture for quantum computation. *Phys. Rev. A*, 69:062320, 2004.

[129] M. Boissonneault, J. Gambetta, and A. Blais. Non-linear dispersive regime of cavity qed: The dressed dephasing model. *Phys. Rev. A*, 77:060305, 2008.

[130] C. Cohen-Tannoudji, J. Dupont-Roc, and G. Grynberg. *Atom-photon interactions*. Wiley, 1st edition, 1998.

[131] F. A. M. de Oliveira, M. S. Kim, P. L. Knight, and V. Buzek. Properties of displaced number states. *Phys. Rev. A*, 41:2645, 1990.

[132] F. Forster, G. Petersen, S. Manus, P. Hänggi, D. Schuh, W. Wegscheider, S. Kohler, and S. Ludwig. Characterization of qubit dephasing by landau-zener interferometry. *arXiv:1309.5907v2*, 2013.

[133] M.S. Rudner, A.V. Shytov, L. S. Levitov, D.M. Berns, W. D. Oliver, S. O. Valenzuela, and T. P. Orlando. Quantum phase tomography of a strongly driven qubit. *Phys. Rev. Lett.*, 101:190502, 2008.

[134] K. B. Cooper, M. Steffen, R. McDermott, R.W. Simmonds, S. Oh, D. A. Hite, D. P. Pappas, and J. M. Martinis. Observation of quantum oscillations between a josephson phase qubit and a microscopic resonator using fast readout. *Phys. Rev. Lett.*, 93:180401, 2004.

[135] T. A. Palomaki, S. K. Dutta, R. M. Lewis, A. J. Przybysz, H. Paik, B. K. Cooper, H. Kwon, J. R. Anderson, C. J. Lobb, F. C. Wellstood, and E. Tiesinga. Multilevel spectroscopy of two-level systems coupled to a dc squid phase qubit. *Phys. Rev. B*, 81:144503, 2010.

[136] J. M. Martinis, K. B. Cooper, R. McDermott, M. Steffen, M. Ansmann, K. D. Osborn, K. Cicak, S. Oh, D. P. Pappas, R. W. Simmonds, and C. C. Yu. Decoherence in josephson qubits from dielectric loss. *Phys. Rev. Lett.*, 95:210503, 2005.

[137] M. J. A. Stoutimore, M. S. Khalil, C. J. Lobb, and K. D. Osborn. A josephson junction defect spectrometer for measuring two-level systems. *Appl. Phys. Lett.*, 101:062602, 2012.

[138] G. J. Grabovskij, T. Peichl, J. Lisenfeld, G. Weiss, and A. V. Ustinov. Strain tuning of individual atomic tunneling systems detected by a superconducting qubit. *Science*, 338:232, 2012.

[139] C. Gao and X.-D. Xiang. Quantitative microwave near-field microscopy of dielectric properties. *Rev. Sci. Instrum.*, 69:3846, 1998.

[140] Y. Kubo, C. Grezes, A. Dewes, T. Umeda, J. Isoya, H. Sumiya, N. Morishita, H. Abe, S. Onoda, T. Ohshima, V. Jacques, A. Dréau, J.-F. Roch, I. Diniz, A. Auffeves, D. Vion, D. Esteve, and P. Bertet. Hybrid quantum circuit with a superconducting qubit coupled to a spin ensemble. *Phys. Rev. Lett.*, 107:220501, 2011.

[141] M. Sandberg. *Fast-tunable resonators and quantum electrical circuits.* PhD thesis, Chalmers university of technology, 2009.

[142] J. Aumentado, M. W. Keller, J. M. Martinis, and M. H. Devoret. Nonequilibrium quasiparticles and 2e periodicity in single-cooper-pair transistors. *Phys. Rev. Lett.*, 92:066802, 2004.

[143] B. S. Palmer, C. A. Sanchez, A. Naik, M. A. Manheimer, J. F. Schneiderman, P. M. Echternach, and F. C. Wellstood. Steady-state thermodynamics of nonequilibrium quasiparticles in a cooper-pair box. *Phys. Rev. B*, 76:054501, 2007.

[144] R. M. Lutchyn, L. I. Glazman, and A. I. Larkin. Kinetics of the superconducting charge qubit in the presence of a quasiparticle. *Phys. Rev. B*, 74:064515, 2006.

[145] M. Lenander, H. Wang, R. C. Bialczak, E. Lucero, M. Mariantoni, M. Neeley, A. D. O'Connell, D. Sank, M. Weides, J. Wenner, T. Yamamoto, Y. Yin, J. Zhao, A. N. Cleland, and J. M. Martinis. Measurement of energy decay in superconducting qubits from nonequilibrium quasiparticles. *Phys. Rev. B*, 84:024501, 2011.

[146] L. Sun, L. DiCarlo, M. D. Reed, G. Catelani, L. S. Bishop, D. I. Schuster, B. R. Johnson, Ge A. Yang, L. Frunzio, L. Glazman, M. H. Devoret, and R. J. Schoelkopf. Measurements of quasiparticle tunneling dynamics in a band-gap-engineered transmon qubit. *Phys. Rev. Lett.*, 108:230509, 2012.

[147] M. D. Shaw, R. M. Lutchyn, P. Delsing, and P. M. Echternach. Kinetics of nonequilibrium quasiparticle tunneling in superconducting charge qubits. *Phys. Rev. B*, 78:024503, 2008.

[148] N. A. Court, A. J. Ferguson, R. Lutchyn, and R. G. Clark. Quantitative study of quasiparticle traps using the single-cooper-pair transistor. *Phys. Rev. B*, 77:100501, 2008.

[149] J. Leppäkangas and E. Thuneberg. Effect of decoherence on resonant cooper-pair tunneling in a voltage-biased single-cooper-pair transistor. *Phys. Rev. B*, 78:144518, 2008.

[150] J. Siewert and G. Schön. Charge transport in voltage-biased superconducting single-electron transistors. *Phys. Rev. B*, 54:7421, 1996.

[151] H. T. Brenning, S. Kafanov, T. Duty, S. E. Kubatkin, and P. Delsing. An ultrasensitive radio-frequency single-electron transistor working up to 4.2 k. *J. Appl. Phys.*, 100:114321, 2006.

[152] O. Astafiev, Yu. A. Pashkin, Y. Nakamura, T. Yamamoto, and J. S. Tsai. Quantum noise in the josephson charge qubit. *Phys. Rev. Lett.*, 93:267007, 2004.

[153] H. T. Brenning, S. E. Kubatkin, D. Erts, S. G. Kafanov, T. Bauch, and P. Delsing. A single electron transistor on an atomic force microscope probe. *Nano Lett.*, 6:937, 2006.

[154] H. Brenning. *Fabrication and Characterizatio of Aluminium single Electron Transistors for Scanning Probes.* PhD thesis, Chalmers university of technology, 2006.

[155] F. Dolde, H. Fedder, M. W. Doherty, T. Nöbauer, F. Rempp, G. Balasubramanian, T. Wolf, F. Reinhard, L. C. L. Hollenberg, F. Jelezko, and J. Wrachtrup. Electric-field sensing using single diamond spins. *Nature Physics*, 7:459, 2011.

[156] R. J. Schoelkopf, P. Wahlgren, A. A. Kozhevnikov, P. Delsing, and D. E. Prober. The radio-frequency single-electron transistor (rf-set): A fast and ultrasensitive electrometer. *Science*, 280:1238, 1998.

[157] M. U. Staudt, I.-C. Hoi, P. Krantz, M. Sandberg, M. Simoen, P. Bushev, N. Sangouard, M. Afzelius, V. S. Shumeiko, G. Johansson, P. Delsing, and C. M. Wilson. Coupling of an erbium spin ensemble to a superconducting resonator. *J. Phys. B: At. Mol. Opt. Phys.*, 45:124019, 2012.

[158] M. Afzelius, N. Sangouard, G. Johansson, M. U. Staudt, and C. M. Wilson. Proposal for a coherent quantum memory for propagating microwave photons. *New J. Phys.*, 15:065008, 2013.

[159] P. V. Klimov, A. L. Falk, B. B. Buckley, and D. D. Awschalom. Electrically driven spin resonance in silicon carbide color centers. *arXiv:1310.4844*, 2013.

[160] Y. Kubo, F. R. Ong, P. Bertet, D. Vion, V. Jacques, D. Zheng, A. Dréau, J.-F. Roch, A. Auffeves, F. Jelezko, J. Wrachtrup, M.F. Barthe, P. Bergonzo, and D. Esteve. Strong coupling of a spin ensemble to a superconducting resonator. *Phys. Rev. Lett.*, 105:140502, 2010.

[161] D. I. Schuster, A. P. Sears, E. Ginossar, L. DiCarlo, L. Frunzio, J. J. L. Morton, H. Wu, G. A. D. Briggs, B. B. Buckley, D. D. Awschalom, and R. J. Schoelkopf. High-cooperativity coupling of electron-spin ensembles to superconducting cavities d. *Phys. Rev. Lett.*, 105:140501, 2010.

[162] R. Amsüss, C. Koller, T. Nöbauer, S. Putz, S. Rotter, K. Sandner, S. Schneider, M. Schramböck, G. Steinhauser, H. Ritsch, J. Schmiedmayer, and J. Majer. Cavity qed with magnetically coupled collective spin states. *Phys. Rev. Lett.*, 107:060502, 2011.

[163] K. Sandner, H. Ritsch, R. Amsüss, Ch. Koller, T. Nöbauer, S. Putz, J. Schmiedmayer, and J. Majer. Strong magnetic coupling of an inhomogeneous nitrogen-vacancy ensemble to a cavity. *Phys. Rev. B*, 85:053806, 2012.

[164] X. Zhu, S. Saito, A. Kemp, K. Kakuyanagi, S. Karimoto, H. Nakano, W. J. Munro, Y. Tokura, M. S. Everitt, K. Nemoto, M. Kasu, N. Mizuochi, and K. Semba. Coherent coupling of a superconducting flux qubit to an electron spin ensemble in diamond. *Nature*, 478:221, 2011.

[165] D. Braun, J. Hoffman, and E. Tiesinga. Superradiance of cold atoms coupled to a superconducting circuit. *Phys. Rev. A*, 83:062305, 2011.

[166] Y. Twig, E. Dikarov, W. D. Hutchison, and A. Blank. Note: High sensitivity pulsed electron spin resonance spectroscopy with induction detection. *Rev. Sci. Instrum.*, 82:076105, 2011.

[167] H. Malissa, D. I. Schuster, A. M. Tyryshkin, A. A. Houck, and S. A. Lyon. Superconducting coplanar waveguide resonators for low temperature pulsed electron spin resonance spectroscopy. *arxiv:1202.6305*, 2012.

[168] Y. Kubo, I. Diniz, C. Grezes, T. Umeda, J. Isoya, H. Sumiya, T. Yamamoto, H. Abe, S. Onoda, T. Ohshima, V. Jacques, A. Dréau, J.-F. Roch, A. Auffeves, D. Vion, D. Esteve, and P. Bertet. Electron spin resonance detected by a superconducting qubit. *arxiv:1205.5659*, 2012.

[169] S. Cardona-Serra, J. M. Clemente-Juan, A. Gaita-Ariño, N. Suaud, O. Svobodabc, and E. Coronado. Modelling electric field control of the spin state in the mixed-valence poly-oxometalate $[\mathrm{GeV}_{14}\mathrm{O}_{40}]^{8-}$. *Chem. Commun.*, 49:9621, 2013.

[170] P. Hedegård. private communication, 2013.

[171] P. Rabl, D. DeMille, J. M. Doyle, M. D. Lukin, R. J. Schoelkopf, and P. Zoller. Hybrid quantum processors: Molecular ensembles as quantum memory for solid state circuits. *Phys. Rev. Lett.*, 97:033003, 2006.

[172] S. Tan. A computational toolbox for quantum and atomic optics. *J. Opt. B*, 1:424, 1999.